

ABSTRACT

SUBBARAMA IYER, GANESH. Effects of Different Cross Flow Schemes for Array Jet Impingement Cooling with Bidirectional Exits. (Under the direction of Dr. Srinath V. Ekkad).

As technology advances day by day, thermal cooling strategies are becoming more sophisticated and important in modern-day industries. From the smallest electronic chip to a huge gas turbine, the cooling strategies employed are of vital importance for the longevity of different components. Another factor is the amount of heat produced by each component. For a gas turbine blade, the leading edge of the blade would be hotter than the trailing edge. Thus, the cooling channels would need to be designed to cool the leading edge of the blade more than the trailing edge. Thus, it is vital to efficiently design and adopt cooling strategies for heat transfer.

This study mainly focuses on array jet impingement cooling. This area has been researched quite a lot. However, forcing the flow to bidirectionally exit with different mass flow rates through each exit after impingement provides an interesting study. The analysis helps us to understand how the flow behaves when it is forced to exit through one exit more than the other and how the heat transfer varies for the test section due to this. Based on the simulations, it was observed that a 1:1 exit provides the highest heat transfer on the test section compared to 1:2, 1:3, and single exits.

© Copyright 2023 by Ganesh Subbarama Iyer

All Rights Reserved

Effects of Different Cross Flow Schemes for Array Jet Impingement Cooling with Bidirectional Exits.

by
Ganesh Subbarama Iyer

A Thesis submitted to the Graduate Faculty of
North Carolina State University
in partial fulfillment of the
requirements for the degree of
Master of Science

Mechanical Engineering

Raleigh, North Carolina
2023

APPROVED BY:

Dr. Chi-An Yeh

Dr. Tarek Echehki

Dr. Srinath V. Ekkad
Committee Chair

DEDICATION

I dedicate this to my parents, my family, and my friends.

BIOGRAPHY

Ganesh Subbarama Iyer was born in Thiruvananthapuram, Kerala, India in 1995. His parents were Subbarama Iyer G. and Rajalekshmi K. He showed a keen interest in science and mathematics during his school days. He went on to pursue his Bachelor's degree in Mechanical Engineering from the College of Engineering Trivandrum, Kerala, India. He was part of the SAE-INDIA CET, participated in various activities, and developed an interest in Thermal Engineering. He participated in projects to design, analyze and fabricate an Einstein-Szilard based refrigerator. Post his graduation, he went on to join Accenture to get some industry experience. Though he was working in the IT industry, he still had the same interest and passion for Mechanical Engineering. He joined NC State University to continue his education in Mechanical Engineering after the COVID-19 pandemic. He was interested in heat transfer and went on to join Dr. Srinath V. Ekkad and his research team to study and research gas turbine heat transfer and combustion.

ACKNOWLEDGMENTS

I would like to thank Dr. Srinath V. Ekkad for providing me with an opportunity to work with him in the ThERMaL Lab and the project. The experience obtained from working with his students under Dr. Ekkad's guidance helped me enhance my knowledge in Thermal Engineering, specifically, combustion and heat transfer. Especially when I would encounter problems during different phases of the project, he would guide me and give me lots of different perspectives and options to solve the problem. I would also like to thank my lab colleagues, Michael, Meghna, Madhusudan, Pratik, Ben, Shoaib, and Obinna for their help whenever I needed it in the lab.

I would also like to thank my family and friends, Vishnu, Vaishnavi, Akash, Moses, Shakthi, Sneha, Uma, Aravindan, and Divya for constantly supporting me throughout my courses and my project.

TABLE OF CONTENTS

LIST OF TABLES	vi
LIST OF FIGURES	vii
Chapter 1: Introduction	1
1.1 Classification of Jet Impingement Configurations	1
1.2 Studies on Array Jet Impingement with Bidirectional Exits	4
1.3 Layout of the Thesis.....	8
Chapter 2: Numerical Simulations - Setup	10
2.1 Design of Models for Simulation.....	11
2.2 Meshing.....	16
2.3 ANSYS Fluent Model Setup.....	17
2.3.1 Turbulence Models	17
2.3.2 Boundary Conditions	17
2.3.3 Solution Methods	18
2.3.4 Post-Processing of Results	19
Chapter 3: Results and Discussions	20
3.1 Temperature Distribution for the different configurations	20
3.1.1 Single Exit Model Temperature Distribution	20
3.1.2 Bidirectional Exit Model Temperature Distribution.....	25
3.2 Nusselt Number based on Area-Averaged Temperature	34
3.2.1 Single Exit Configuration	34

3.2.2 Bidirectional Exit Configurations	36
3.3 Spanwise Nusselt Number	38
3.3.1 Single Exit Configuration	38
3.3.2 Bidirectional Exit Model.....	44
3.4 Overall Nusselt Number for the Region of Interest	64
3.5 Nusselt Number Contours.....	67
Chapter 4: Conclusion	69
Chapter 5: Future Work	70
Nomenclature	72
References	74
Appendices	77
Appendix A: Example for multizone mesh used for 0.25 inch plate ($z/D = 4$)	78

LIST OF TABLES

Table 2.1	Orifice Plate Configuration Parameters	12
Table 2.2	Test Conditions in Fluent	19

LIST OF FIGURES

Figure 1.1	Single Jet Impingement Schematic Diagram.	2
Figure 1.2	Inline Array Jet Configuration	3
Figure 1.3	Staggered Array Jet Configuration.....	3
Figure 1.4	Nusselt Number vs. Reynolds Number for different turbulence models	5
Figure 1.5	Spanwise Averaged Nusselt Number vs. Streamwise Location for inline configuration	6
Figure 1.6	Spanwise Averaged Nusselt Number vs. Streamwise Location for staggered configuration	8
Figure 2.1	Simulation Model used for array jet impingement simulations.	10
Figure 2.2	Simulation Model used for array jet impingement simulations	11
Figure 2.3	0.25 inch diameter inline configuration	13
Figure 2.4	0.33 inch diameter inline configuration	13
Figure 2.5	0.5 inch diameter inline configuration	14
Figure 2.6	0.25 inch diameter staggered configuration	14
Figure 2.7	0.33inch diameter staggered configuration	15
Figure 2.8	0.5 inch diameter staggered configuration	15
Figure 3.1	Temperature distribution for single exit (exit at left side) inline grid model ($z/D = 2$) with a mass flow rate of 32 g/s	20
Figure 3.2	Temperature distribution for single exit (exit at left side) inline grid model ($z/D = 2$) with a mass flow rate of 64 g/s	21
Figure 3.3	Temperature distribution for single exit inline (exit at left side) grid model ($z/D = 2$) with a mass flow rate of 96 g/s	21
Figure 3.4	Temperature distribution for single exit staggered (exit at left side) grid model ($z/D = 2$) with a mass flow rate of 32 g/s	22
Figure 3.5	Temperature distribution for single exit staggered (exit at left side) grid model ($z/D = 2$) with a mass flow rate of 64 g/s	23

Figure 3.6	Temperature distribution for single exit staggered (exit at left side) grid model ($z/D = 2$) with a mass flow rate of 96 g/s	23
Figure 3.7	Temperature distribution for single exit inline (exit at left side) grid model ($z/D = 4$) with a mass flow rate of 32 g/s	24
Figure 3.8	Temperature distribution for single exit inline (exit at left side) grid model ($z/D = 3$) with a mass flow rate of 32 g/s	25
Figure 3.9	Temperature distribution for bidirectional exit (1:1 exit at left and right) inline grid model ($z/D = 2$) with a mass flow rate of 32 g/s.....	26
Figure 3.10	Temperature distribution for bidirectional exit (1:1 exit at left and right) inline grid model ($z/D = 2$) with a mass flow rate of 64 g/s.....	26
Figure 3.11	Temperature distribution for bidirectional exit (1:1 exit at left and right) inline grid model ($z/D = 2$) with a mass flow rate of 96 g/s.....	27
Figure 3.12	Temperature distribution for bidirectional exit (1:2 exit with higher mass flow exit at the left) inline grid model ($z/D = 3$) with a mass flow rate of 32 g/s	28
Figure 3.13	Temperature distribution for bidirectional exit (1:2 exit with higher mass flow exit at the left) inline grid model ($z/D = 3$) with a mass flow rate of 64 g/s	29
Figure 3.14	Temperature distribution for bidirectional exit (1:2 exit with higher mass flow exit at the left) inline grid model ($z/D = 3$) with a mass flow rate of 96 g/s	29
Figure 3.15	Temperature distribution for bidirectional exit (1:3 exit with higher mass flow exit at the left) inline grid model ($z/D = 3$) with a mass flow rate of 32 g/s	30
Figure 3.16	Temperature distribution for bidirectional exit (1:3 exit with higher mass flow exit at the left) inline grid model ($z/D = 3$) with a mass flow rate of 64 g/s	31
Figure 3.17	Temperature distribution for bidirectional exit (1:3 exit with higher mass flow exit at the left) inline grid model ($z/D = 3$) with a mass flow rate of 96 g/s	31
Figure 3.18	Temperature distribution for bidirectional exit (1:1 exit at left and right) staggered grid model ($z/D = 2$) with a mass flow rate of 32 g/s	32
Figure 3.19	Temperature distribution for bidirectional exit (1:2 exit with higher mass flow exit at the left) staggered grid model ($z/D = 3$) with a mass flow rate of 96 g/s.....	33
Figure 3.20	Temperature distribution for bidirectional exit (1:3 exit with higher mass flow exit at the left) staggered grid model ($z/D = 3$) with a mass flow rate of 64 g/s.....	33

Figure 3.21 Nusselt Number (using Area Averaged Temperature) vs. Reynolds Number for a single exit jet impingement configuration	35
Figure 3.22 Nusselt Number (using Area Averaged Temperature) vs. Reynolds Number for a bidirectional exit inline jet impingement configuration	36
Figure 3.23 Nusselt Number (using Area Averaged Temperature) vs. Reynolds Number for a bidirectional exit staggered jet impingement configuration	37
Figure 3.24 Spanwise Nusselt Number for inline grid configuration for $z/D = 2$	39
Figure 3.25 Spanwise Nusselt Number for staggered grid configuration for $z/D = 2$	40
Figure 3.26 Spanwise Nusselt Number for inline grid configuration for $z/D = 3$	41
Figure 3.27 Spanwise Nusselt Number for staggered grid configuration for $z/D = 3$	42
Figure 3.28 Spanwise Nusselt Number for inline grid configuration for $z/D = 4$	43
Figure 3.29 Spanwise Nusselt Number for staggered grid configuration for $z/D = 4$	44
Figure 3.30 Spanwise Nusselt Number distribution for 1:1 mass flow inline configuration ($z/D = 2$)	45
Figure 3.31 Spanwise Nusselt Number distribution for 1:2 mass flow inline configuration ($z/D = 2$)	46
Figure 3.32 Spanwise Nusselt Number distribution for 1:3 mass flow inline configuration ($z/D = 2$)	47
Figure 3.33 Spanwise Nusselt Number distribution for 1:1 mass flow inline configuration ($z/D = 4$)	49
Figure 3.34 Spanwise Nusselt Number distribution for 1:2 mass flow inline configuration ($z/D = 4$)	50
Figure 3.35 Spanwise Nusselt Number distribution for 1:3 mass flow inline configuration ($z/D = 4$)	51
Figure 3.36 Spanwise Nusselt Number distribution for 1:1 mass flow inline configuration ($z/D = 3$)	52
Figure 3.37 Spanwise Nusselt Number distribution for 1:2 mass flow inline configuration ($z/D = 3$)	53

Figure 3.38 Spanwise Nusselt Number distribution for 1:3 mass flow inline configuration ($z/D = 3$)	54
Figure 3.39 Spanwise Nusselt Number distribution for 1:1 mass flow staggered configuration ($z/D = 2$).....	55
Figure 3.40 Spanwise Nusselt Number distribution for 1:2 mass flow staggered configuration ($z/D = 2$).....	56
Figure 3.41 Spanwise Nusselt Number distribution for 1:3 mass flow staggered configuration ($z/D = 2$).....	57
Figure 3.42 Spanwise Nusselt Number distribution for 1:1 mass flow staggered configuration ($z/D = 4$).....	58
Figure 3.43 Spanwise Nusselt Number distribution for 1:2 mass flow staggered configuration ($z/D = 4$).....	59
Figure 3.44 Spanwise Nusselt Number distribution for 1:3 mass flow staggered configuration ($z/D = 4$).....	60
Figure 3.45 Spanwise Nusselt Number distribution for 1:1 mass flow staggered configuration ($z/D = 3$).....	61
Figure 3.46 Spanwise Nusselt Number distribution for 1:2 mass flow staggered configuration ($z/D = 3$).....	62
Figure 3.47 Spanwise Nusselt Number distribution for 1:3 mass flow staggered configuration ($z/D = 3$).....	63
Figure 3.48 Overall Nusselt Number comparison with existing Literature.....	64
Figure 3.49 Overall Nusselt number vs. Reynolds number for inline configurations	65
Figure 3.50 Overall Nusselt number vs. Reynolds number for staggered configurations.....	66
Figure 3.51 Nusselt number contours for inline configuration for $z/D = 4$ with $Re = 10000$ for different mass flow rate exits (higher mass flow exit at the left side), (a) 1:0, (b) 1:1, (c) 1:2, (d) 1:3	67
Figure 3.52 Nusselt number contours for staggered configuration for $z/D = 4$ with $Re = 10000$ for different mass flow rate exits (higher mass flow exit at the left side), (a) 1:0, (b) 1:1, (c) 1:2, (d) 1:3	68

CHAPTER 1

INTRODUCTION

The relevance of heat transfer, especially cooling is becoming vital for all industries. Jet impingement is one such technique that is predominantly used in the gas turbine and electronic industries. Jet impingement is predominantly useful for cooling surfaces where heat is concentrated in a localized area. For example, a modern microchip or processor, which would be only a few millimeters in size, would require thermal management because of the heat dissipation due to its high processing power. Considering the gas turbine industries, jet impingement techniques have proven effective for the design of cooling channels such that the jets impinge on the leading edge of the gas turbine blade internally.

1.1 Classification of Jet Impingement Configurations

There are different ways of classifying jet impingements. The jets can be classified based on the number of jets, the angle at which the jet holes are designed, and based on the types of exits.

Based on the number of jets, the jets can be classified into array jets and single jets. A single jet, as the name suggests, has a single jet impinging on the target surface. Single jets can be used only when the target surface has a heat concentration only at one point for effective heat transfer.

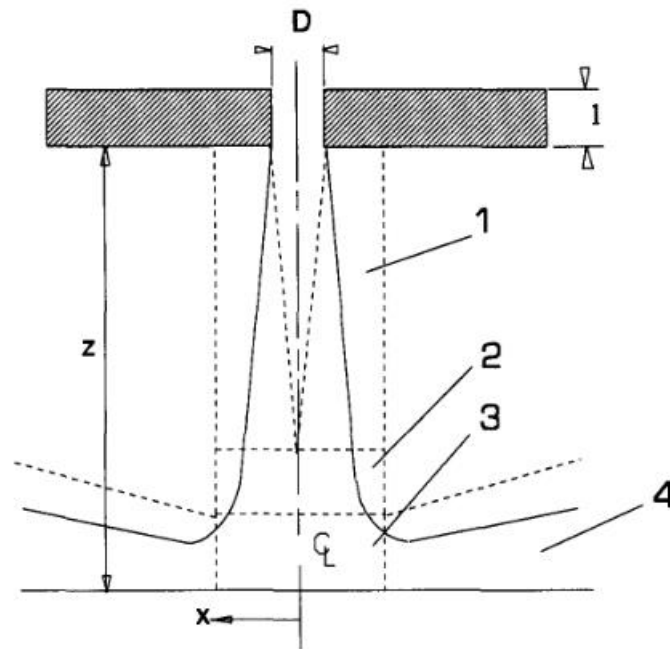


Figure 1.1: Single Jet Impingement Schematic Diagram. [1]

Figure 1.1 shows a single jet impingement configuration where the jet enters through a hole of Diameter D and impinges on the target surface which is at a distance of z from the hole. The jet becomes a wall jet once it impinges on the test section and moves in the positive and negative X direction.

An array jet, on the other hand, has multiple jet holes leading to a large number of jets impinging on the test section instead of one. Based on the arrangement of the jet holes, the jets can be further classified into staggered and inline jets.

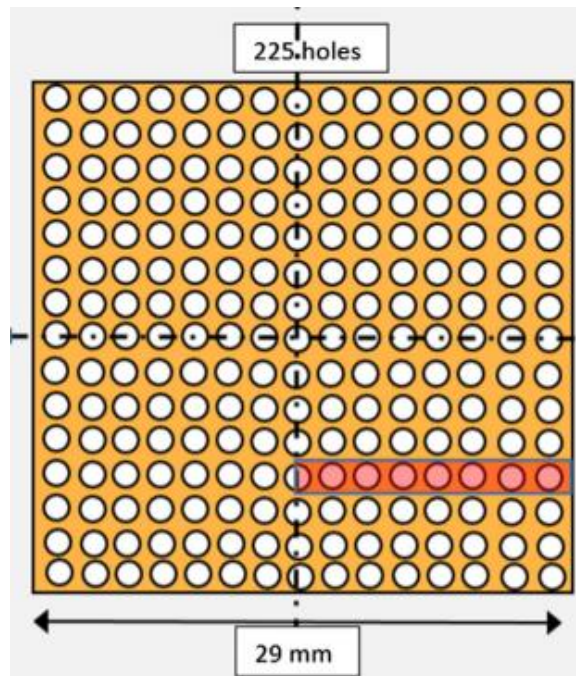


Figure 1.2: Inline Array Jet Configuration. [2]

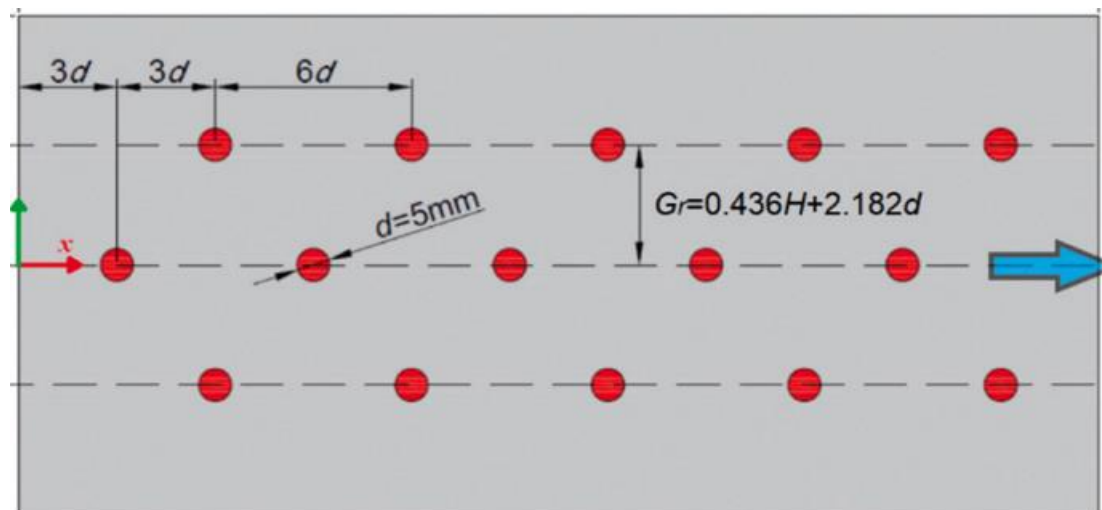


Figure 1.3: Staggered Array Jet Configuration. [3]

Figure 1.2 shows an inline grid of jet holes where each hole is arranged uniformly in the X and Y directions. The staggered grid as shown in Figure 1.3 has the holes aligned uniformly in one direction and moved by half the hole spacing in the other direction. The jet characteristics will be mainly dependent on the number of holes, the hole spacing, and the hole diameter.

Another classification will be based on the angle of the jet holes. If the jet hole axis is at 90 degrees with respect to the target surface, then the holes are classified as orthogonal jets. If the angle is not 90 degrees, then jets are called angled jets[4].

Based on the number and type of exits, the jets are classified into single-exit jet impingement, bidirectional exit jet impingement, and multidirectional exit jet impingement configurations.

1.2 Studies on Array Jet Impingement with Bidirectional Exits

Array Jet Impingement has been extensively studied for different jet configurations and jet orifice orientations. However, most of the studies have been based on a single-directional exit or a bidirectional exit where the mass flow rates are equal at both exits.

Early studies [5], [6] by NASA have shown array jet impingement to be an effective method of cooling. The experimental setup has been used to calculate heat performance for Reynolds numbers ranging from 5000 to 50000. Inline and staggered configurations have been analyzed with different hole diameters and spacing. The studies show that the Nusselt numbers decrease with an increase in the z/D ratio. The local maximas for Nusselt numbers also increase with an increase in jet diameter.

Studies for different cross-flow orientations have been conducted experimentally and numerically. Based on the literature [7], the heat transfer performance for array jet impingement for a single-directional exit configuration is compared with bidirectional exit configurations using Liquid Crystal Thermography. The inlet of the jet, however, is parallel to the jet impingement orifice plate in this case. With increasing Reynolds number, the heat transfer coefficient increases for the different crossflow orientations. The distance between the jet orifice plate to the target plate

is three times the hole diameter providing a z/D ratio of 3. The results show a higher heat transfer performance for the bidirectional exit configuration compared to the single exit configurations.

The effect of staggered holes for narrow impingement channels has been studied in the literature [8] [9] [10]. It is observed that inline configurations provide better heat transfer compared to the staggered grid configurations for single-exit jet impingement configurations. Other studies [11] also compare the effect of different jet diameters, spacing, and jet orifice plate to test section distances. A correlation is developed for finding the Nusselt number. Another study [12] shows an increase in Nusselt number by adding U-shaped crossflow diverters to the orifice plate to divert the jet onto the target plate.

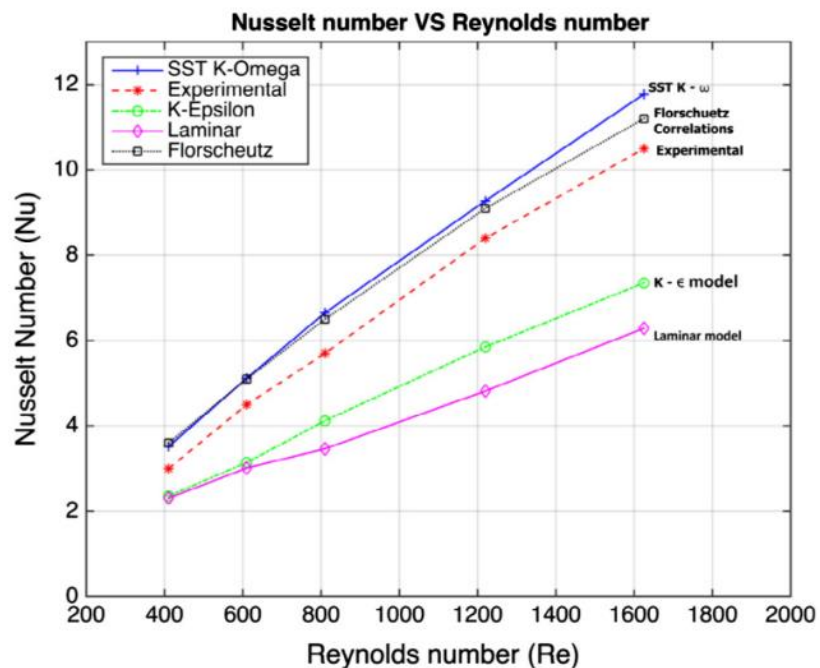


Figure 1.4: Nusselt Number vs. Reynolds Number for different turbulence models. [2]

Numerical simulations of array jet impingement configurations also provide useful insight into the behavior of the jets and the heat transfer performance for different jet configurations and exit orientations. One of the most important setups required for modeling and analyzing the different numerical models is the turbulence models available in various CFD software. Studies

[2] [13] show the heat transfer results for the different turbulence models such as the $k-\epsilon$ model, SST $k-\omega$ model, and the laminar model. Results show an improved prediction of the flow and heat transfer for the SST $k-\omega$ model because of a more accurate boundary layer prediction due to the wall treatment functionality used for the numerical diffusion term near the walls. The study also explains that the SST $k-\omega$ model will overpredict the thermal performance of the array jets whereas the other 2 models underpredict the results. Figure 1.4 shows the different results based on different turbulent models.

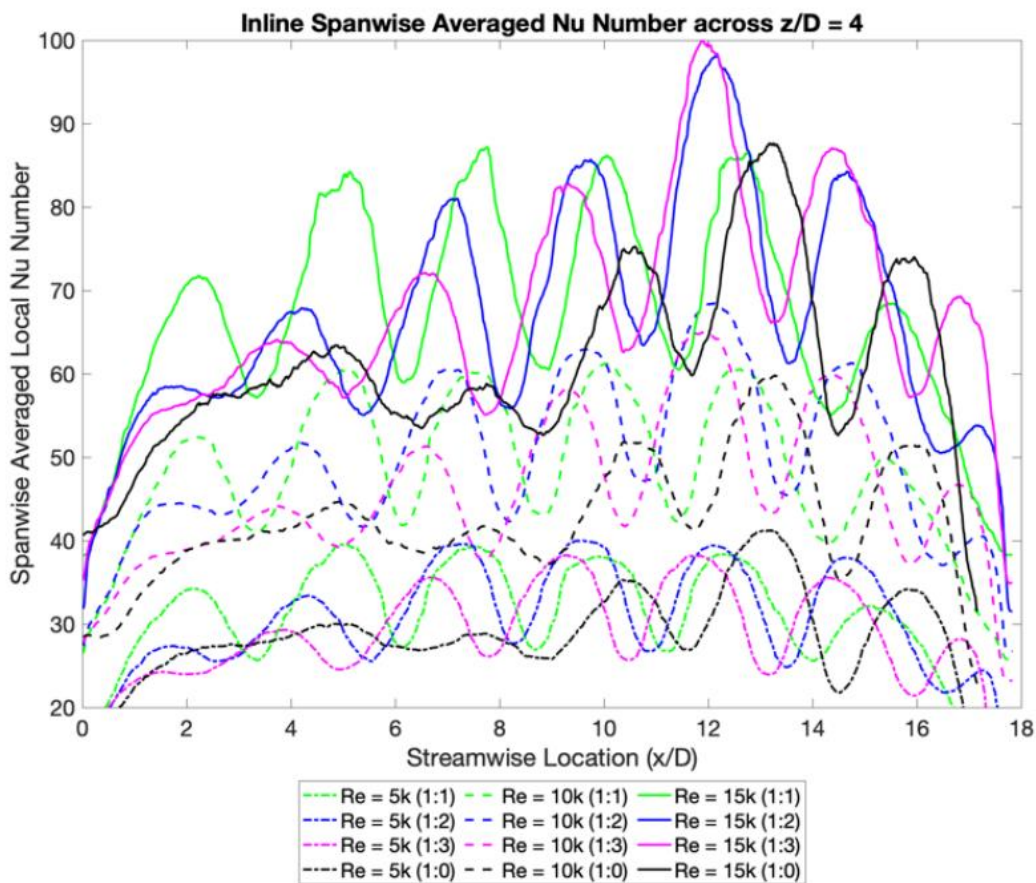


Figure 1.5: Spanwise Averaged Nusselt Number vs. Streamwise Location for inline configuration

Studies on cross-flow configurations with different mass flow rate exits by varying back pressure of the exits are limited. Literature [14] explains the study on varying mass flow exits by adjusting backflow pressure to control the mass flow through each exit. The study shows that mass flow exiting with a 1:1 ratio through each exit provides the maximum heat transfer performance compared to a single exit or a bidirectional exit with a mass flow exit ratio of 1:2 or 1:3. The experiment is done using a plexiglass test section coated with Liquid Crystals. The transient temperature readings are observed based on the change in color of the TLC and, the heat transfer coefficient is calculated using the 1-D semi-infinite model by assuming that the heat transfer is only in one direction. Figure 1.5 shows the variation of the Nusselt number with the streamwise location for inline configurations, which shows the comparison between the different mass flow exit ratios for staggered and inline configurations. It can be observed that the maximum average Nusselt number can be observed for the 1:1 configuration where the jets are more uniformly spread out across the test section.

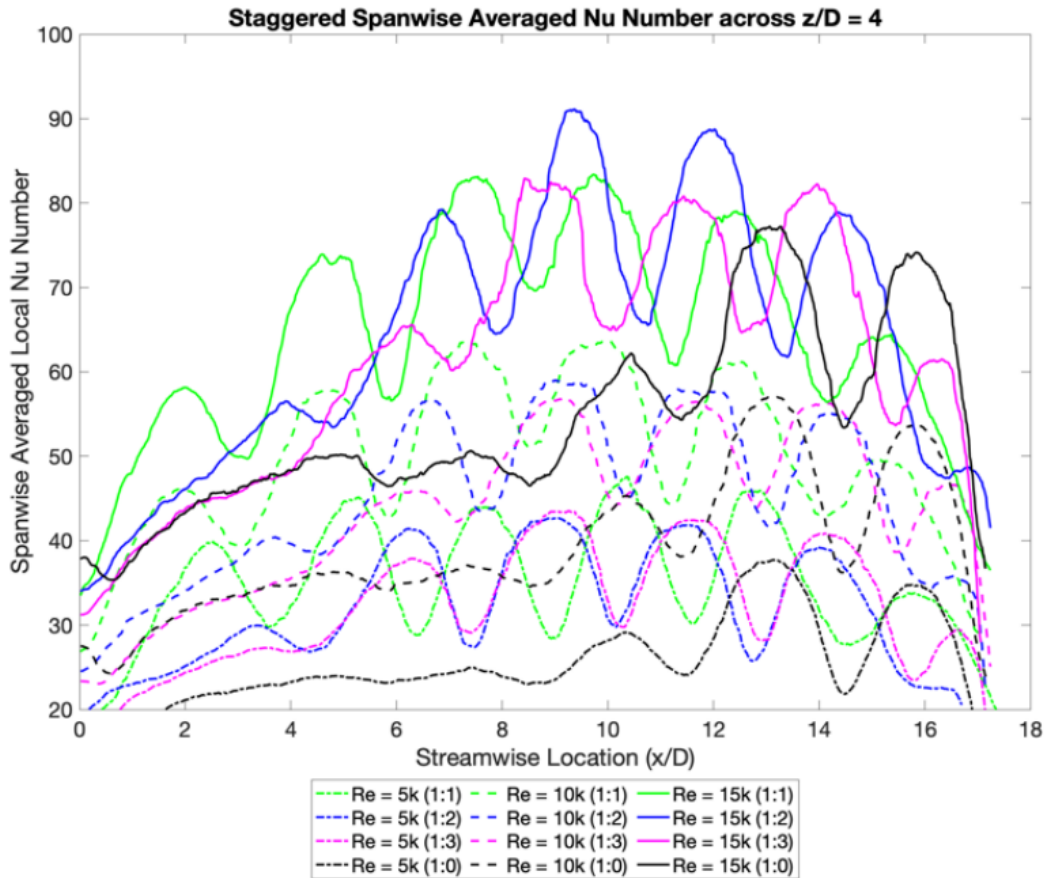


Figure 1.6: Spanwise Averaged Nusselt Number vs. Streamwise Location for staggered configuration

Similarly, Figure 1.6 shows similar characteristics of the jets for staggered configurations. However, the Nusselt number for the inline configurations is relatively higher compared to the staggered grid results.

1.3 Layout of the Thesis

The thesis majorly deals with the different crossflow exit configurations by varying the mass flow rates through each exit. Numerical Simulations are performed in ANSYS Fluent to study the different models for inline and staggered grid configurations. Chapter 2 explains the numerical model setup for the different configurations and the parameters used to study the flow characteristics and thermal performance. Chapter 3 discusses the results obtained from the

different numerical simulations and the comparison of the simulations with experimental results from different studies.

CHAPTER 2

NUMERICAL SIMULATIONS – SETUP

The numerical model for the different jet impingement crossflow configurations has been set up primarily using ANSYS software. ANSYS SpaceClaim has been used to set up the fluid domain and the orifices for the jet orifice plate. ANSYS meshing tool is used for meshing the different models and ANSYS Fluent and CFD-Post have been used to analyze the different models and classify the results.

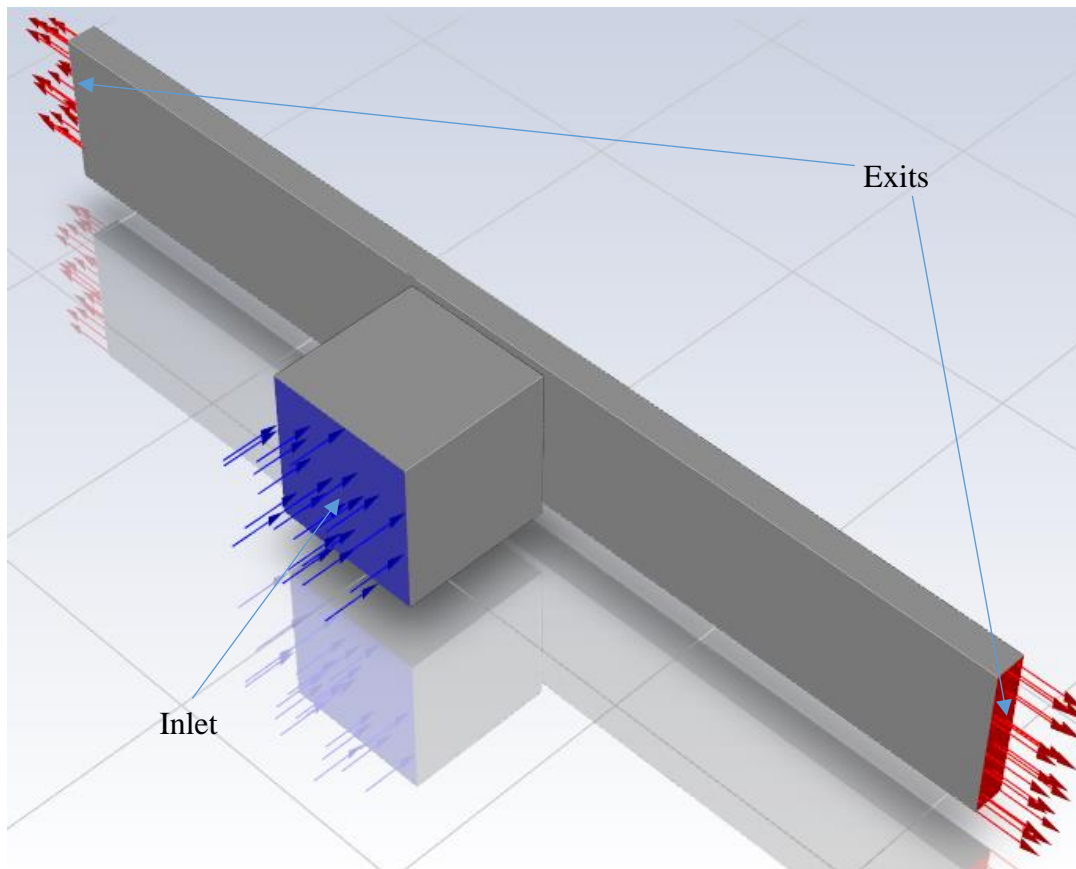


Figure 2.1: Simulation Model used for array jet impingement simulations

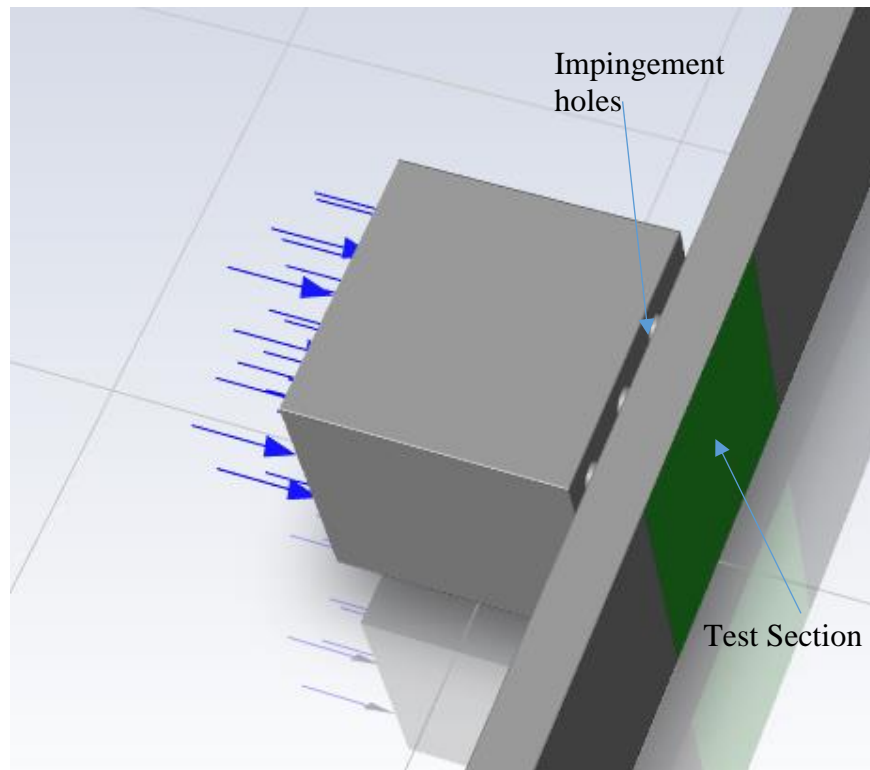


Figure 2.2: Simulation Model used for array jet impingement simulations

Figure 2.1 and Figure 2.2 shows the simulation model (fluid domain) used for the numerical simulations. The inlet, exits, orifice holes, and test sections are marked for better clarity on the model. The orifice holes differ for each model based on the diameter of the jets and the jet configuration used, i.e., inline, or staggered.

2.1 Design of models for simulation

ANSYS SpaceClaim has been used to model the configurations for simulation. The model is created based on the experimental setup used for a similar study. The orifice plate has a length of 5.125 in and a width of 5 in. The plate has a width of 0.25 in. The axes of the orifices are perpendicular to the test section plate since the analysis is based on orthogonal jets.

3 different orifice diameters are analyzed in the thesis. The diameters are decided based on the z/D ratios (distance of orifice plate to test section to orifice diameter ratio) of 2, 3, and 4. The

distance between the orifice plate and the test section is kept at a constant value of 1 in. The diameters of the orifices, therefore, are calculated as 0.5 in, 0.33 in, and 0.25 in respectively. The different parameters of the models are tabulated in Table 2.1.

Table 2.1: Orifice Plate Configuration Parameters

Plate Number	Orifice Diameter (mm)	Orifice Diameter (inches)	Spacing	Number of Jets	Configuration Type
1	12.7	0.5	1.4	32	Inline
2	12.7	0.5	1.4	32	Staggered
3	8.467	0.33	1.9	48	Inline
4	8.467	0.33	1.9	48	Staggered
5	6.35	0.25	2.2	64	Inline
6	6.35	0.25	2.2	64	Staggered

The inlet section before the orifice plate and the test section plate has the same length and width as the orifice plate itself. An entry length of 5 inch has been fixed for the model. The exits have dimensions of 1 inch by 5.125 inch respectively. The exit section after the test section is 15 inch long to ensure a uniform flow at the exit.

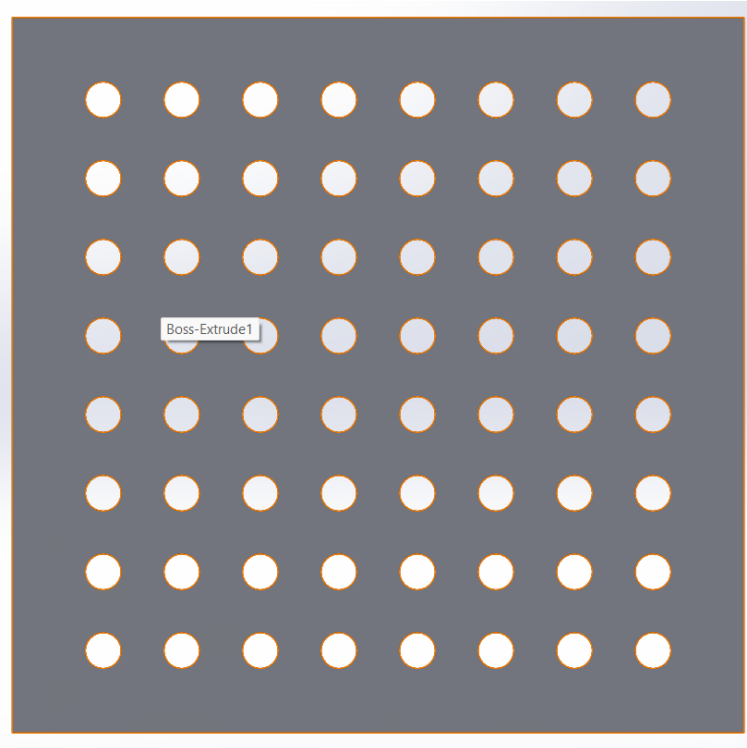


Figure 2.3: 0.25 inch diameter inline configuration

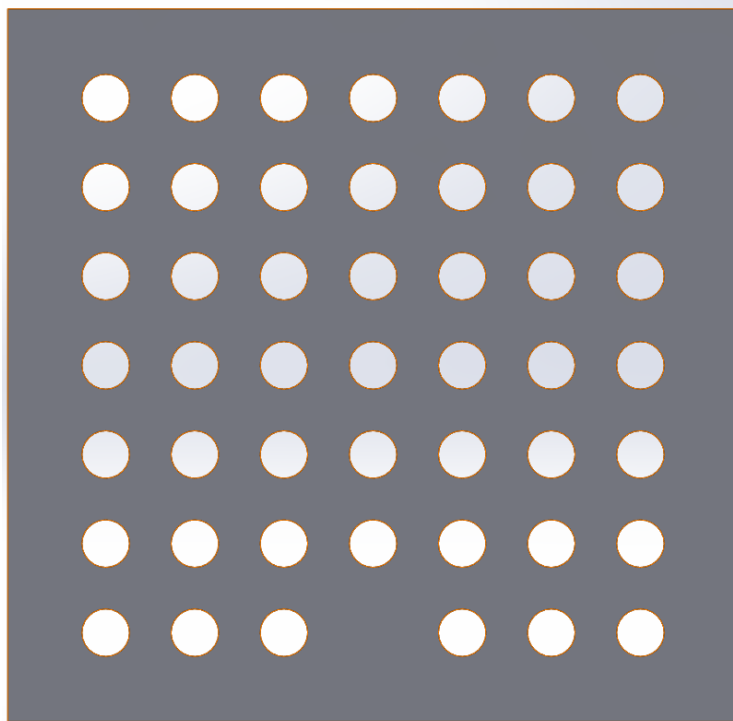


Figure 2.4: 0.33 inch diameter inline configuration

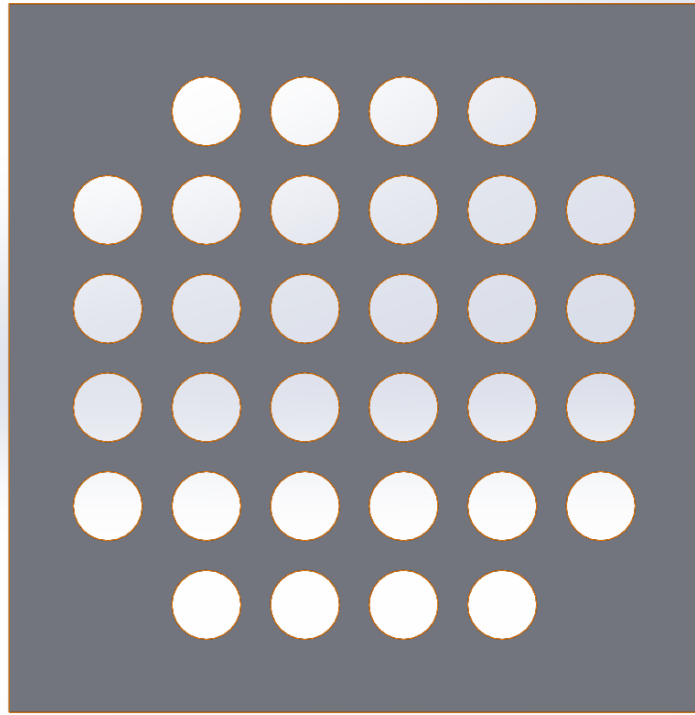


Figure 2.5: 0.5 inch diameter inline configuration

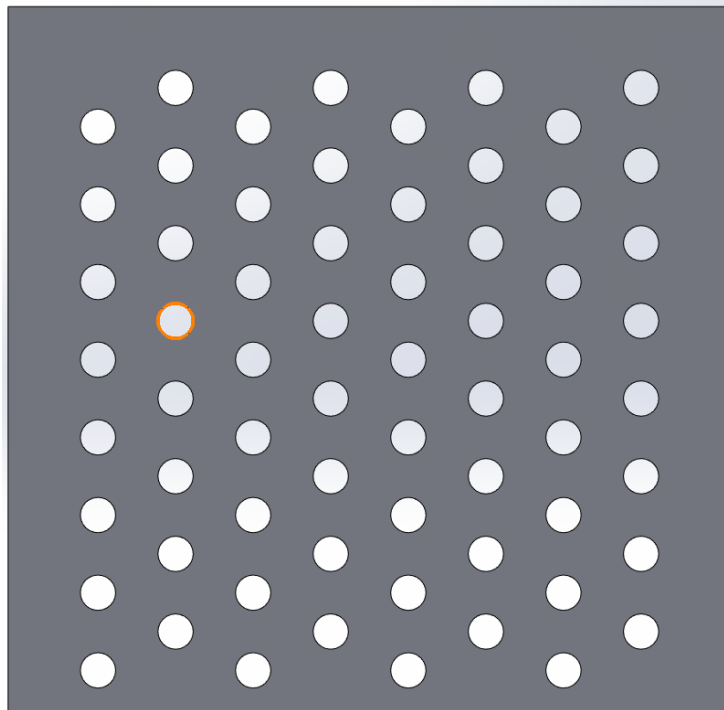


Figure 2.6: 0.25 inch diameter staggered configuration

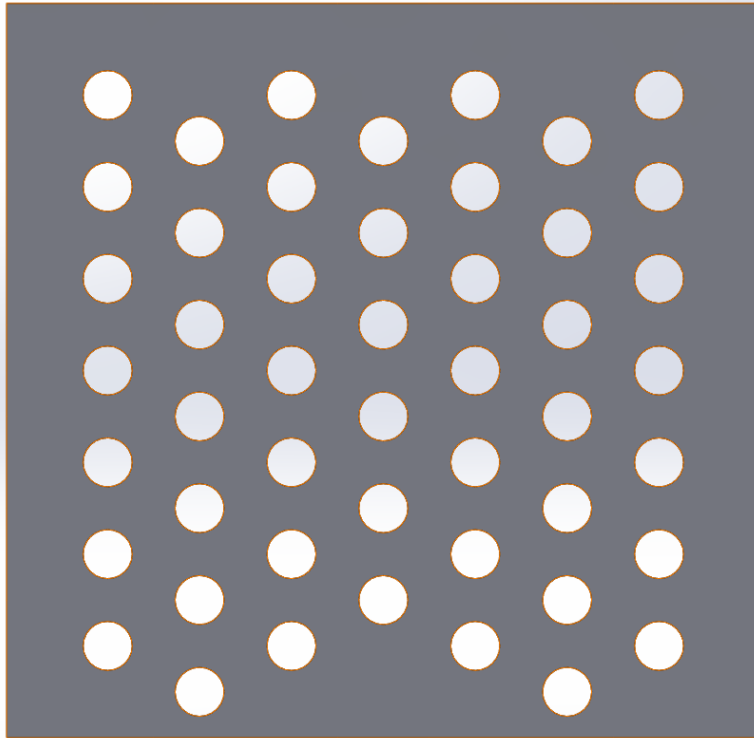


Figure 2.7: 0.33 inch diameter staggered configuration

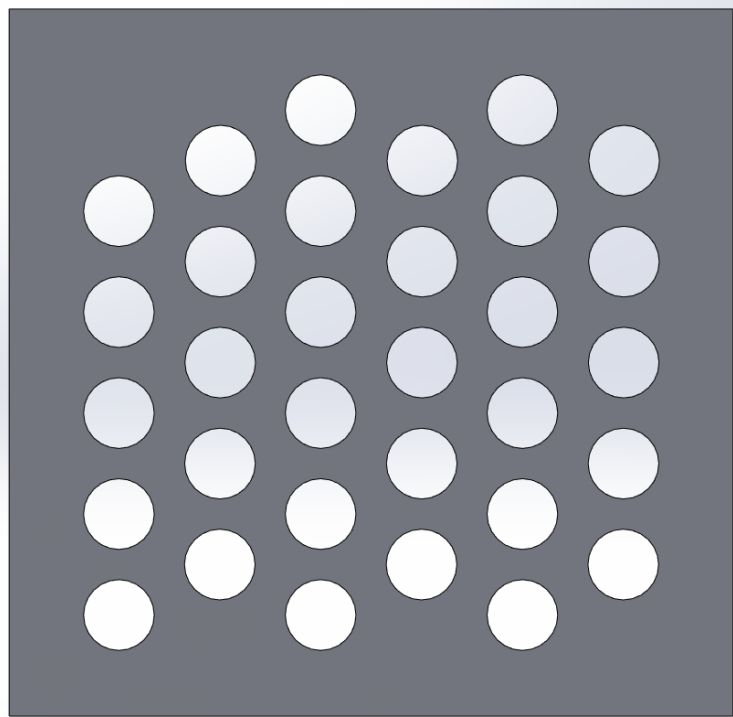


Figure 2.8: 0.5 inch diameter staggered configuration

The mass flow rates used for the simulations are 32 g/s, 64 g/s, and 96 g/s. Based on the mass flow rates, the Reynolds numbers used in the simulations are in the range of 5000, 10000, and 15000 respectively. The number of holes for each orifice plate is based total area of the orifices being kept as a constant. The number of holes for the different diameters is calculated as 64 (for 0.25 in dia.), 48 (for 0.33 in dia.), and 32 (for 0.5 in dia.). Figures 2.3 to 2.8 shows the difference orifice plates for the inline and staggered configurations used for the simulation models.

2.2 Meshing

ANSYS Meshing Tool is used for meshing the different models for simulation. The different parts of the model are modeled based on the type of flow. Multizone meshing is used for all the models since the mesh captures the jets better, thereby leading to faster convergence and better simulation results for the various runs.

The initial part of the inlet section and the section near the exit have been meshed with a 5 mm mesh which is a coarse mesh compared to the rest of the geometry. The section close to the orifice plate (before and after) is meshed with a 1 mm mesh for capturing better turbulence of the fluid. The orifice holes are meshed with a finer mesh of 0.5 mm mesh. Inflation layers have been added on all the walls where there would be boundary layers. This ensures a lower y^+ , and accurate prediction of data near the walls. Along with this, the SST $k-\omega$ model provides further accuracy due to wall treatment functionality in ANSYS Fluent. As shown in the figure, the multizone mesh ensures a finer mesh along the line of the orifice until the test section so that the jets are captured better, and the results are predicted more accurately.

2.3 ANSYS Fluent Model Setup

Once meshing is completed, the models are imported into Fluent. The simulations performed are all steady-state simulations. The current problem is a conjugate heat transfer problem.

2.3.1 Turbulence Models

The model used in the current models is the SST k- ω model which uses the near wall treatment using the k- ω formulation for accurate prediction of the boundary layer along with the prediction of the k- ϵ model for the free stream part of the model[15]. Compared to the standard k- ω model which uses only k- ω formulation for the entire fluid region, the SST k- ω model combines both the k- ω and the k- ϵ formulations for more accurate predictions of the fluid flow.

The SST k- ω model uses the below transport equations for the numerical simulations by using the turbulent kinetic energy and the dissipation rate.

$$\frac{\partial}{\partial t}(\rho k) + \frac{\partial}{\partial x_i}(\rho k u_i) = \frac{\partial}{\partial x_j} \left(\tau_k \frac{\partial k}{\partial x_j} \right) + \tilde{G}_k - Y_k + S_k \quad (\text{Equ. 2.1})$$

$$\frac{\partial}{\partial t}(\rho \omega) + \frac{\partial}{\partial x_i}(\rho \omega u_i) = \frac{\partial}{\partial x_j} \left(\tau_\omega \frac{\partial \omega}{\partial x_j} \right) + \tilde{G}_\omega - Y_\omega + S_\omega \quad (\text{Equ. 2.2})$$

2.3.2 Boundary Conditions

The test section is modeled as a wall with a heat flux of 2000 W/m². The fluid used in the simulations is air at 300 K. The inlet mass flow rates are provided as 32 g/s, 64 g/s and 96 g/s. The exits are mainly dependent on the mass flow rates exiting through both sides based on the mass flow ratio for the exits, namely, 1:1, 1:2, or 1:3. To fix the mass flow at the exit, the outflow condition is used in Fluent which allows fixing the percentage of mass exiting through each exit.

Based on the weightage provided for each exit, pressure, mass flow rate and other properties are predicted based on each iteration run.

This boundary condition is optimal for the problem because other boundary conditions such as a fixed mass flow outlet, velocity outlet or pressure outlet, forces the mass flow rates at the exits to be fixed leading to inaccurate prediction of the flow. Due to turbulence in the flow after impingement, the initial runs can show a backflow from the exits which is accurately predicted in the outflow condition which allows the pressure to be adjusted initially and then recalculated as the flow approaches a steady state.

The external walls of the fluid domain are provided with an adiabatic condition so that there is no heat loss through any other walls except the test section wall. Also, since all the walls are considered to be zero thickness, the material of the wall does not play a huge part in the determination of the heat transfer coefficient and Nusselt number.

2.3.3 Solution Methods

Since the analysis is done using a pressure-based solver, the SIMPLEC method is used for the velocity-pressure coupling. The Coupled solver is not used in this problem because of fixed mass flow rates at exits and inlets because of the problem definition leading to slow convergence and more computation time. The SIMPLEC method uses the SIMPLE algorithm with a face flux correction which helps in the accurate prediction of the flow with faster convergence.

The SIMPLE algorithm uses mass conservation along with velocity-pressure correlations to calculate the pressure field. The momentum equations are solved using a guessed pressure field. Further, the face flux is calculated using the guessed pressure field using the discretized continuity equation. The SIMPLEC method adds a correction term to the face flux calculated from the

SIMPLE algorithm if the face flux does not satisfy the continuity equation. The correction term is defined differently in the SIMPLE and SIMPLEC methods.

Table 2: Test Conditions in Fluent

Reynolds Number	5000, 10000 and 15000
Outflow mass weighting	1:0, 1:1, 1:2 and 1:3
Heat Flux on Test Section	2000 W/m ²
Materials used	Aluminum, air
Inlet	32 g/s, 64 g/s and 96 g/s

The convergence criteria are determined based on the temperature convergence of the test section along with mass convergence residuals of 10^{-3} and energy convergence residuals of 10^{-6} .

Table 2 shows all the test conditions which are simulated.

2.3.4 Post-Processing of Results

Since the problem is directly being analyzed using a zero-thickness wall with a constant heat flux of 2000 W/m², the heat transfer coefficient can be directly calculated using the heat flux equation for convection. The reference temperature used for the equation is room temperature (27 °C or 300 K). The equation used for the calculation of the heat transfer coefficient is shown below.

$$h = \frac{q''}{(T - T_{ref})} \quad (Equ. 2.3)$$

The Nusselt number is also calculated using the below equation where the characteristic length is taken as the orifice diameter for the different jet configurations and k is taken as the conductivity of air.

$$Nu = \frac{h \cdot L}{k_{air}} \quad (Equ. 2.4)$$

CHAPTER 3

RESULTS AND DISCUSSIONS

3.1 Temperature Distribution for the different configurations

The temperature contours explain the jet behavior on how they impinge on the test section of the model. The models provide insight into how heat transfer is affected when the exit mass flow rates are changed and the effect of back pressure on the thermal performance of the jets.

3.1.1 Single Exit Model Temperature Distribution

The single-exit models show a lower temperature drop near the exit side and well-defined jets at the opposite side of the test section.

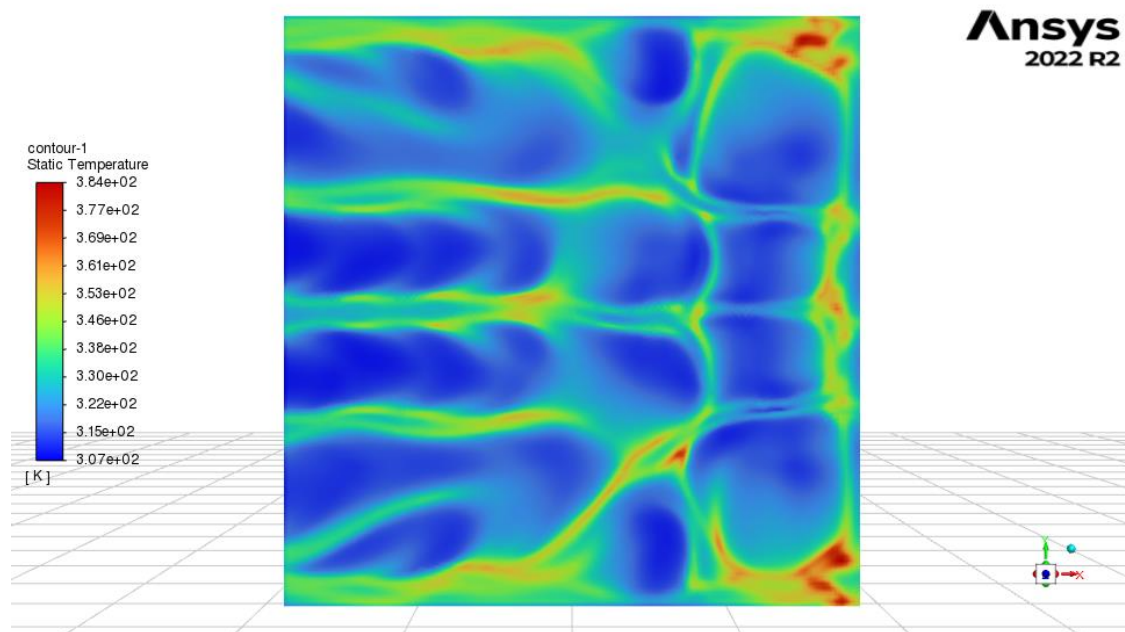


Figure 3.1: Temperature distribution for single exit (exit at left side) inline grid model ($z/D = 2$)

with a mass flow rate of 32 g/s

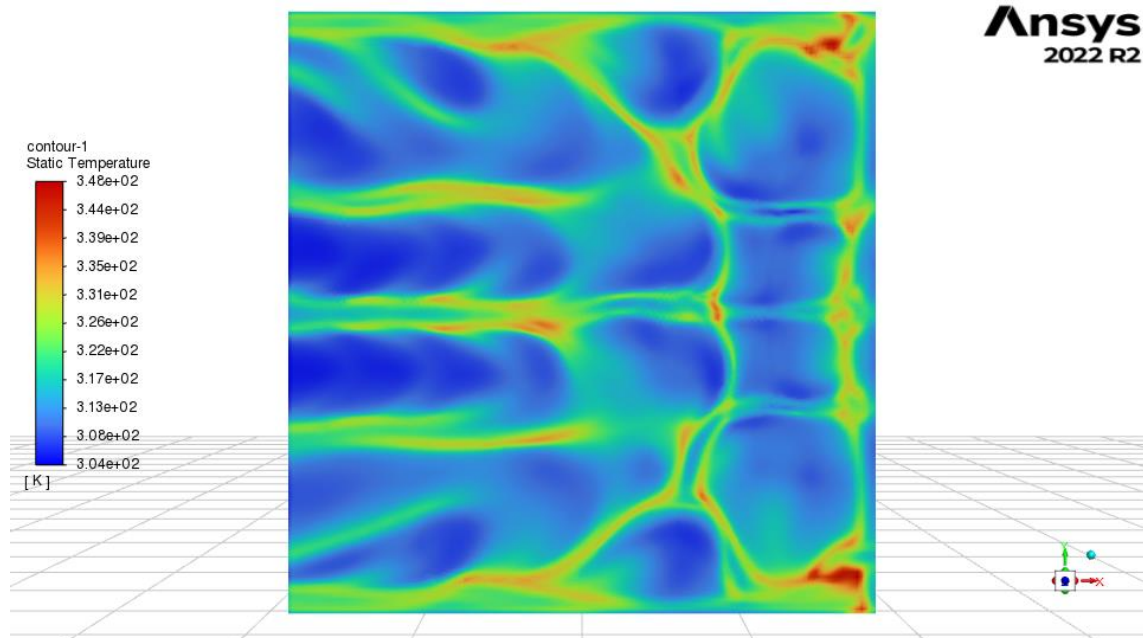


Figure 3.2: Temperature distribution for single exit (exit at left side) inline grid model ($z/D = 2$) with a mass flow rate of 64 g/s

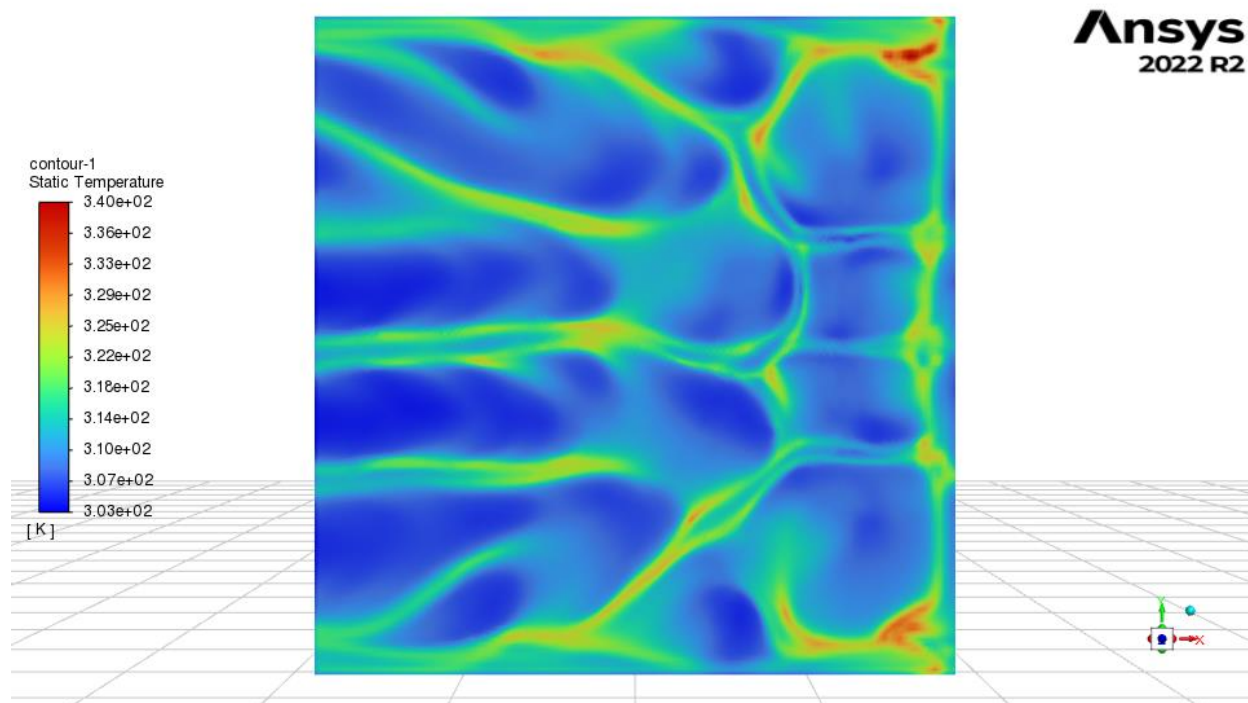


Figure 3.3: Temperature distribution for single exit inline (exit at left side) grid model ($z/D = 2$) with a mass flow rate of 96 g/s

Figures 3.1, 3.2 and 3.3 show the effect of mass flow rates on the jets. The contours look similar except for a higher temperature drop when the mass flow rate increases. As expected, for all 3 diameters ($z/D = 2, 3$ and 4), the contours are similar for different mass flow rates, but the temperature drop is higher as the mass flow rate or Reynolds number is larger.

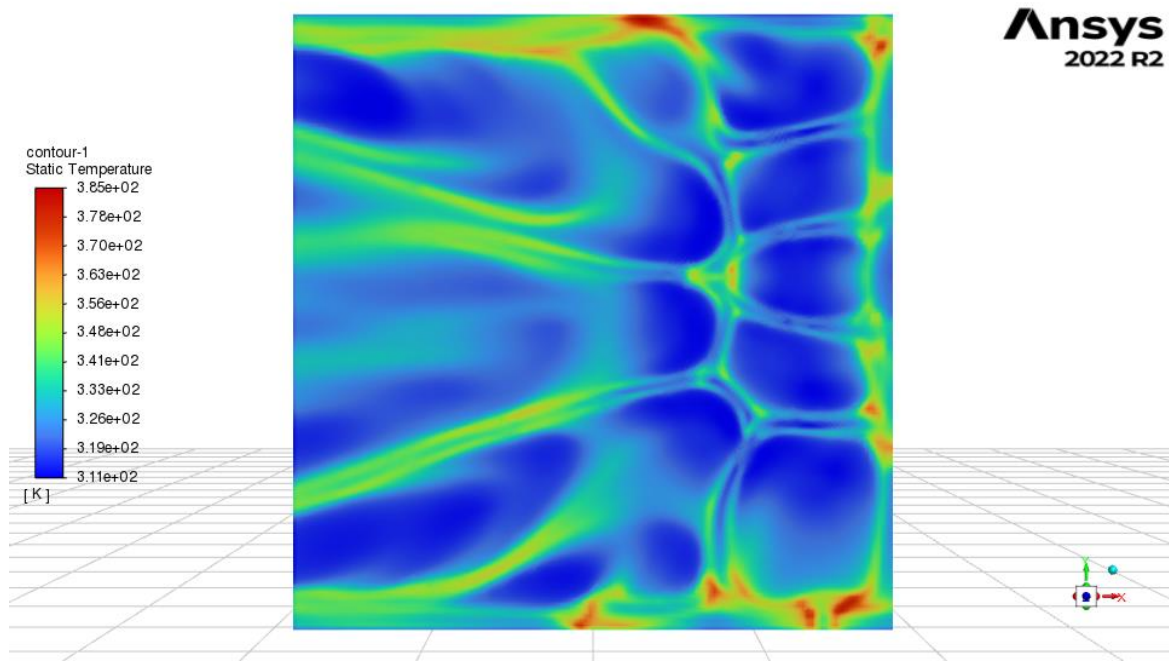


Figure 3.4: Temperature distribution for single exit staggered (exit at left side) grid model ($z/D = 2$) with a mass flow rate of 32 g/s

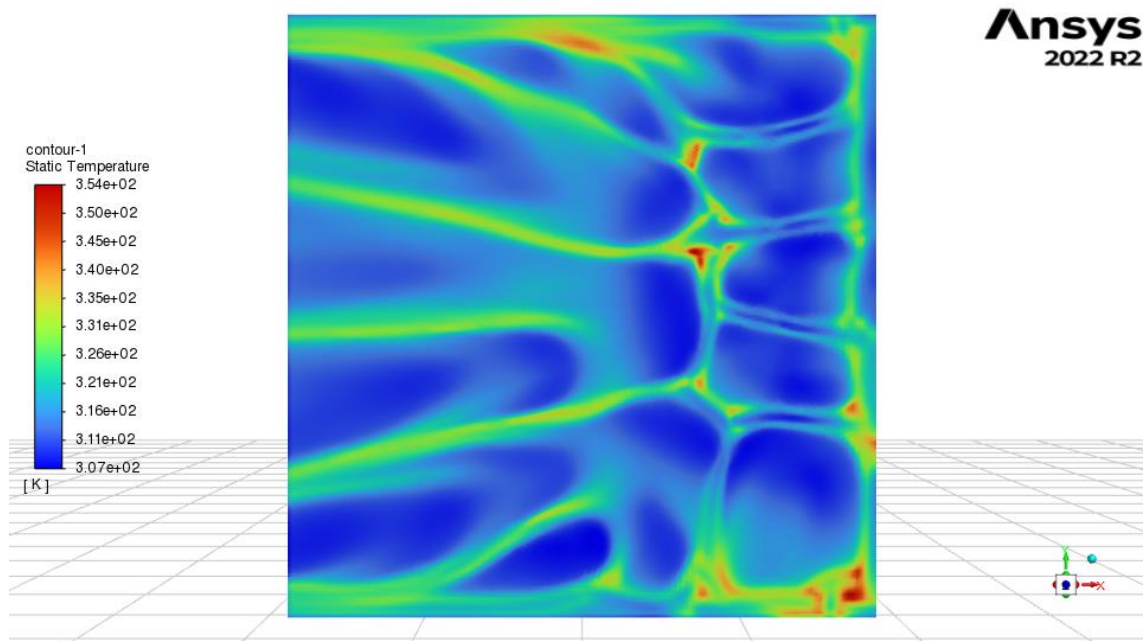


Figure 3.5: Temperature distribution for single exit staggered (exit at left side) grid model ($z/D = 2$) with a mass flow rate of 64 g/s

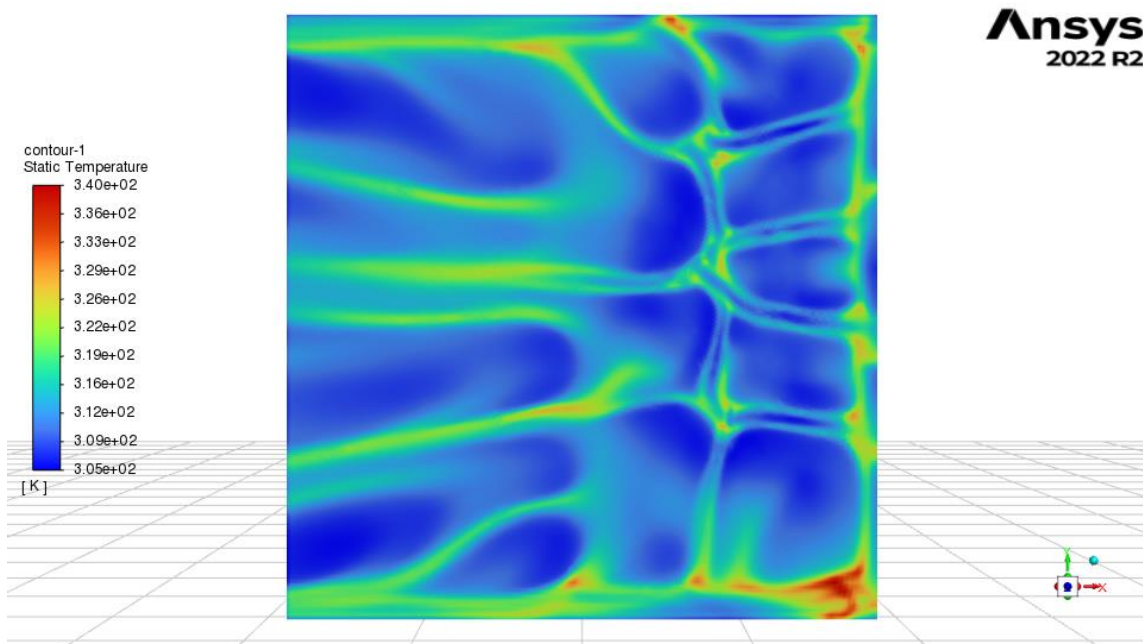


Figure 3.6: Temperature distribution for single exit staggered (exit at left side) grid model ($z/D = 2$) with a mass flow rate of 96 g/s

Checking the different staggered grid configurations shown in figures 3.4, 3.5 and 3.6 for the same z/D value, we can see that the inline configurations show a better temperature drop for the same mass flow rate compared to the staggered grid configurations. However, the staggered grid also shows similar sensitivity to mass flow rate changes similar to the inline grid configuration with temperature drops higher for higher mass flow rates.

Comparing the z/D ratios, the temperature drop increases with increase in z/D value. Comparing the figures 3.7 and 3.8 with 3.1, it is observed that the z/D of 4 gives a maximum temperature drop compared to $z/D = 2$.

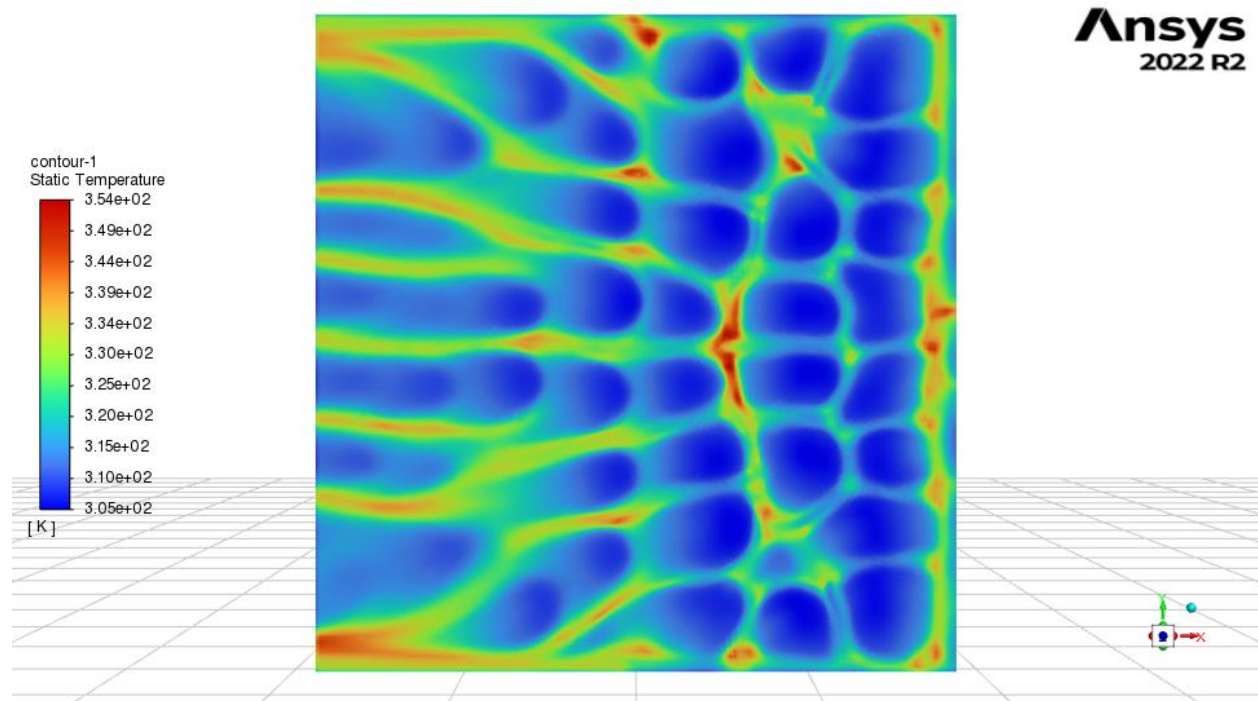


Figure 3.7: Temperature distribution for single exit inline (exit at left side) grid model ($z/D = 4$) with a mass flow rate of 32 g/s

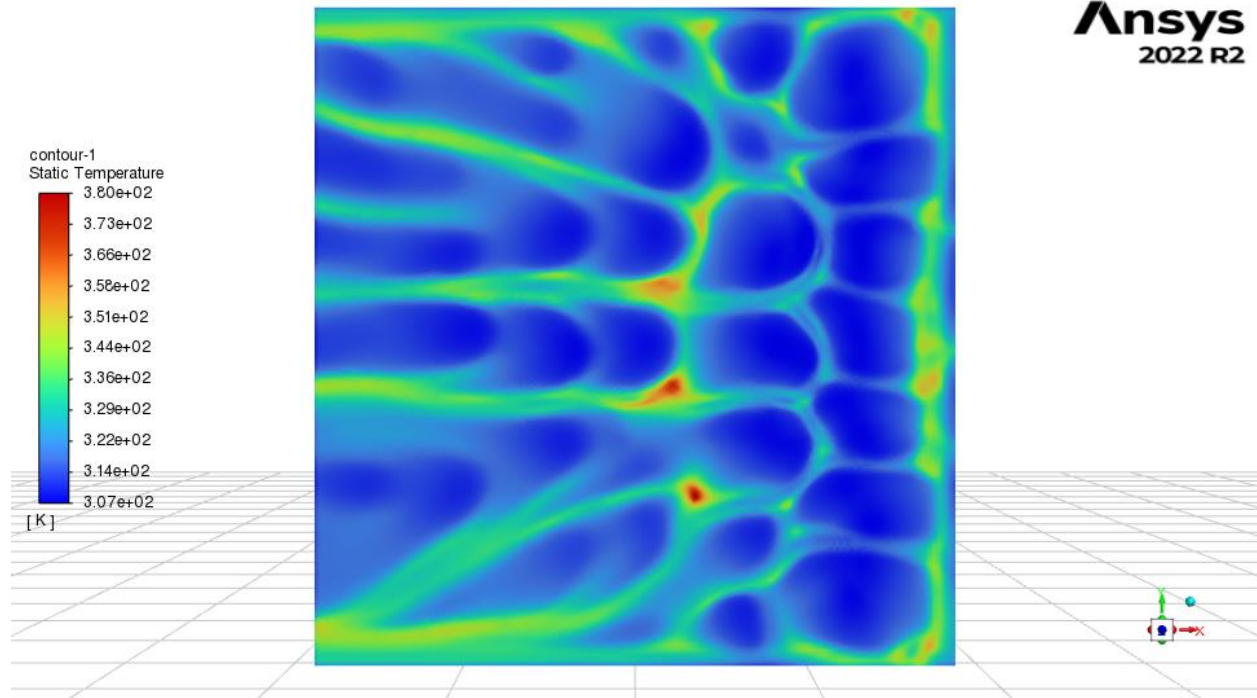


Figure 3.8: Temperature distribution for single exit inline (exit at left side) grid model ($z/D = 3$) with a mass flow rate of 32 g/s

Comparing the contours for the different cases, it can be noted that the jet behavior is similar for all the 3 cases. Since the jet diameter is least for $z/D = 4$, more jets are clearly defined in the temperature contours, when compared to the $z/D = 2$ and $z/D = 3$ cases. The least temperature for $z/D = 2$ and 3 are observed to be 307 K whereas the least temperature noted for $z/D = 4$ is 305 K.

3.1.2 Bidirectional Exit Model Temperature Distribution

Compared to the single exit models, the bidirectional exit configurations provide more interesting contours because of the varying exit mass flow rate ratios, 1:1, 1:2 and 1:3.

The 1:1 models show that the jets contours are more clearly defined in the center of the test section compared to the edges through which the mass flow is exiting equally.

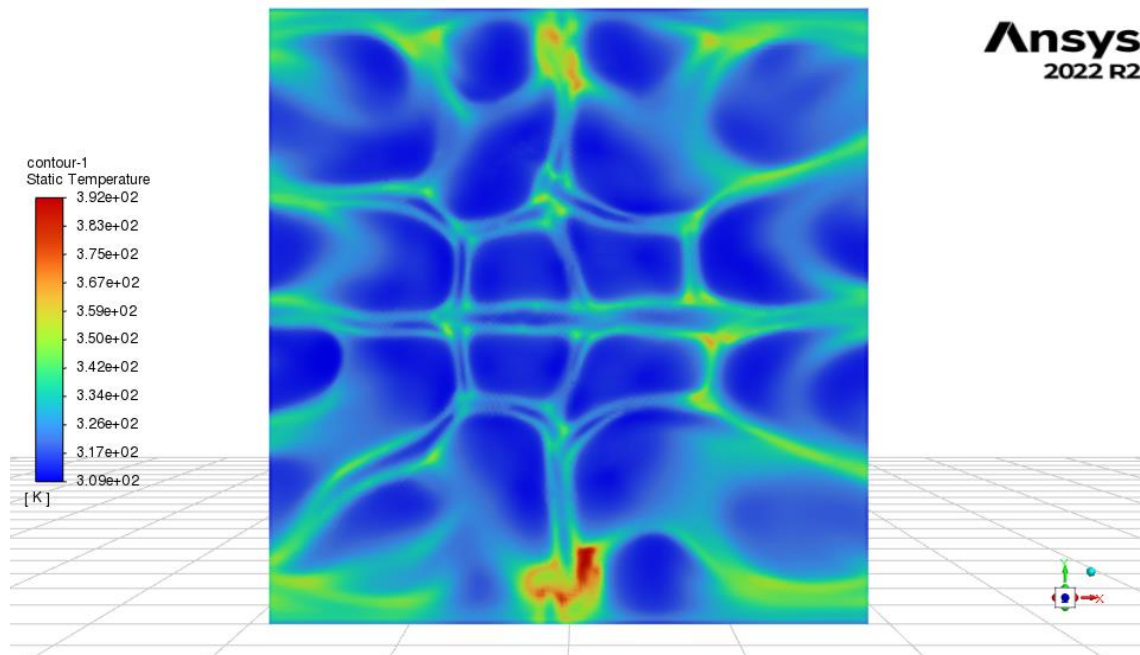


Figure 3.9: Temperature distribution for bidirectional exit (1:1 exit at left and right) inline grid model ($z/D = 2$) with a mass flow rate of 32 g/s

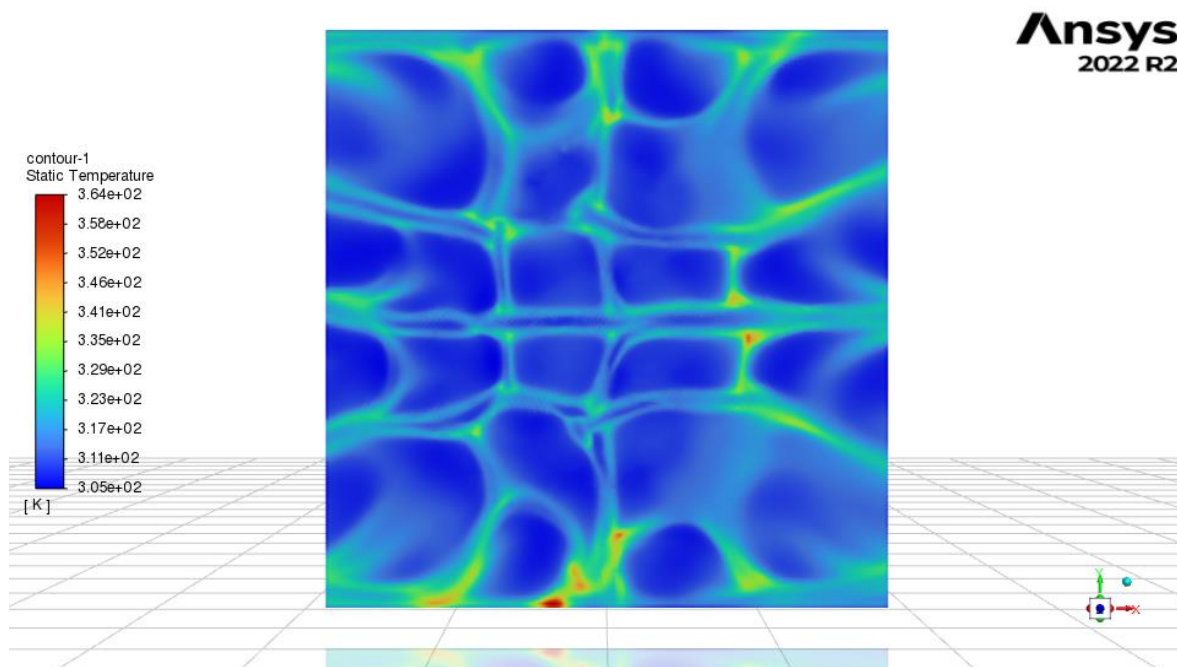


Figure 3.10: Temperature distribution for bidirectional exit (1:1 exit at left and right) inline grid model ($z/D = 2$) with a mass flow rate of 64 g/s

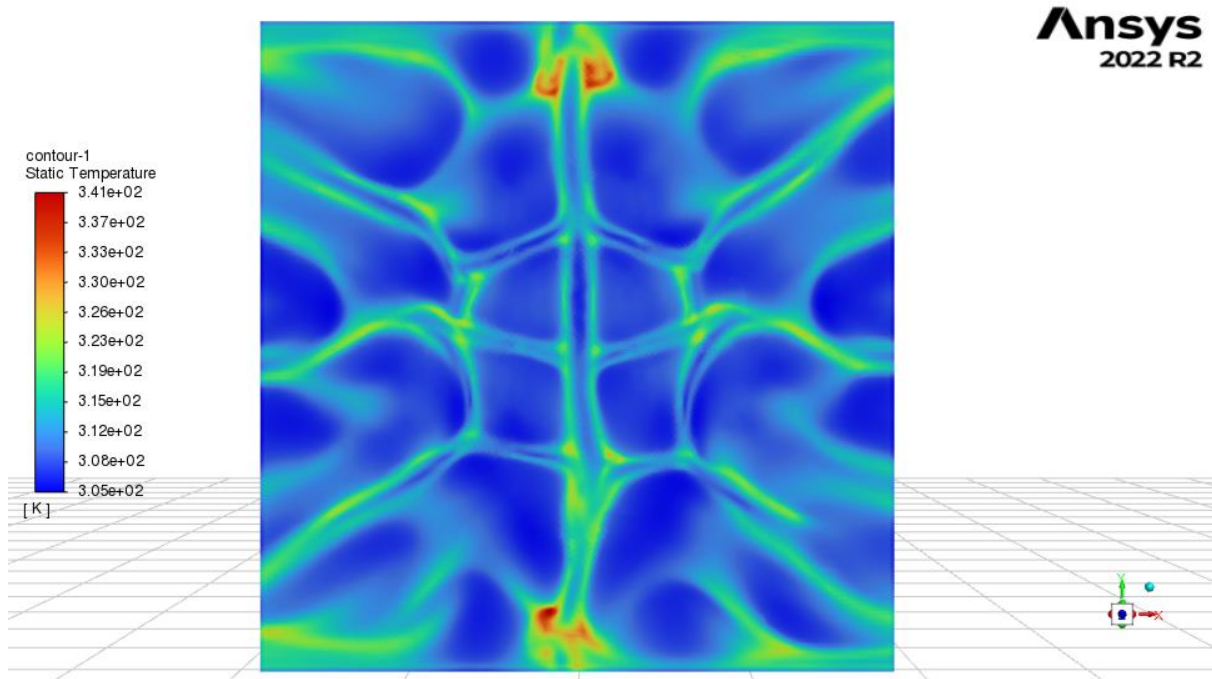


Figure 3.11: Temperature distribution for bidirectional exit (1:1 exit at left and right) inline grid model ($z/D = 2$) with a mass flow rate of 96 g/s

The first configurations analyzed are for $z/D = 2$ or 0.5 inch diameter array jets. Figures 3.9, 3.10 and 3.11 show the various contours for $z/D = 2$ for different mass flow rates. Comparing the contours, all the contours show 4 central fully defined jets whereas the jets at the edges show a more diffusive behavior. Similar to the single exit models, the temperature drop increases with increase in mass flow rates as well.

Checking the second configuration with a 1:2 mass flow exits as shown in figures 3.12, 3.13, and 3.14, it can be seen that the jet contours are more defined in the direction of the exit where the mass flow rate is lesser compared to the other exit where mass flow rate is higher. Due to this, the more defined jets are towards the lesser mass flow rate exit which will have more heat transfer maximas compared to the other exit.

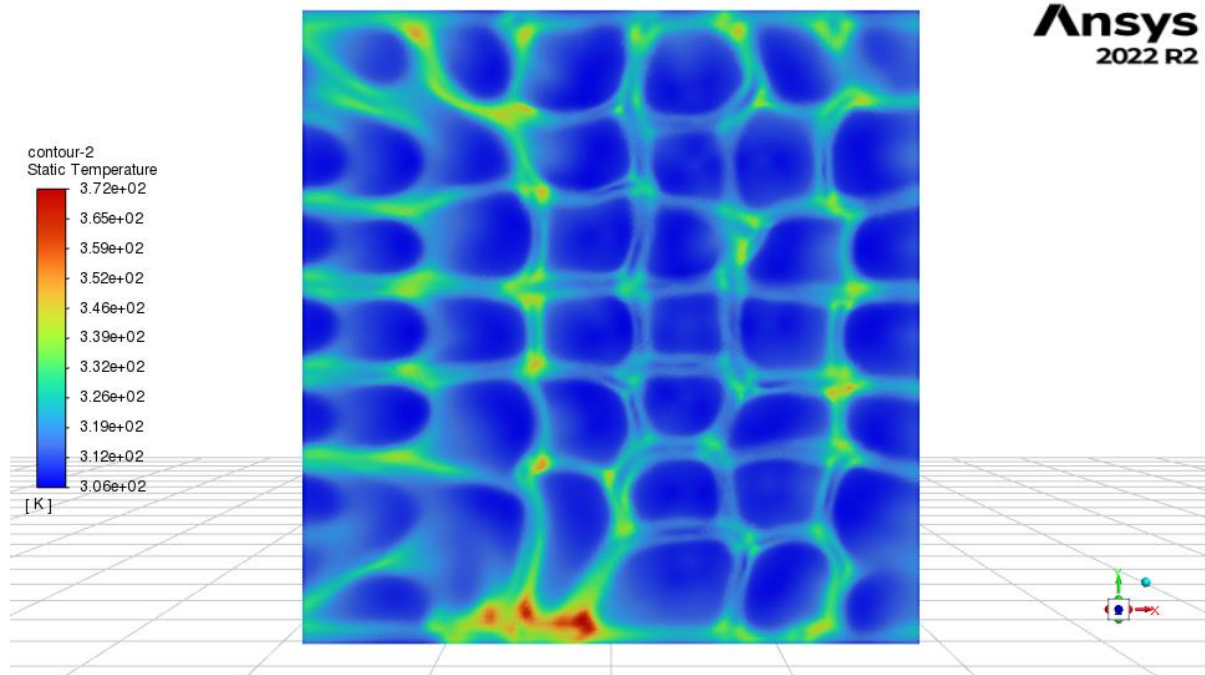


Figure 3.12: Temperature distribution for bidirectional exit (1:2 exit with higher mass flow exit at the left) inline grid model ($z/D = 3$) with a mass flow rate of 32 g/s

Figures 3.12, 3.13 and 3.14 show 1:2 exit contours for $z/D = 3$. It can be observed that the diffusive nature of the jets at the left exit can be observed more clearly as the mass flow rate increases. For this case, the array consists of 7 columns of jets of which 3 of the columns are clearly defined. 3 columns are diffusing towards the left exit and one column is diffusing towards the right exit which is the lower mass flow rate exit.

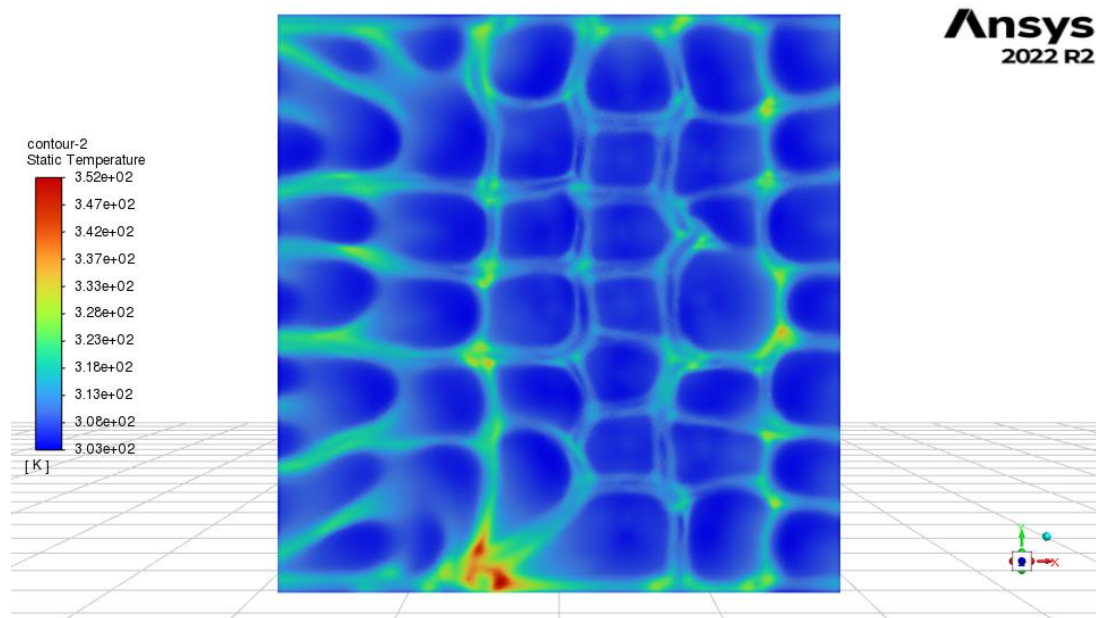


Figure 3.13: Temperature distribution for bidirectional exit (1:2 exit with higher mass flow exit at the left) inline grid model ($z/D = 3$) with a mass flow rate of 64 g/s

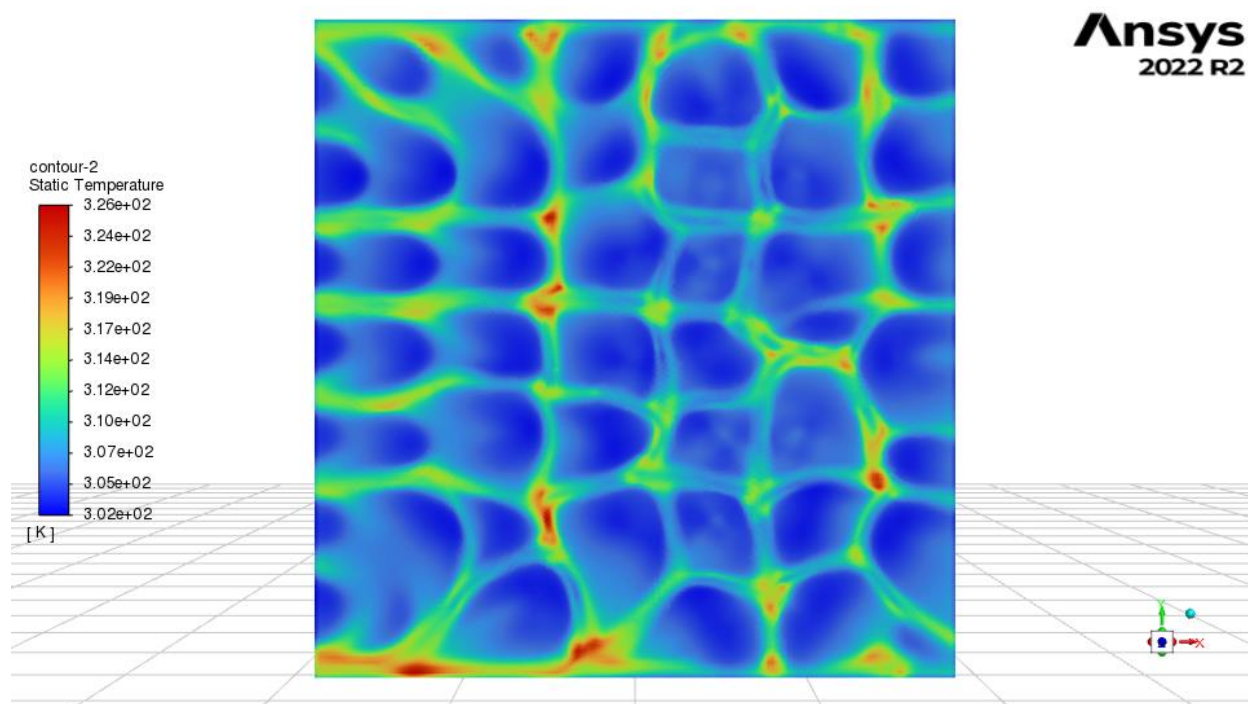


Figure 3.14: Temperature distribution for bidirectional exit (1:2 exit with higher mass flow exit at the left) inline grid model ($z/D = 3$) with a mass flow rate of 96 g/s

The third configuration has a mass flow exit ratio of 1:3. Continuing from the previous case, it is easy to predict that there would be more diffusive behavior towards the left exit since the mass flow rate at the left exit is increased from 66.667 % to 75 % of the total mass flow rate.

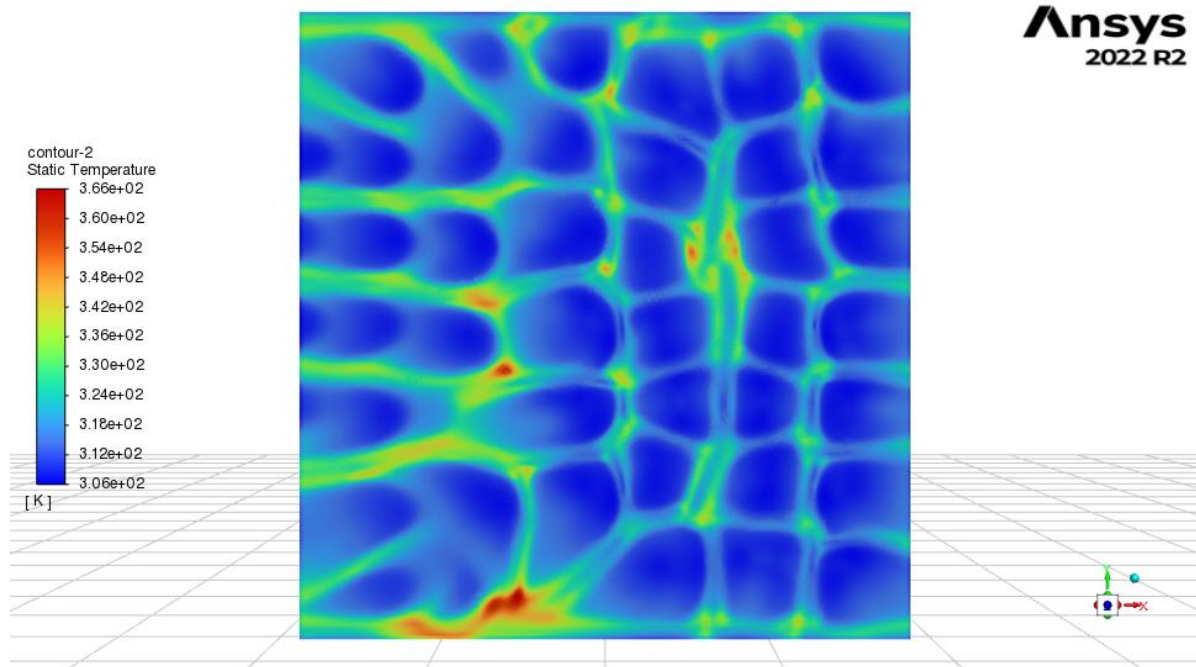


Figure 3.15: Temperature distribution for bidirectional exit (1:3 exit with higher mass flow exit at the left) inline grid model ($z/D = 3$) with a mass flow rate of 32 g/s

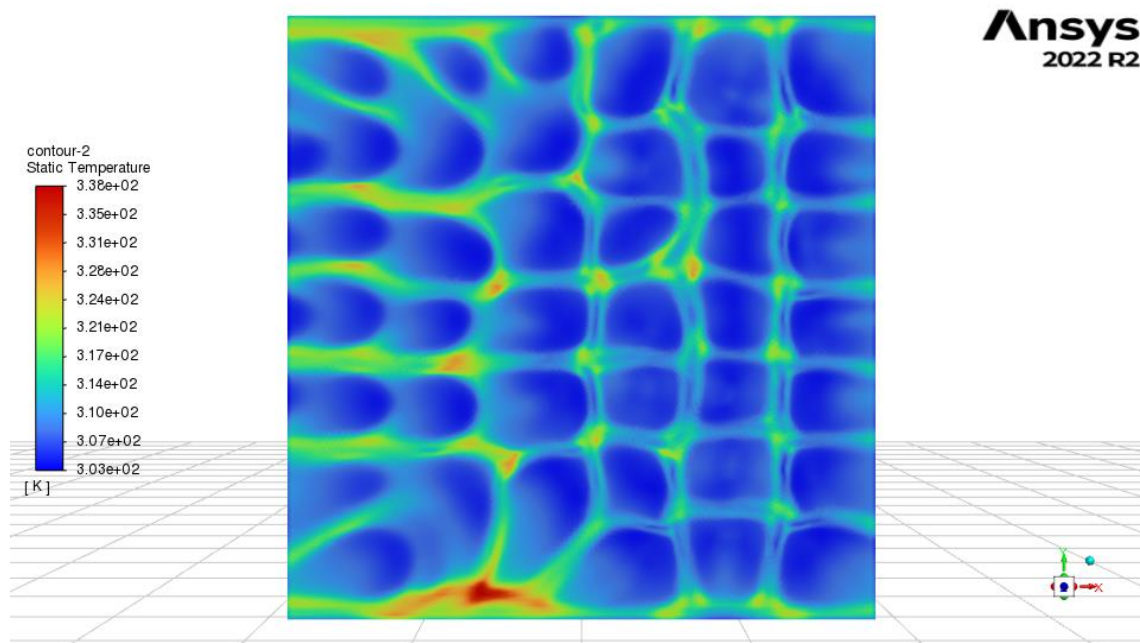


Figure 3.16: Temperature distribution for bidirectional exit (1:3 exit with higher mass flow exit at the left) inline grid model ($z/D = 3$) with a mass flow rate of 64 g/s

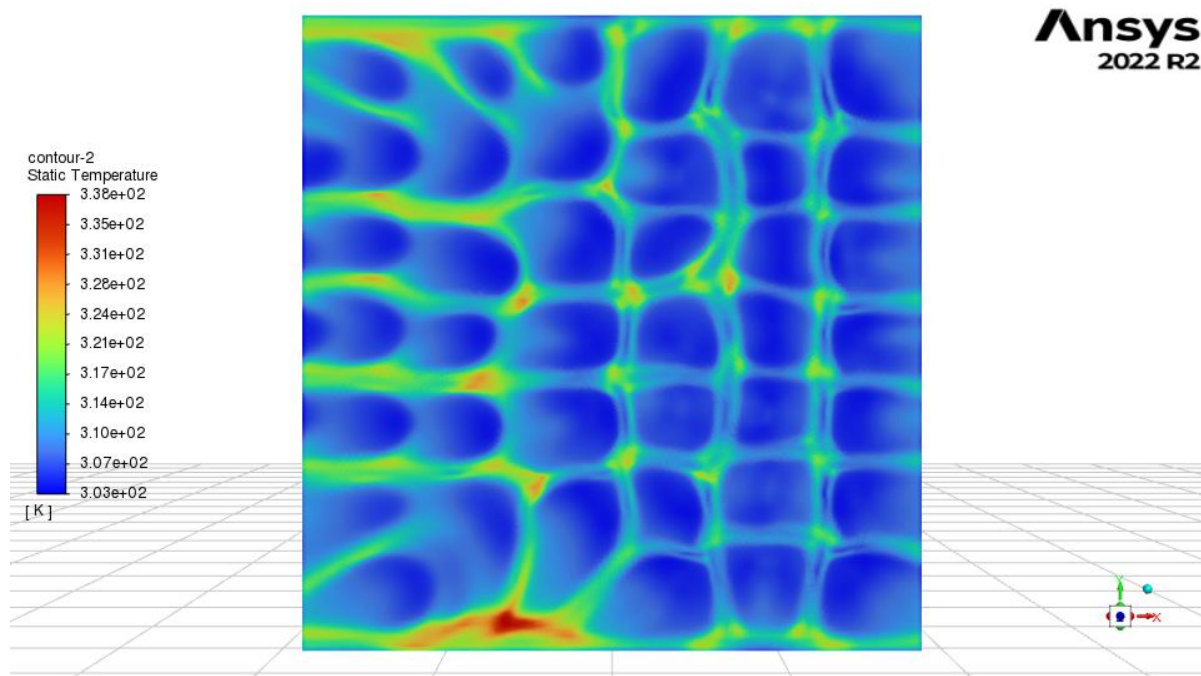


Figure 3.17: Temperature distribution for bidirectional exit (1:3 exit with higher mass flow exit at the left) inline grid model ($z/D = 3$) with a mass flow rate of 96 g/s

Comparing the contours for $z/D = 3$ shown in Figures 3.16, 3.17 and 3.18 with the 1:2 models shown in the Figures 3.13, 3.14 and 3.15, the clearly defined jets reduce from 3 to 2 columns for the 1:3 exit model. Similar to the previous 1:2 models, the diffusivity can be observed on the initial 4 columns on the left and the last column near the right exit.

The next comparison of the models can be based on whether the model has an inline grid or a staggered grid. The staggered grid configurations are not symmetric similar to the inline configuration and the shape of the jets are observed to a lesser extent compared to the inline configurations.

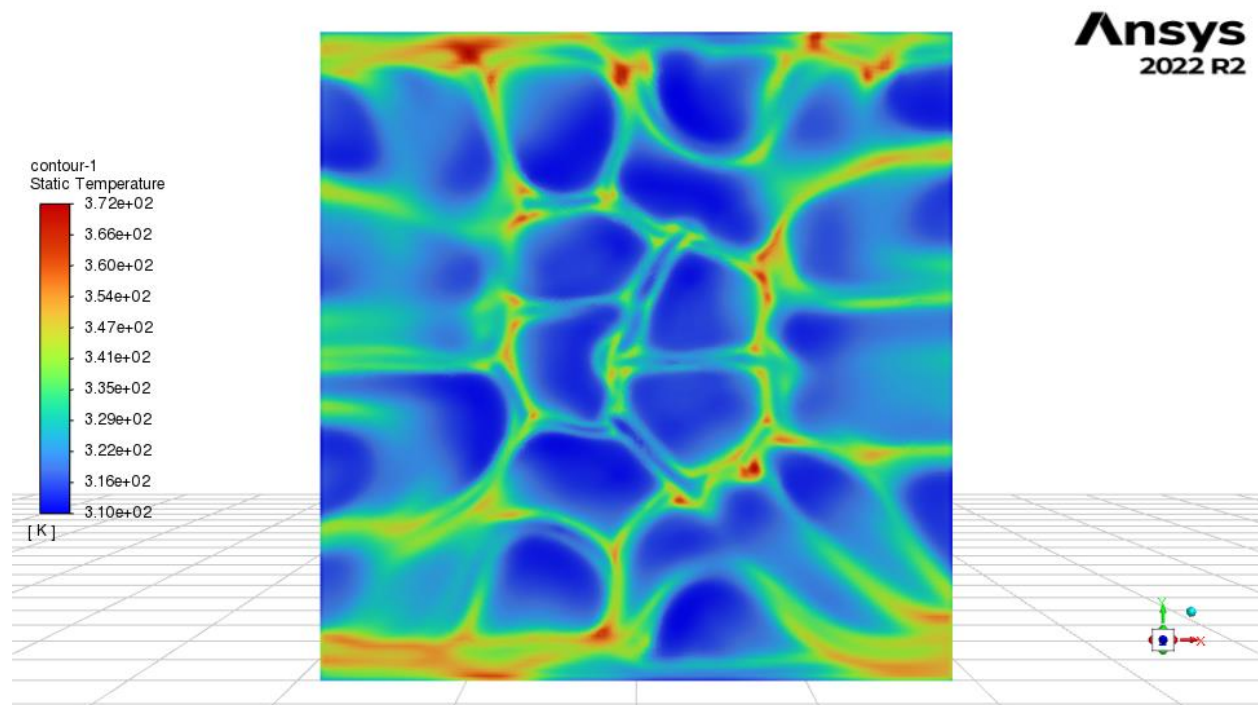


Figure 3.18: Temperature distribution for bidirectional exit (1:1 exit at left and right) staggered grid model ($z/D = 2$) with a mass flow rate of 32 g/s

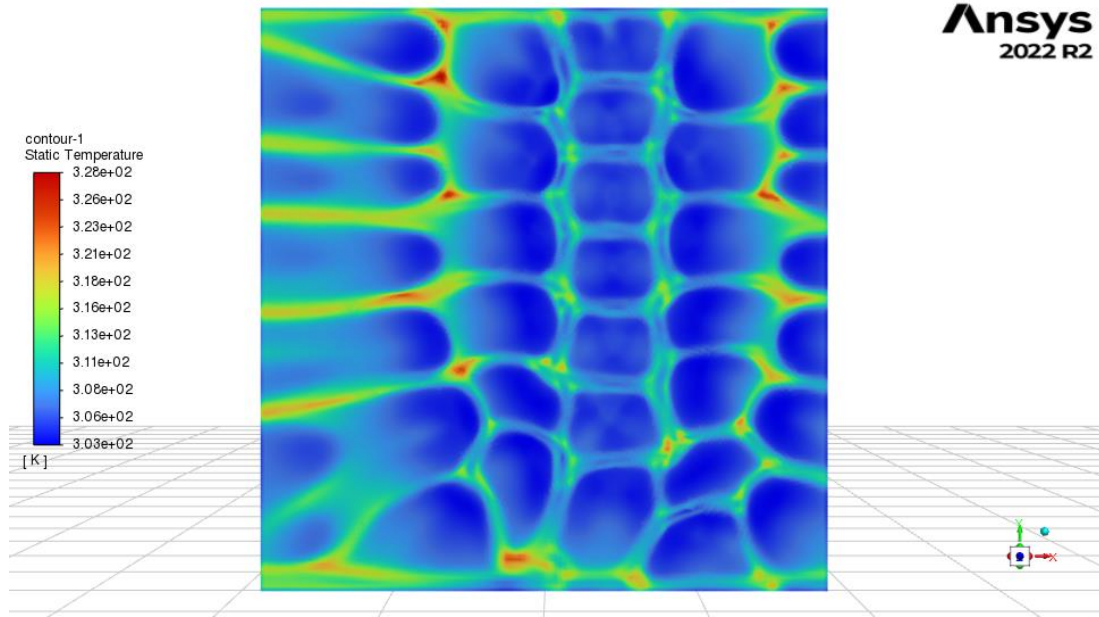


Figure 3.19: Temperature distribution for bidirectional exit (1:2 exit with higher mass flow exit at the left) staggered grid model ($z/D = 3$) with a mass flow rate of 96 g/s

Comparing the inline and staggered models from Figure 3.9 and 3.19 for the 1:1 models, The temperature drop is seen to be higher for the inline grid similar to the single exit model and the jets are more defined for inline grid due to its symmetrical nature.

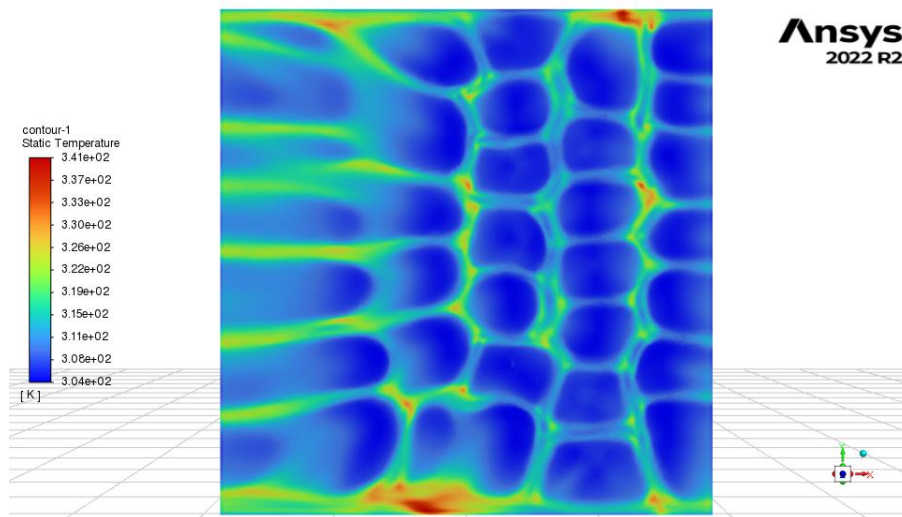


Figure 3.20: Temperature distribution for bidirectional exit (1:3 exit with higher mass flow exit at the left) staggered grid model ($z/D = 3$) with a mass flow rate of 64 g/s

Figures 3.20 and 3.15 show a similar comparison for the 1:2 models. Both show similar contours except for the alignment of jets in the staggered and inline grid configuration. As observed in the previous cases, the inline grid promotes a higher temperature drop compared to the staggered grid. Similar observations can be made for Figure 3.21, which shows the staggered grid 1:3 model when compared to the same model's inline grid configuration shown in Figure 3.17.

The last comparison of the contours can be made based on the different z/D ratios. As observed in the single exit model, the smaller jet diameter configurations with higher z/D ratios present much clearer jet contours compared to lower z/D ratios as shown in the figures in this section.

3.2 Nusselt Number based on Area-Averaged Temperature

Nusselt numbers calculated based on the area-averaged temperature for the inline and staggered plates are plotted against different Reynolds numbers for the single exit configuration and the various bidirectional exit configurations, namely, 1:1, 1:2, and 1:3 is shown in this section.

3.2.1 Single Exit Configuration

The single exit configuration for the inline and staggered grids explains how the inline grid performs better than the staggered grid, with a considerable higher Nusselt Number compared to the staggered grids.

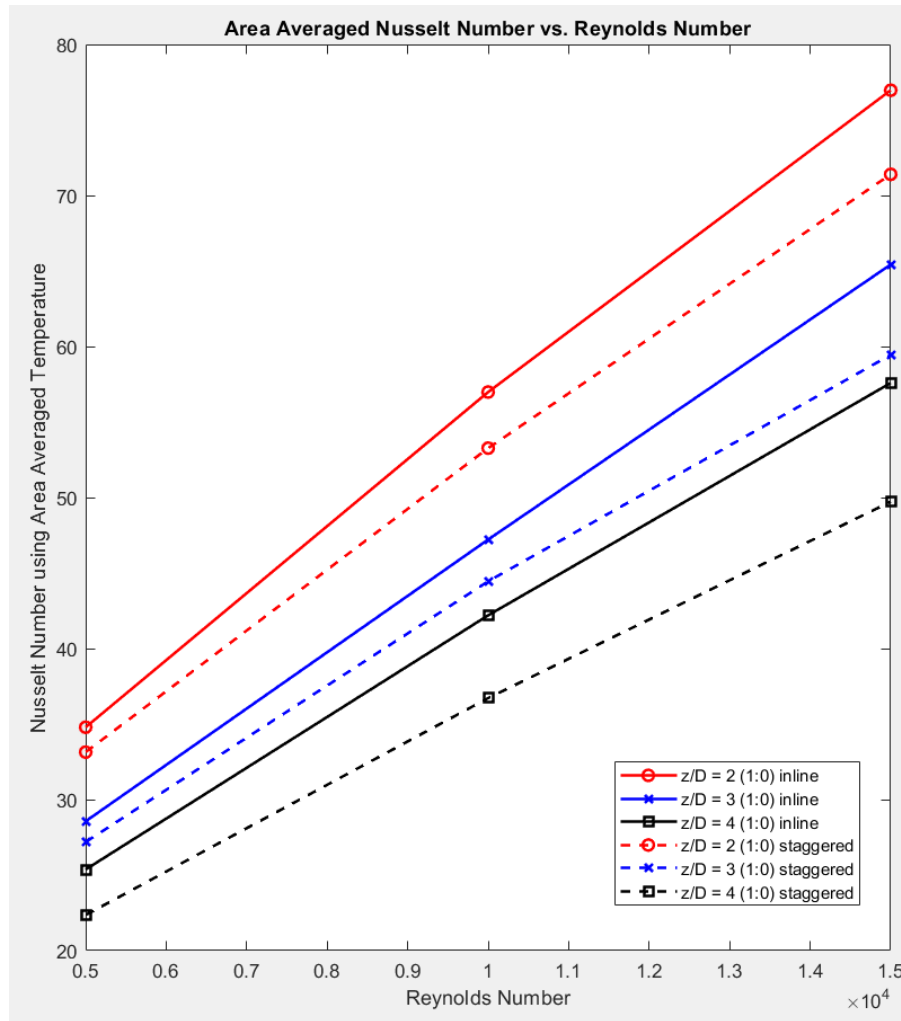


Figure 3.21: Nusselt Number (using Area Averaged Temperature) vs. Reynolds Number for a single exit jet impingement configuration

As per the plot, it can be observed that the Nusselt Number increases as the z/D ratio is higher. Therefore, the 0.5 inch diameter jets provided the highest Nusselt Number compared to the 0.33 inch diameter and 0.25 inch diameter jets. Further, for all the 3 cases provided in the plot, the inline configuration provides better heat transfer for the 3 Reynolds Numbers (5000, 10000 and 15000).

3.2.2 Bidirectional Exit Configurations

The bidirectional exit configurations do not show a huge difference between 1:1, 1:2 and 1:3 configurations for z/D ratios. However, as z/D ratios decrease, the area averaged Nusselt number increases. Comparing the values to the single exit model, the plots for the inline and staggered bidirectional exit models shown in figures 3.22 and 3.23 show a higher Nusselt number value for each Reynolds number.

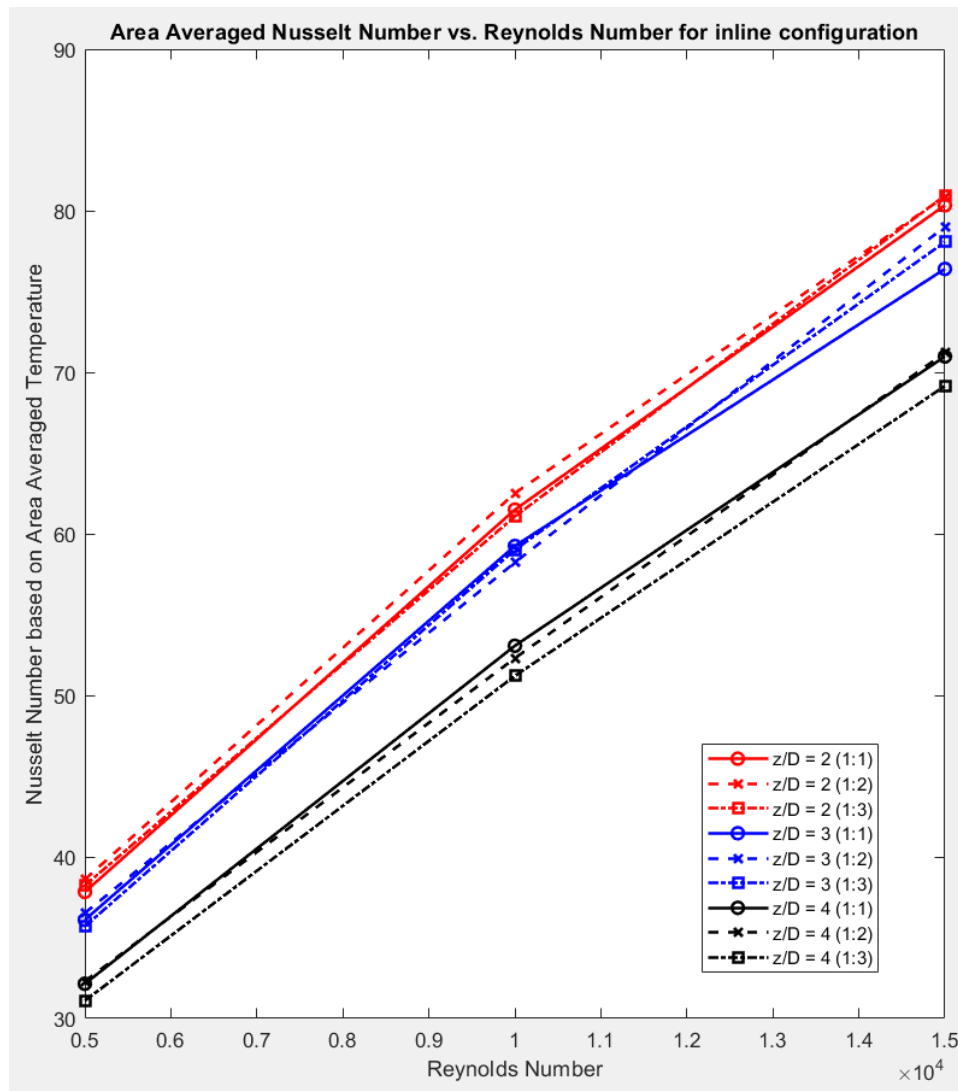


Figure 3.22: Nusselt Number (using Area Averaged Temperature) vs. Reynolds Number for a bidirectional exit inline jet impingement configuration

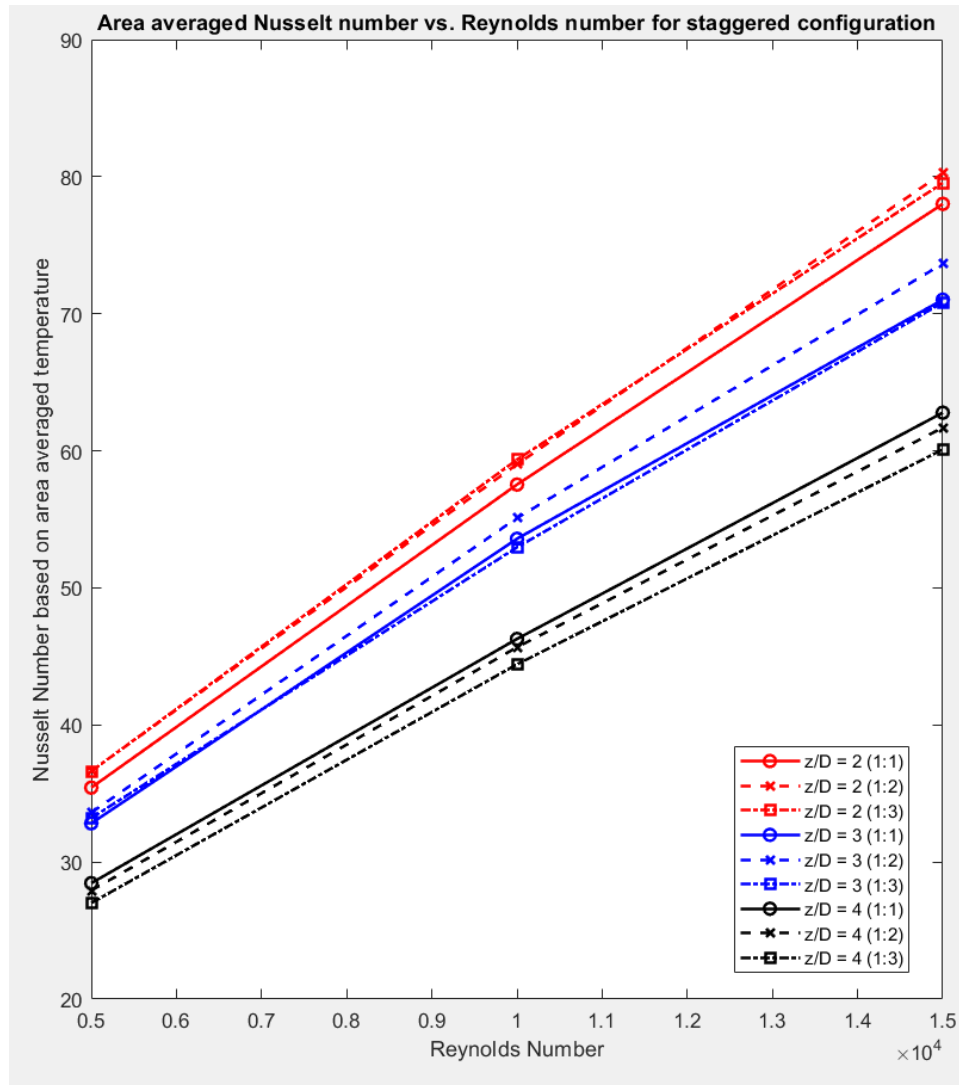


Figure 3.23: Nusselt Number (using Area Averaged Temperature) vs. Reynolds Number for a bidirectional exit staggered jet impingement configuration

Analyzing the inline and staggered grid configurations further, it can be noted that the Nusselt number values are lesser for the staggered grid configuration compared to the inline grid models. These further cement the initial results obtained from the temperature contours obtained for the different models. The higher temperature drop models were inline models which is validated with a higher area averaged Nusselt number when compared to the staggered grid models.

3.3 Spanwise Nusselt Number

Nusselt number is also calculated considering a region of interest where the hole contours are uniformly distributed along the X-direction and the overall average Nusselt number is calculated such that the variation of the Nusselt number along the length of the test section can be noted. Since the walls other than the test section are considered to be adiabatic, it was observed that the edges of the walls which are in contact with the adiabatic walls have a higher Nusselt number. To avoid any discrepancies due to this, the plate has been considered to be 4.5 inches long and 0.25 inches is excluded from either side to get more accurate results.

3.3.1 Single Exit Configuration

For single exit configurations, it can be observed that the Nusselt number peaks at opposite edge of the test section from the exit. The Nusselt number maximas and minimas start reducing when moving towards the exit. For higher z/D ratios, a higher Nusselt number can be observed near the exits whereas it reduces as the z/D ratio is increased. Further, staggered configurations show a sharp decrease in spanwise Nusselt number values when moving from $x/D = 1$ to 0. This further shows why the inline configuration provides better heat transfer compared to the staggered grid configurations.

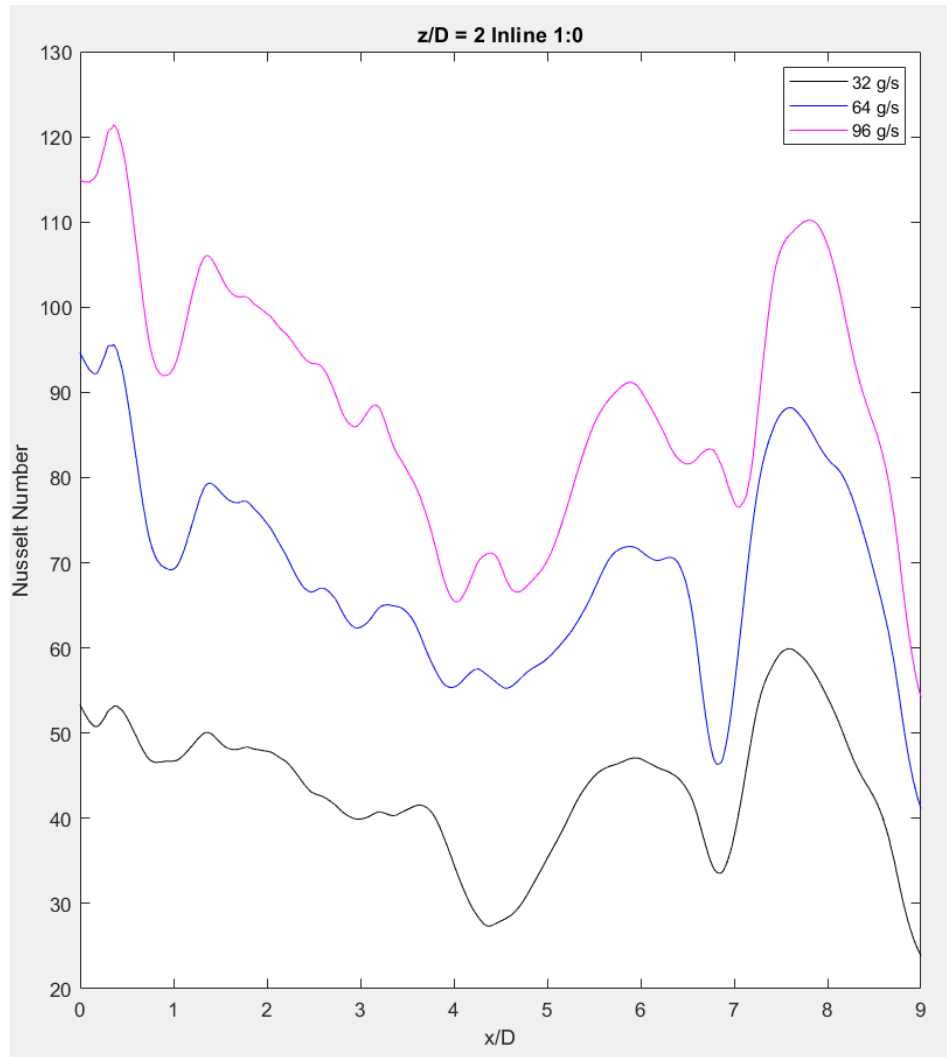


Figure 3.24: Spanwise Nusselt Number for inline grid configuration for $z/D = 2$

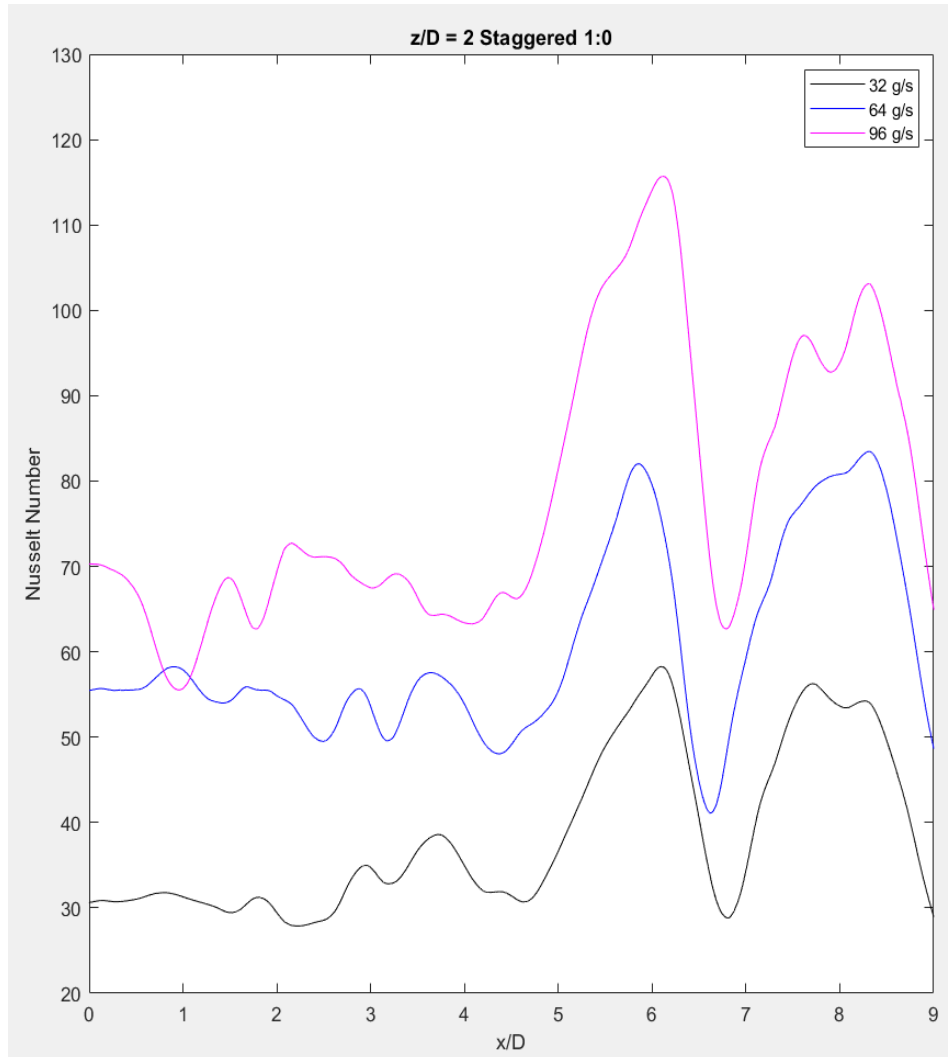


Figure 3.25: Spanwise Nusselt Number for staggered grid configuration for $z/D = 2$

For $z/D = 2$ configurations, the Nusselt number variation can be noticed when moving from $x/D = 1$ to 0. As shown in figures 3.24 and 3.25, the maxima of the staggered grid configuration is higher than the maxima of the inline grid. However, the average Nusselt number when approaching the exit is higher for the inline grid compared to the staggered grid.

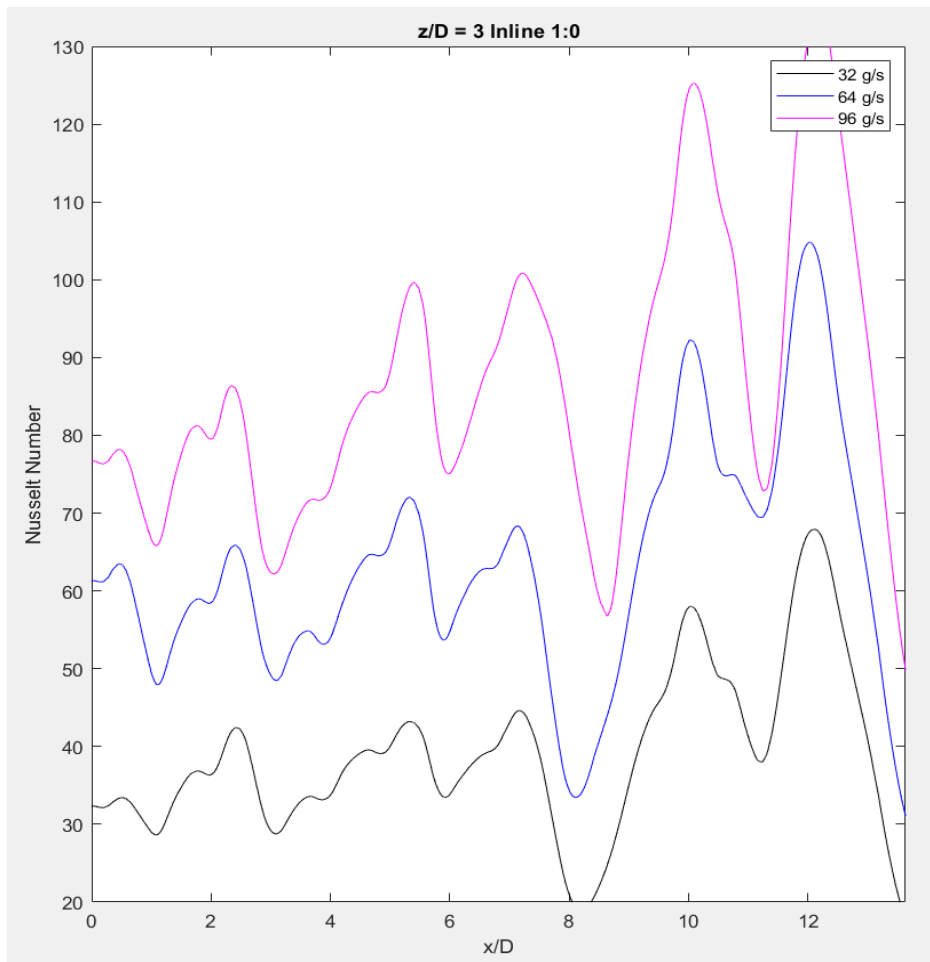


Figure 3.26: Spanwise Nusselt Number for inline grid configuration for $z/D = 3$

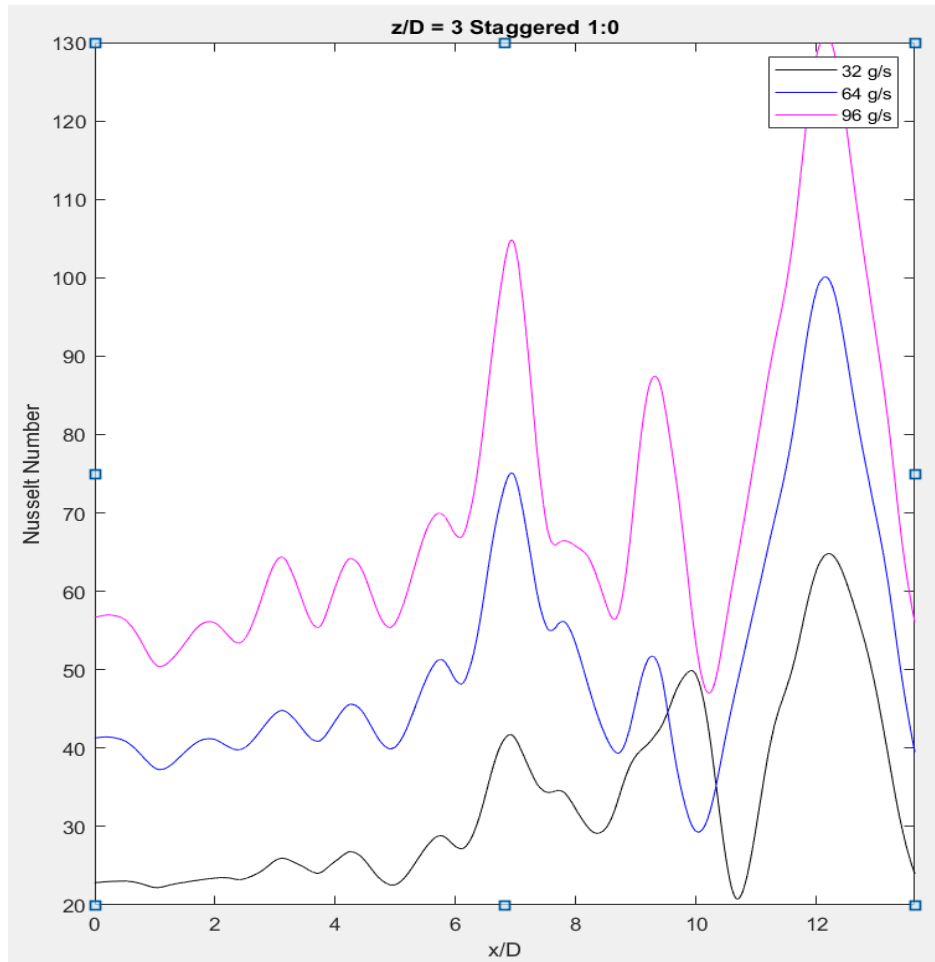


Figure 3.27: Spanwise Nusselt Number for staggered grid configuration for $z/D = 3$

As the z/D is increased to 3, contours are similar to the previous case where local maxima for both inline and staggered configurations appear to be the same. Since all the models are run at steady state, the difference between the local maxima and minima for the single exit and the bidirectional exit models are high but the area averaged Nusselt number are comparable to literature [14] [7].

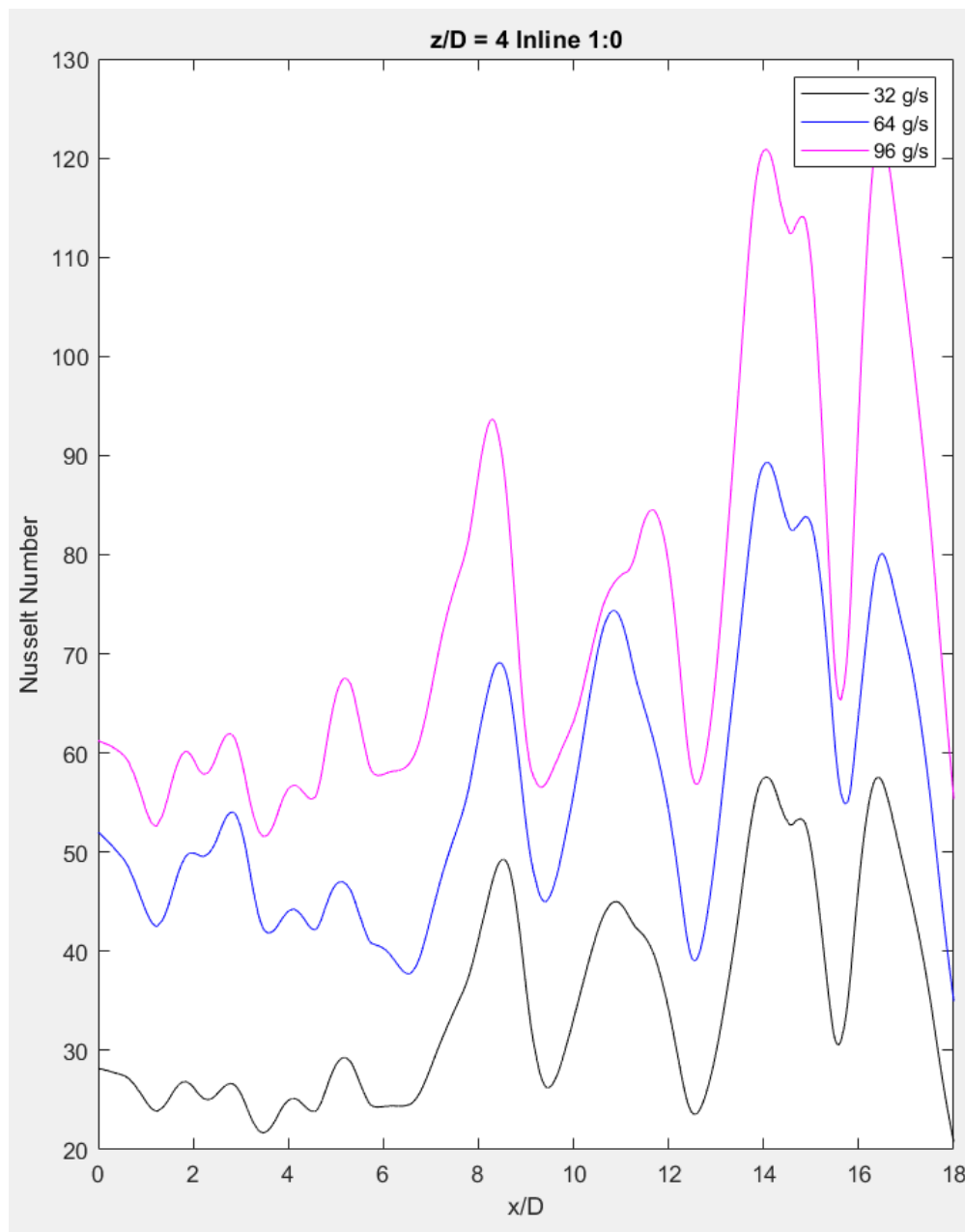


Figure 3.28: Spanwise Nusselt Number for inline grid configuration for $z/D = 4$

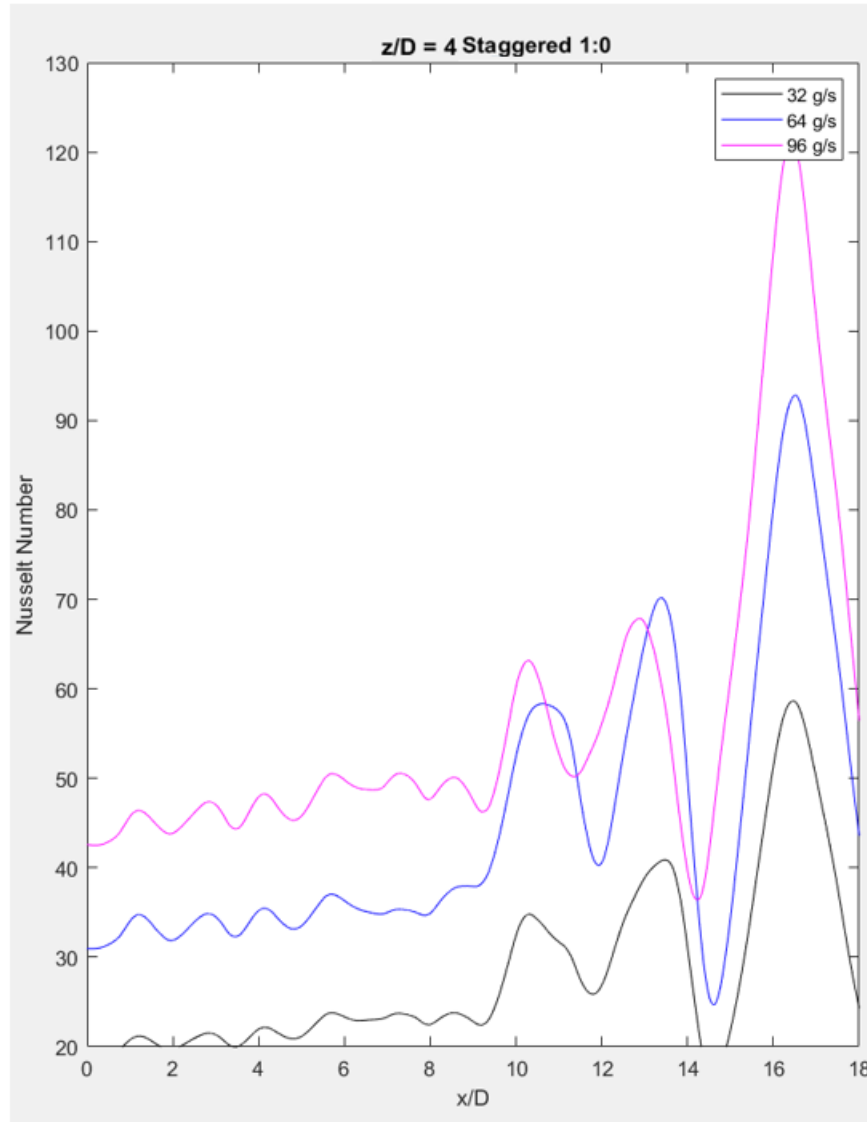


Figure 3.29: Spanwise Nusselt Number for staggered grid configuration for $z/D = 4$

3.3.2 Bidirectional Exit Model

The spanwise Nusselt number plots show local maxima at the points where the orifices align with the test plate and show a local minima in the value of Nusselt number in the spacing between adjacent holes. As the mass flow is biased towards one side, the lower mass flow side shows a higher Nusselt number value with defined jet shaped contours whereas the higher mass flow side does not show the jet contours. As shown in the figures below for $z/D = 2$, the maximas

and minimas are more clearly defined for the 1:1 mass flow exit case compared to the 1:2 and 1:3 flow cases. However, it can be observed that the maxima retain almost the same value compared to the 1:1 case.

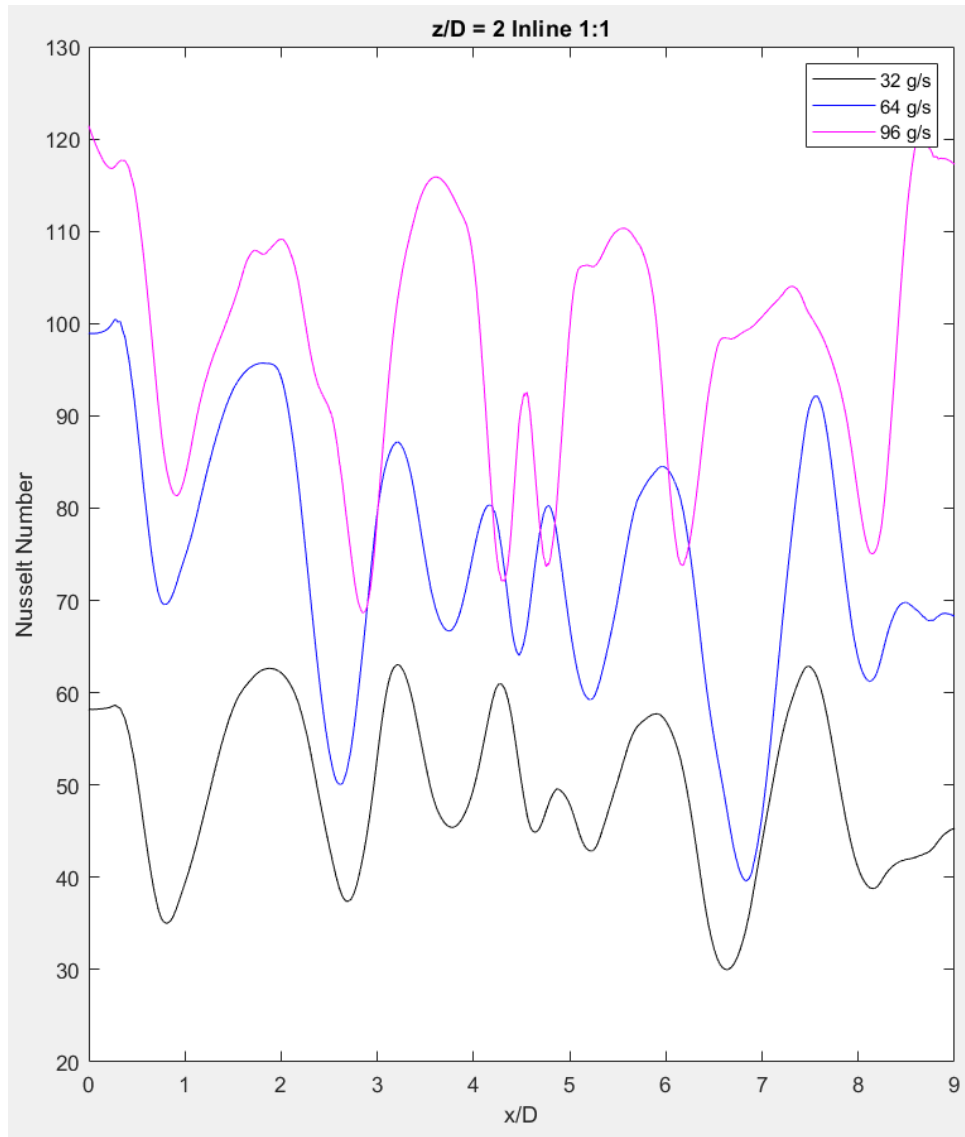


Figure 3.30: Spanwise Nusselt Number distribution for 1:1 mass flow inline configuration

($z/D = 2$)

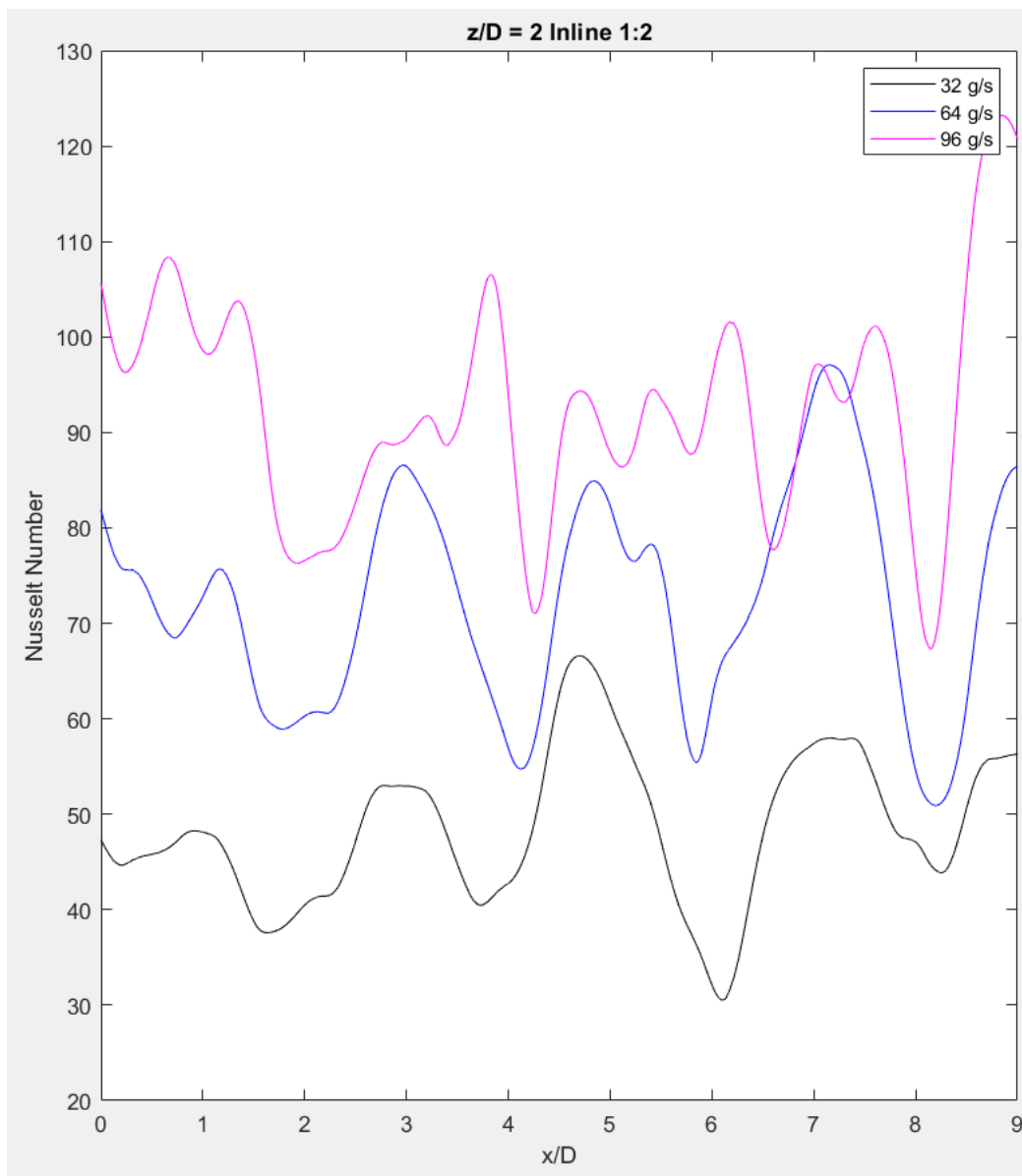


Figure 3.31: Spanwise Nusselt Number distribution for 1:2 mass flow inline configuration

($z/D = 2$)

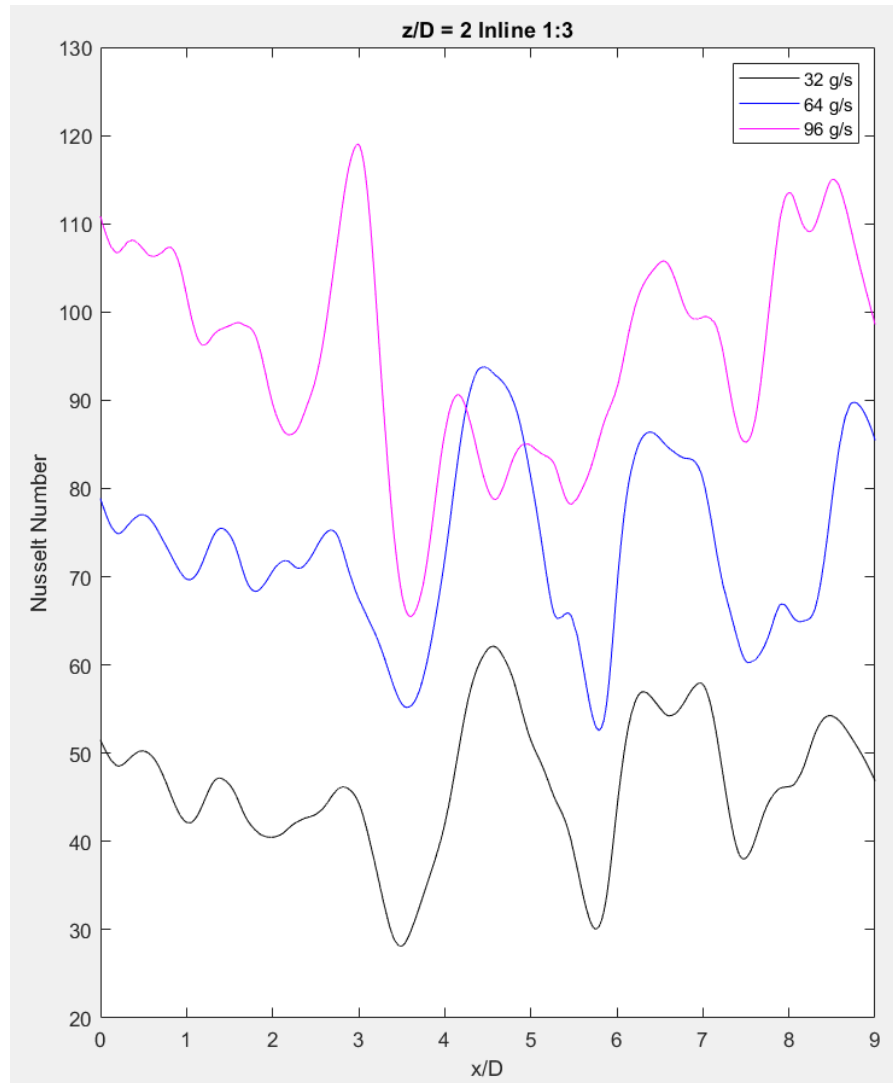


Figure 3.32: Spanwise Nusselt Number distribution for 1:3 mass flow inline configuration
($z/D = 2$)

Compared to the experimental values obtained for similar cases, the major difference that can be observed is that the local maxima and the local minima Nusselt number values are greater and lesser respectively than respective experimentally obtained values. This may be due to the experiment being done for transient case, whereas the simulations are all done at steady state. Multiple peaks can also be observed for the center holes due to the mass flow being diverted

towards the exits. High mass flow cases show a single peak for the center orifices compared to the lower mass flow rates. As the z/D values are increased to 3 and 4, the jet contours are more defined and the spanwise Nusselt number values show a more uniform distribution compared to the above case.

For the inline configuration where $z/D = 4$, the spanwise Nusselt number plots show a more uniform distribution of the jets compared to the $z/D = 2$ configuration as shown in the below figures. Since the z/D ratio is higher, it can be observed that the local maximas and minimas are more clearly visible for this case. As the mass flow is biased towards the left exit, the local maximas and minimas seem to disappearing from the left exit. Similar trends can be seen for z/D ratio of 3 as well.

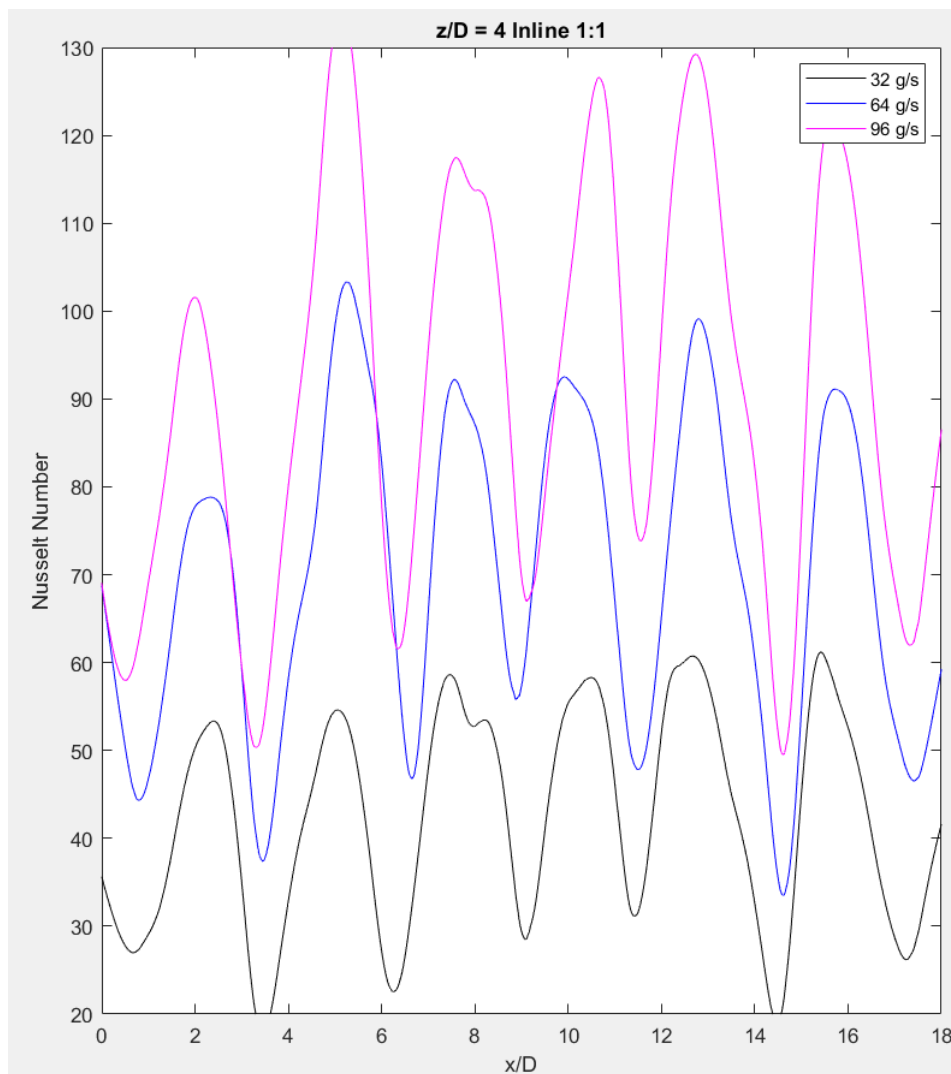


Figure 3.33: Spanwise Nusselt Number distribution for 1:1 mass flow inline configuration

($z/D = 4$)

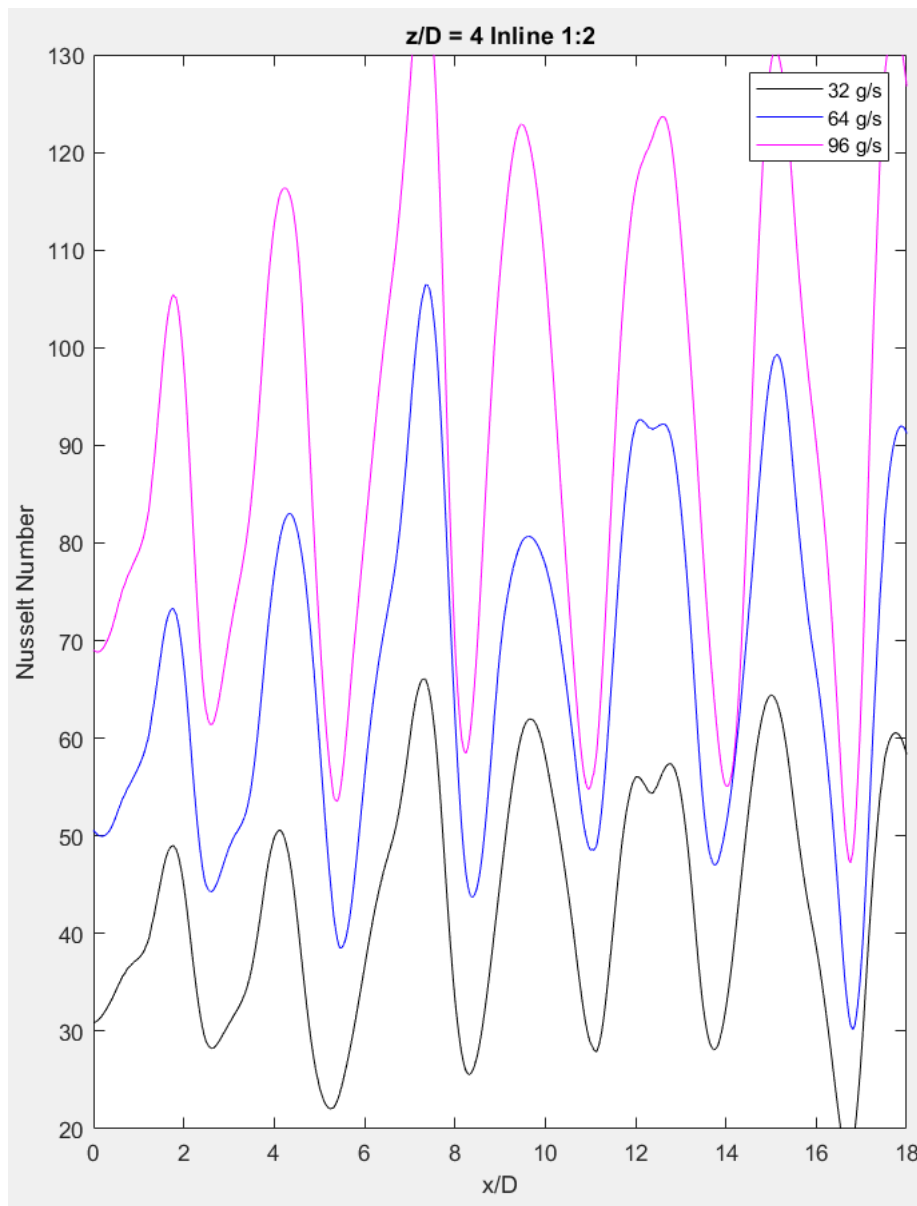


Figure 3.34: Spanwise Nusselt Number distribution for 1:2 mass flow inline configuration
($z/D = 4$)

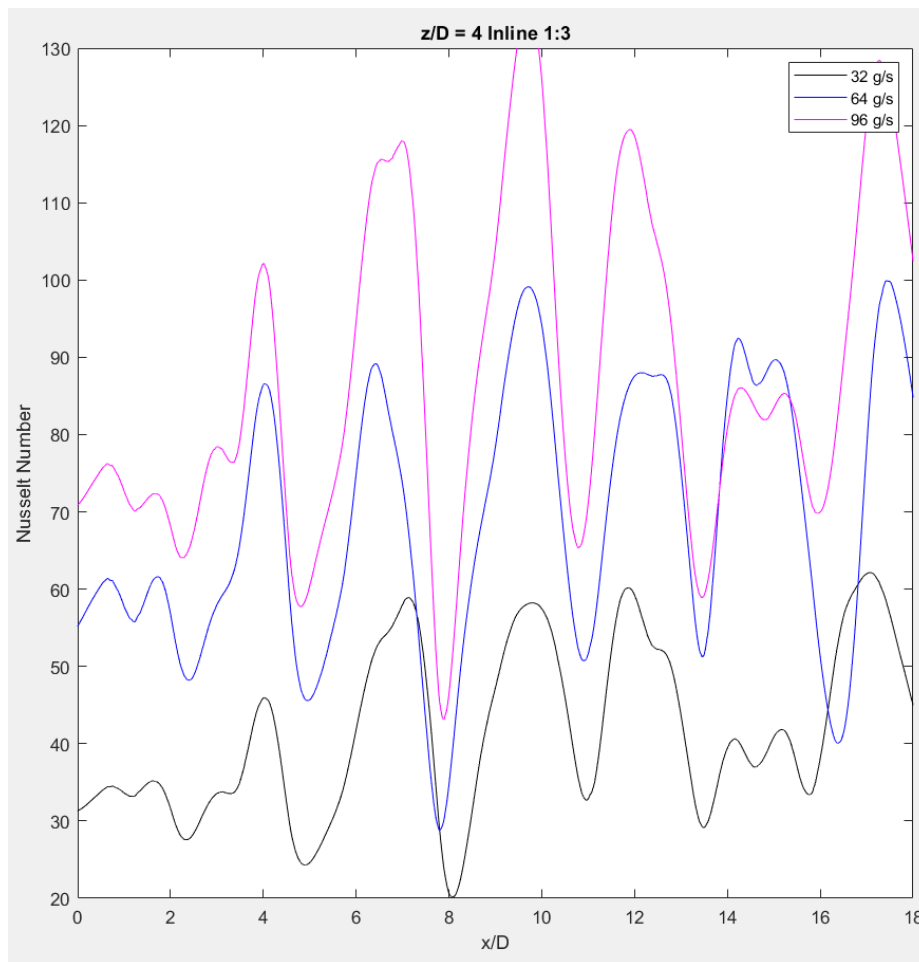


Figure 3.35: Spanwise Nusselt Number distribution for 1:3 mass flow inline configuration

($z/D = 4$)

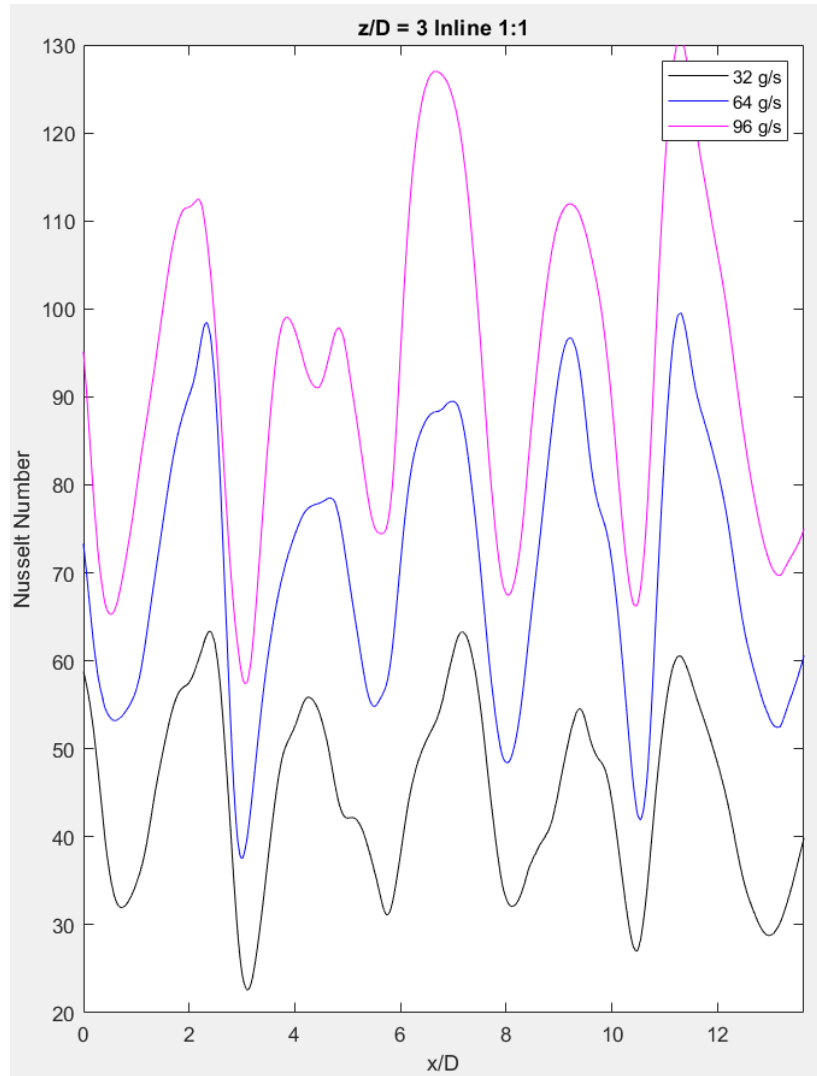


Figure 3.36: Spanwise Nusselt Number distribution for 1:1 mass flow inline configuration

($z/D = 3$)

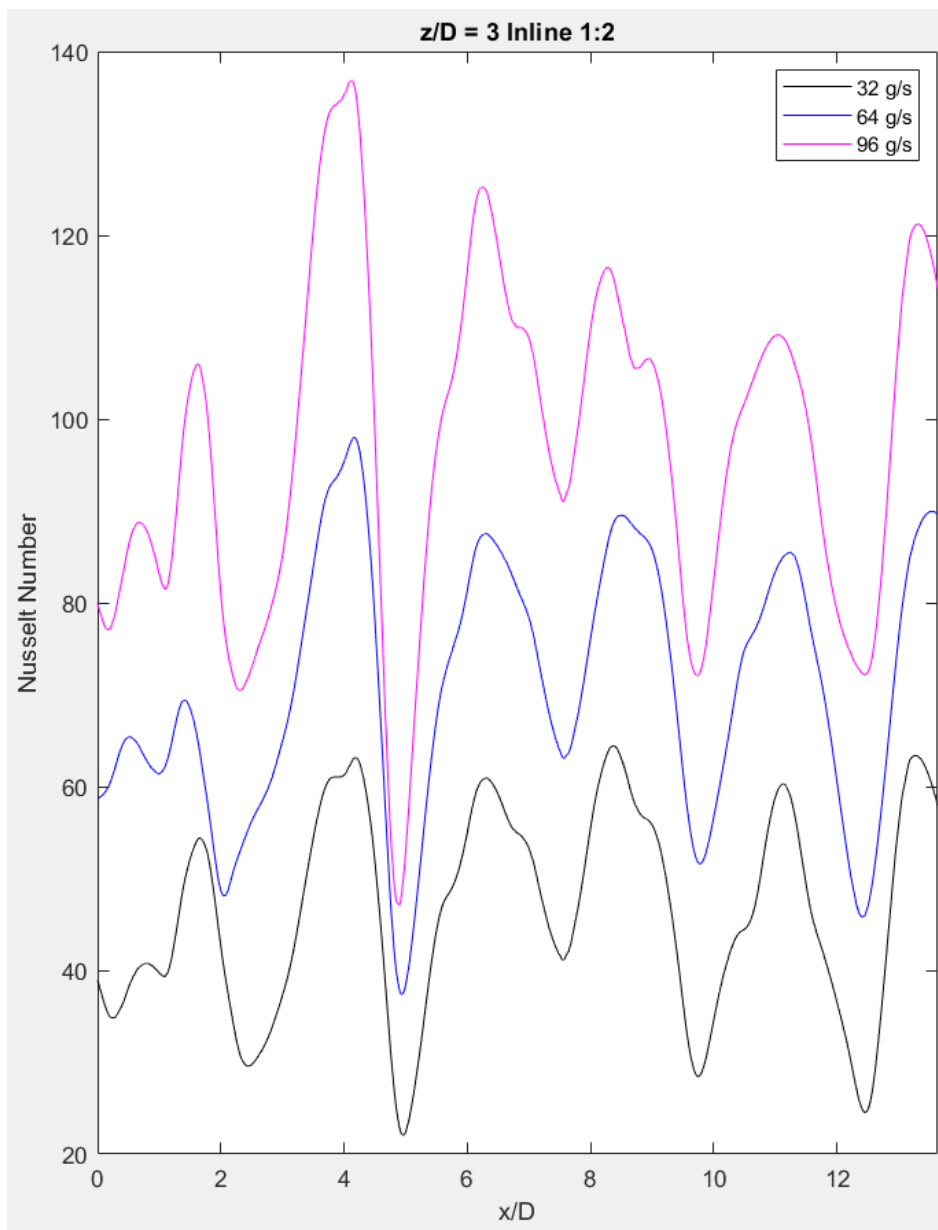


Figure 3.37: Spanwise Nusselt Number distribution for 1:2 mass flow inline configuration

($z/D = 3$)

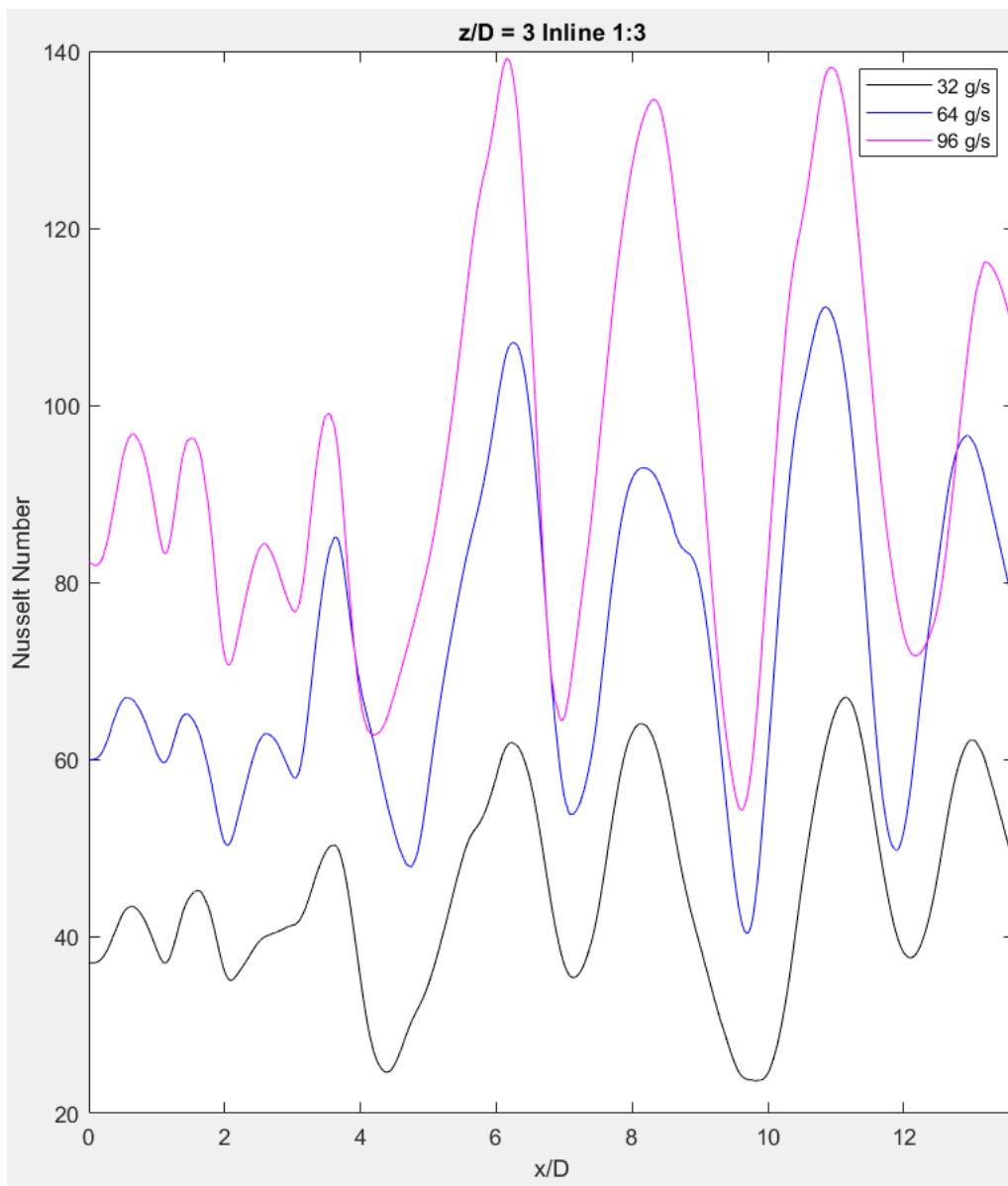


Figure 3.38: Spanwise Nusselt Number distribution for 1:3 mass flow inline configuration

($z/D = 3$)

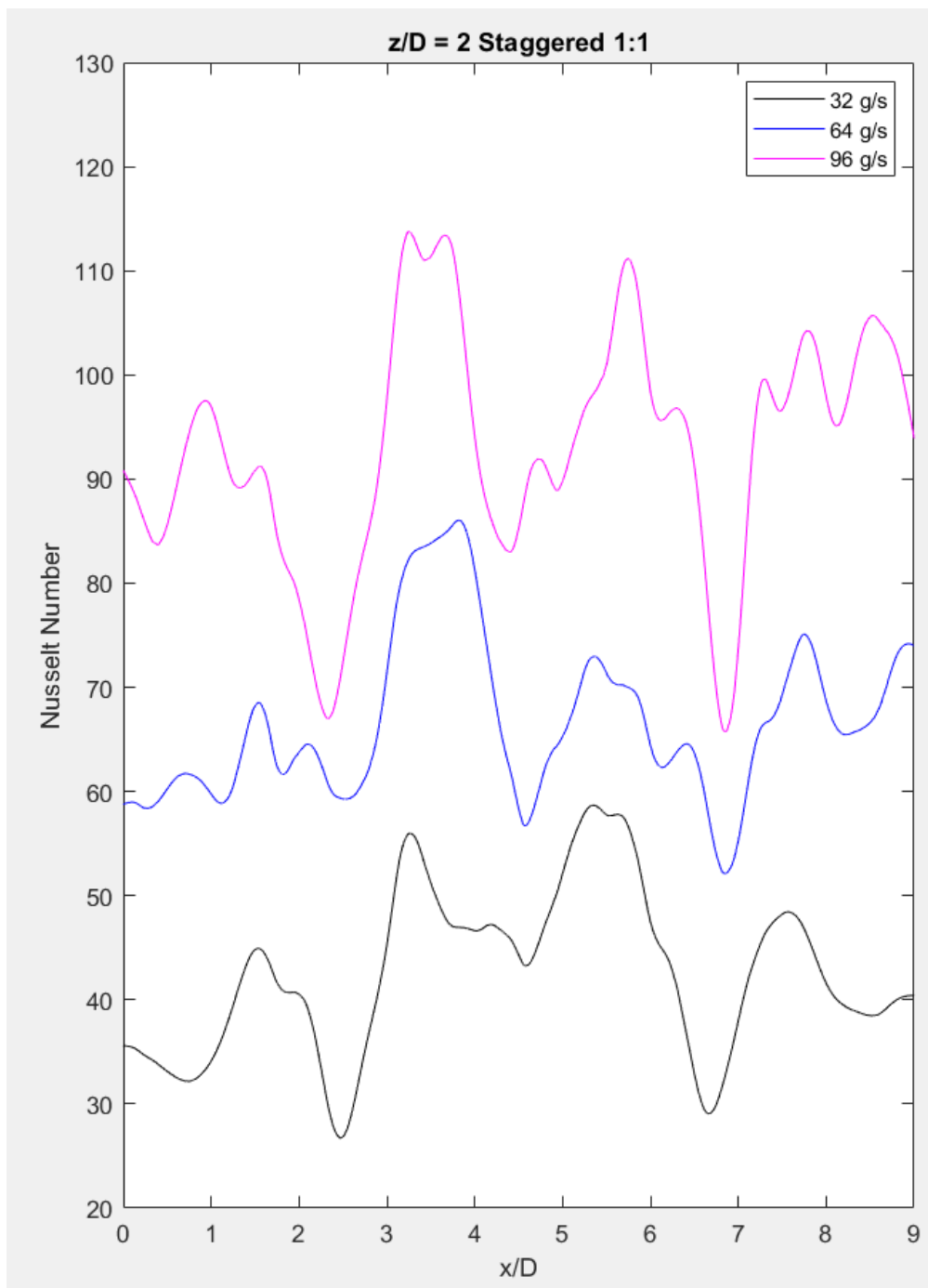


Figure 3.39: Spanwise Nusselt Number distribution for 1:1 mass flow staggered configuration

($z/D = 2$)

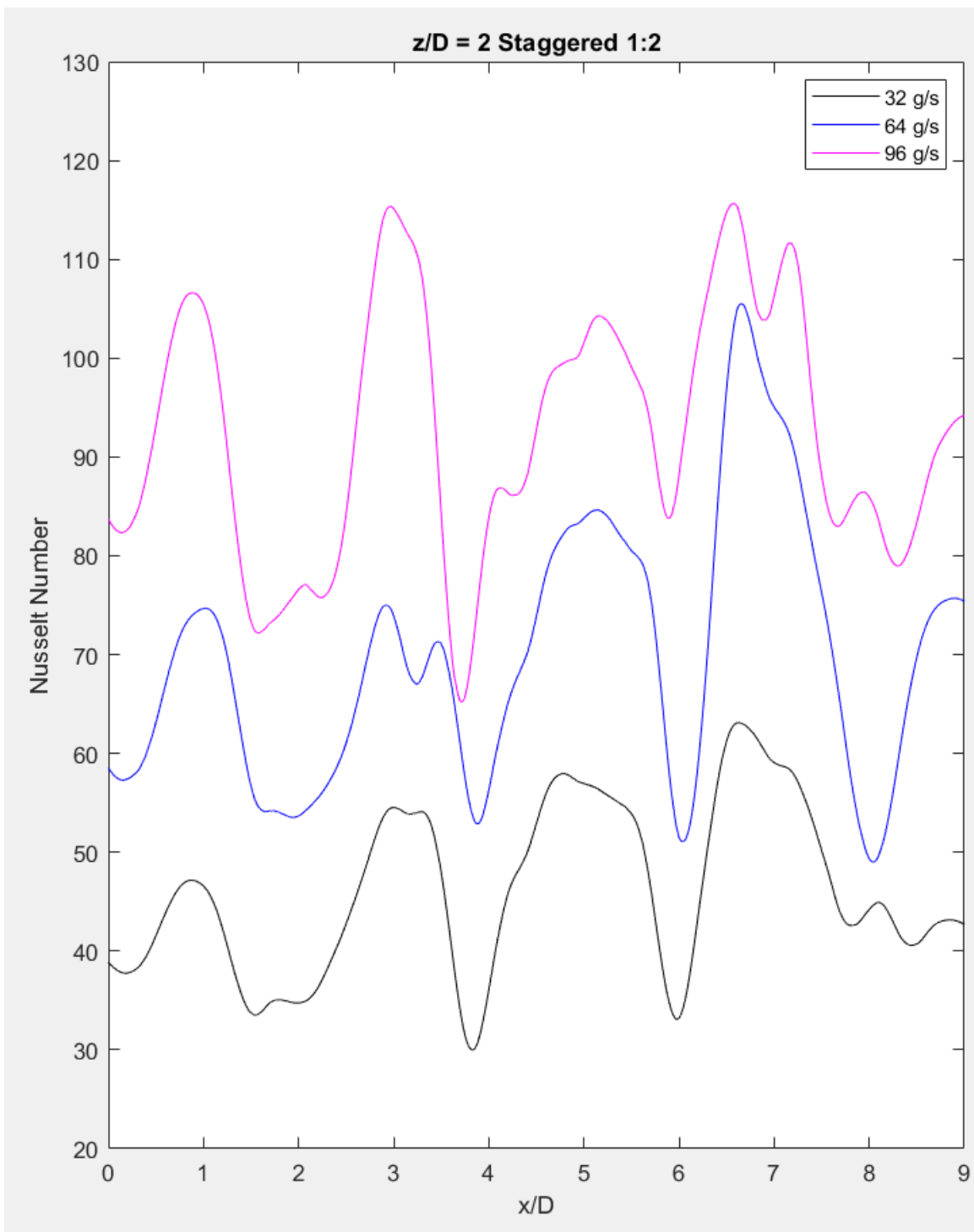


Figure 3.40: Spanwise Nusselt Number distribution for 1:2 mass flow staggered configuration

($z/D = 2$)

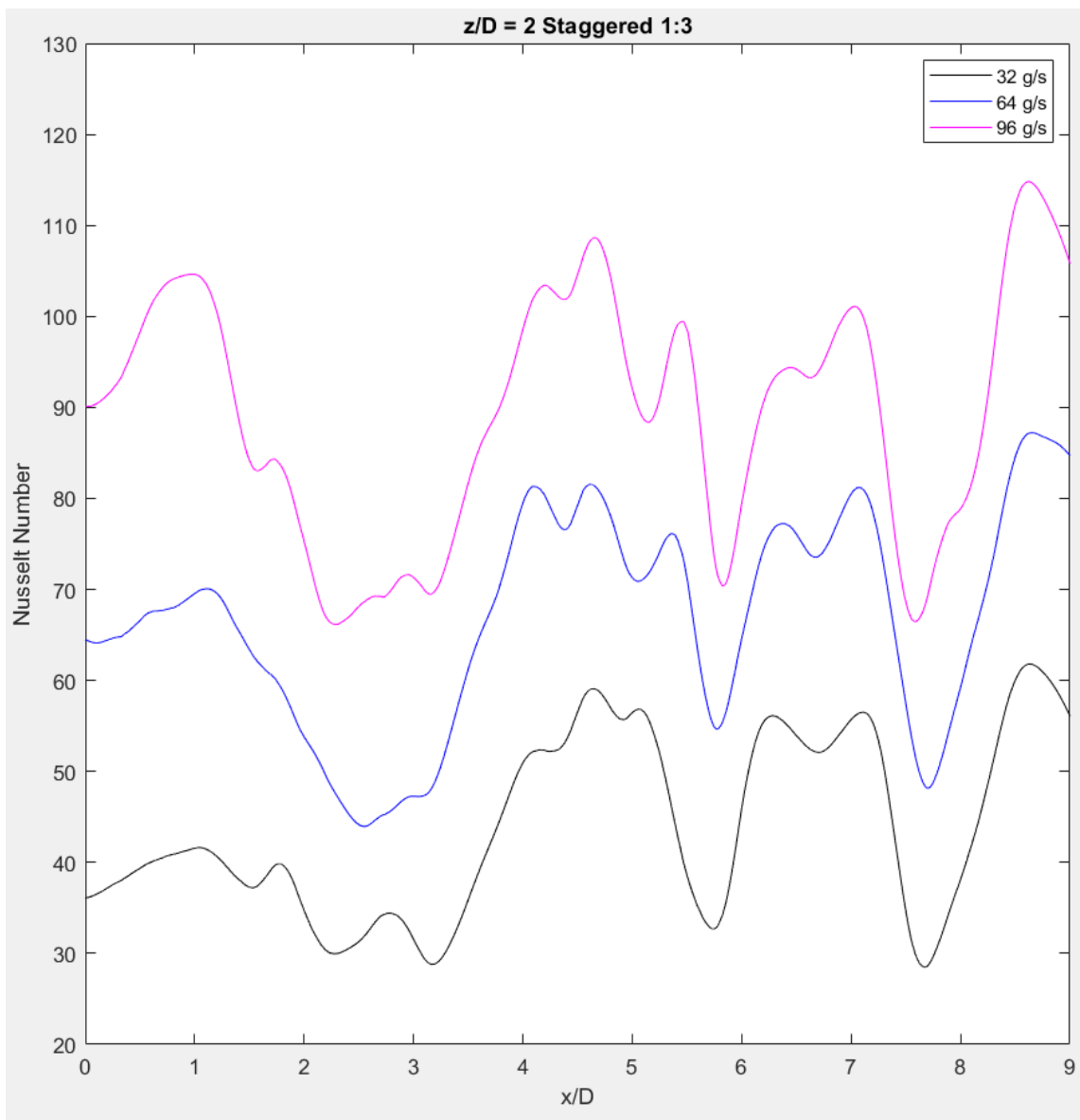


Figure 3.41: Spanwise Nusselt Number distribution for 1:3 mass flow staggered configuration
($z/D = 2$)

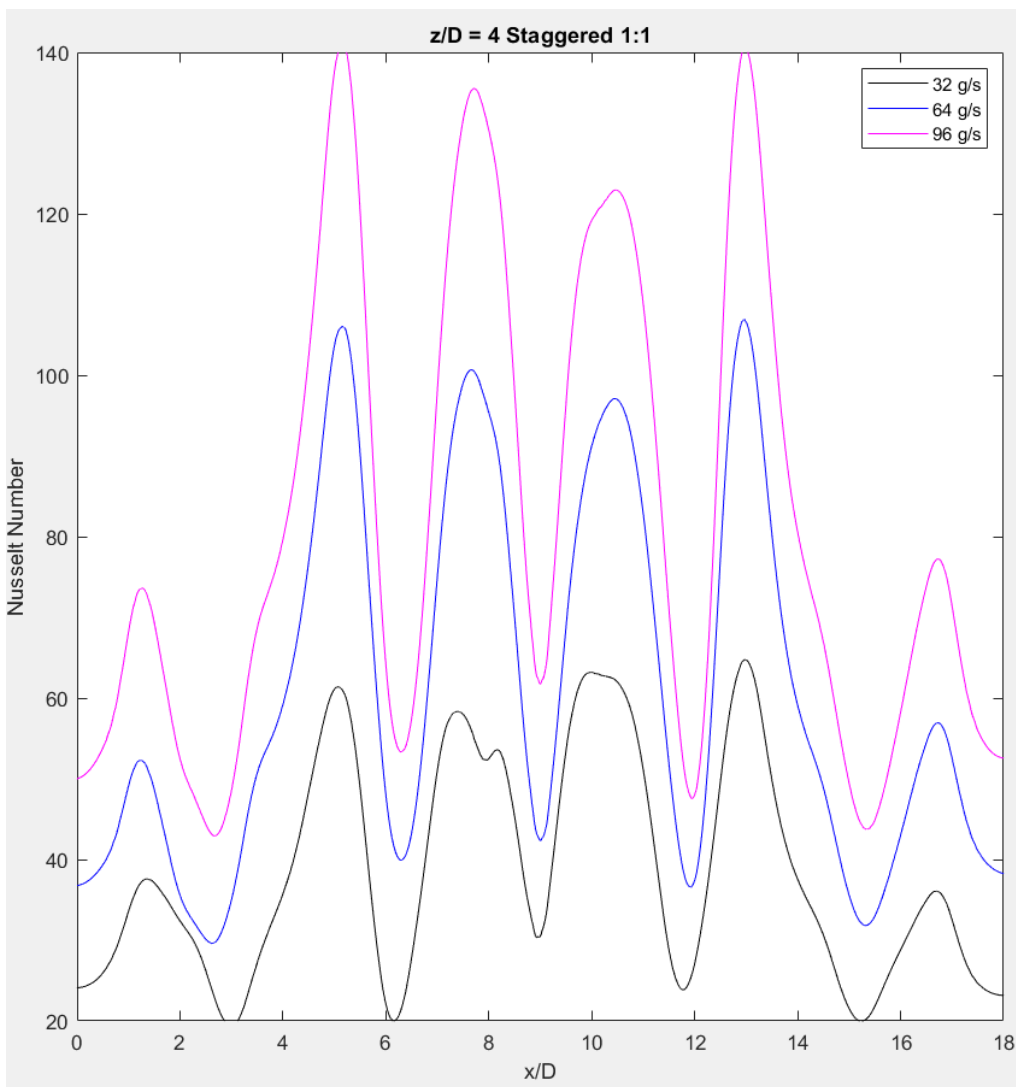


Figure 3.42: Spanwise Nusselt Number distribution for 1:1 mass flow staggered configuration
($z/D = 4$)

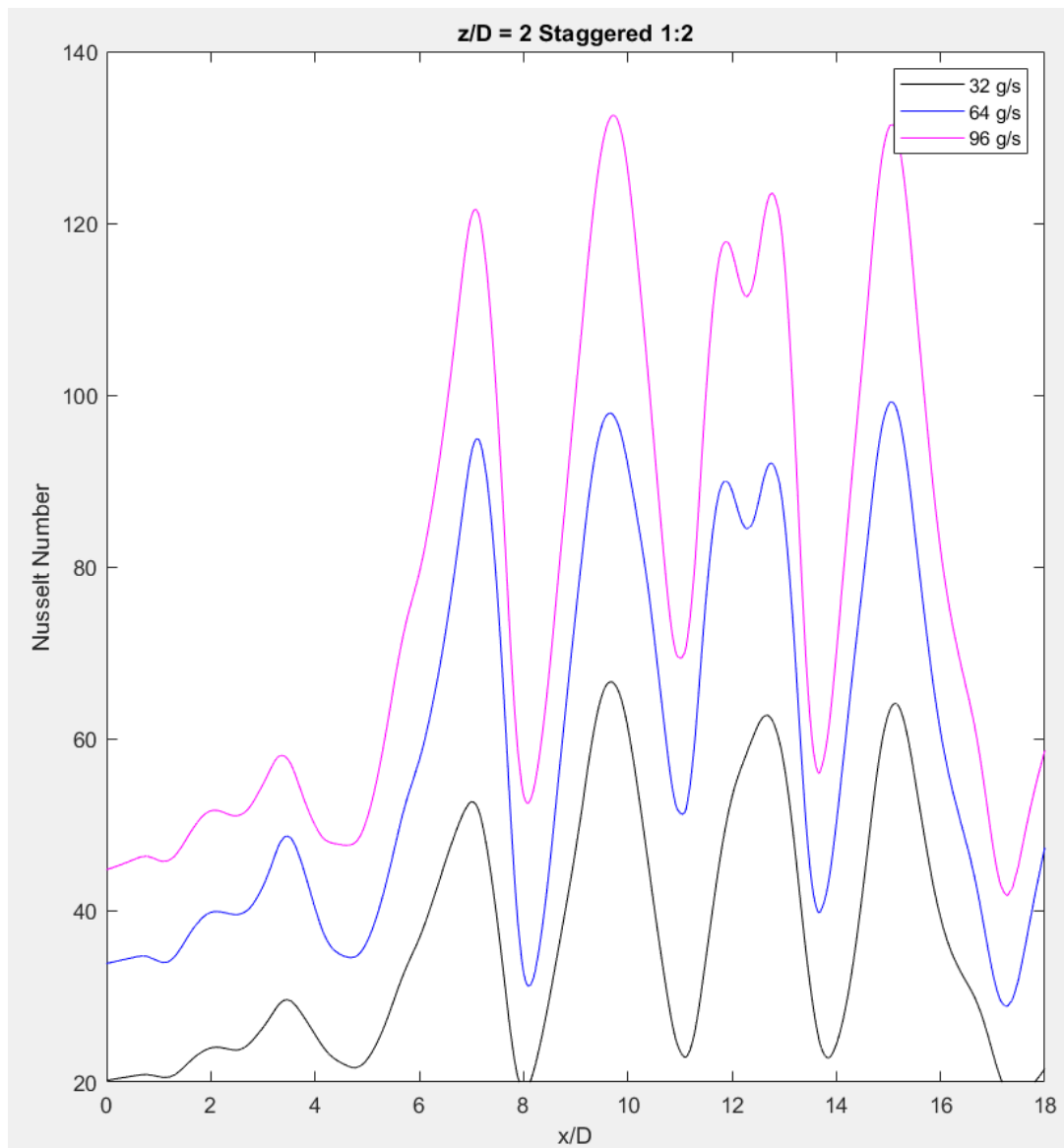


Figure 3.43: Spanwise Nusselt Number distribution for 1:2 mass flow staggered configuration
($z/D = 4$)

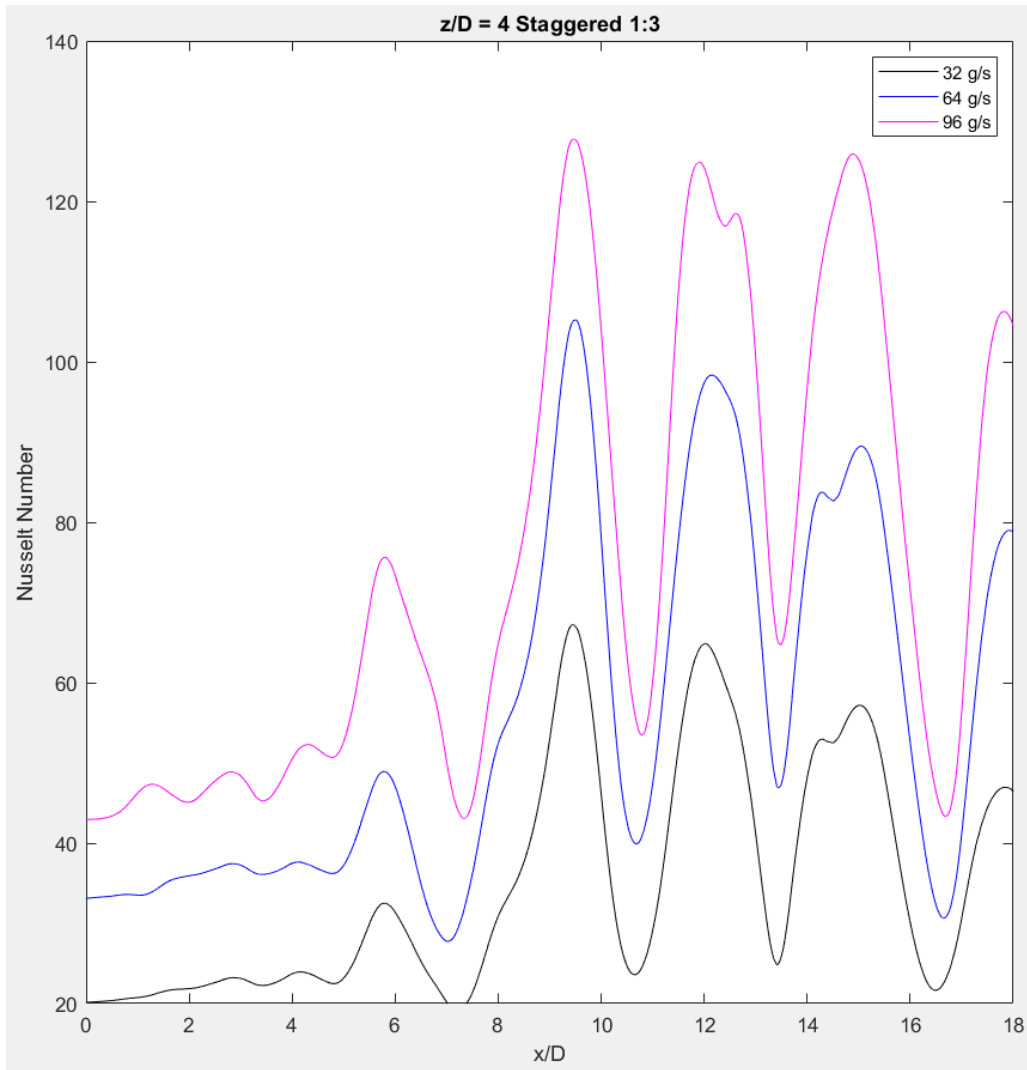


Figure 3.44: Spanwise Nusselt Number distribution for 1:3 mass flow staggered configuration

($z/D = 4$)

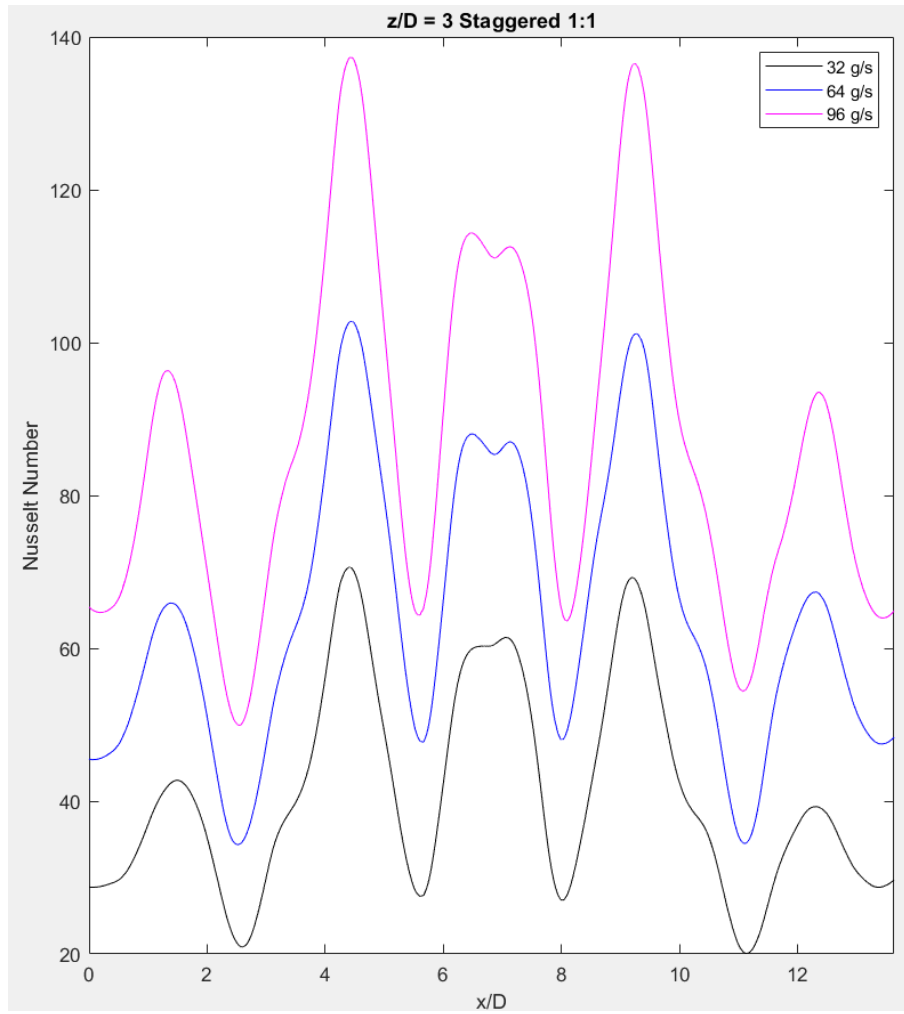


Figure 3.45: Spanwise Nusselt Number distribution for 1:1 mass flow staggered configuration

($z/D = 3$)

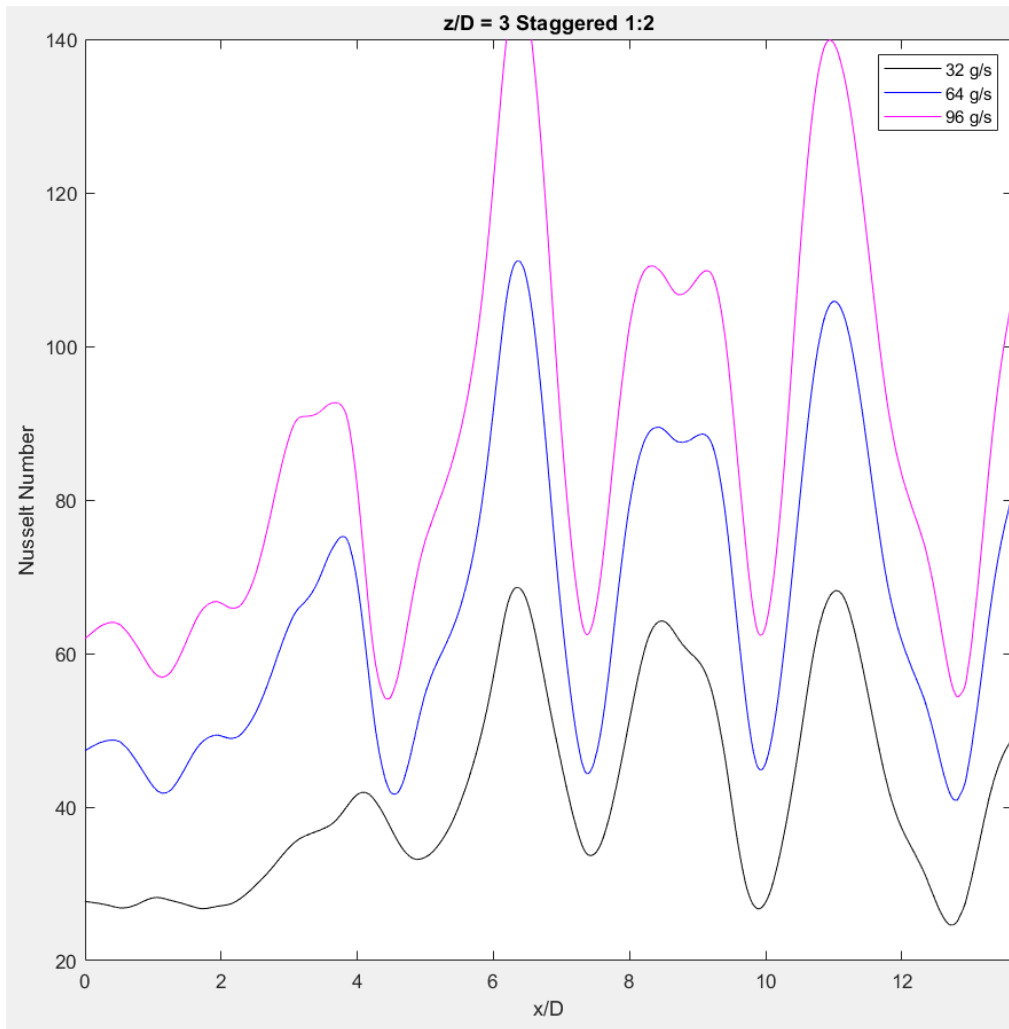


Figure 3.46: Spanwise Nusselt Number distribution for 1:2 mass flow staggered configuration

($z/D = 3$)

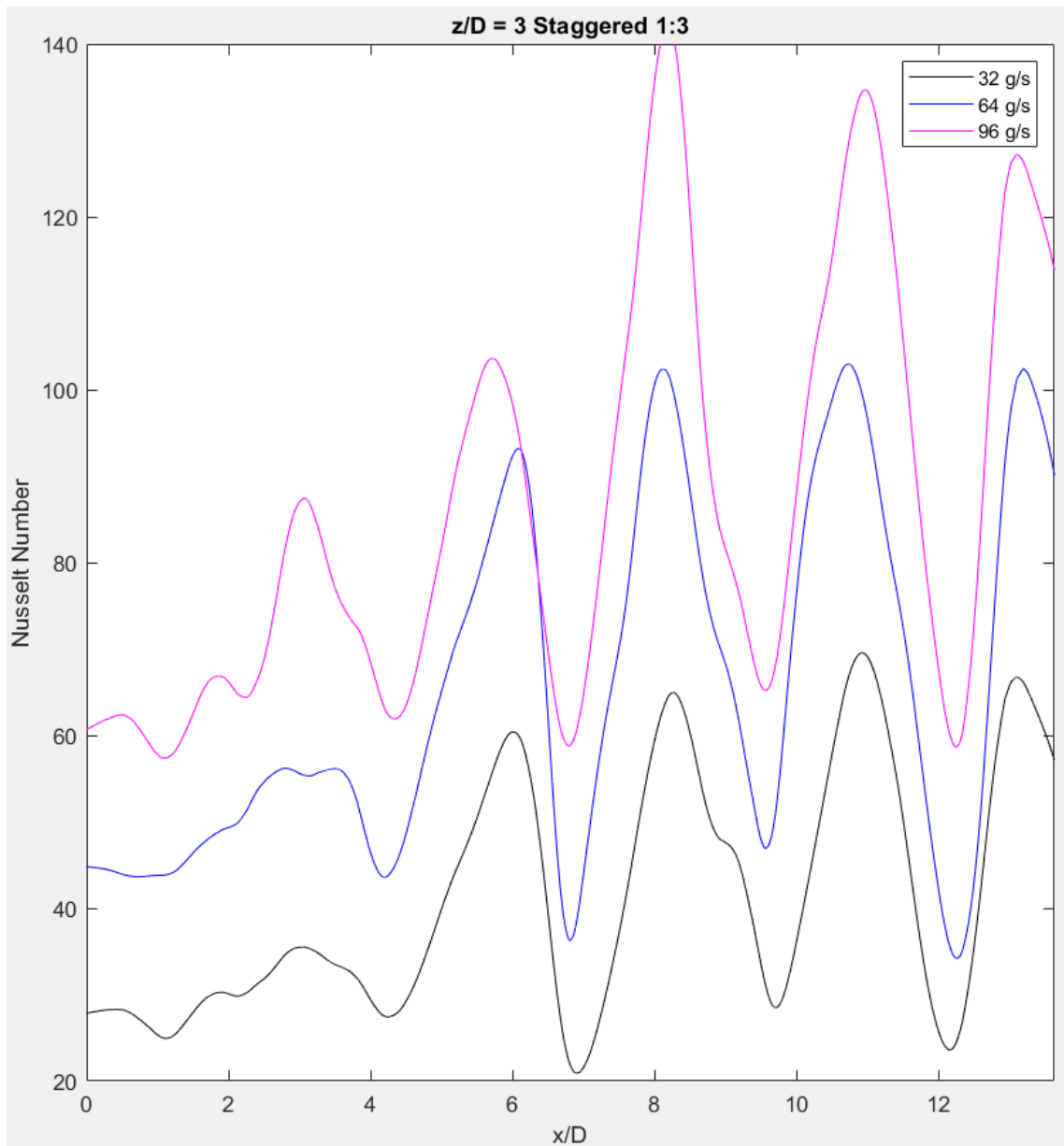


Figure 3.47: Spanwise Nusselt Number distribution for 1:3 mass flow staggered configuration
($z/D = 3$)

The staggered configuration shows a much higher sensitivity to the mass flow bias. Figures 3.39 to 3.47 show the staggered configurations for all the z/D ratios for different mass flow rate exit ratios. It can be observed that the staggered configuration shows a aggressive reduction in

maxima and minima when moving towards the mass flow exit with higher mass flow rate. Also, as the z/D ratio increases, this behavior is more pronounced.

3.4 Overall Nusselt Number for the Region of Interest

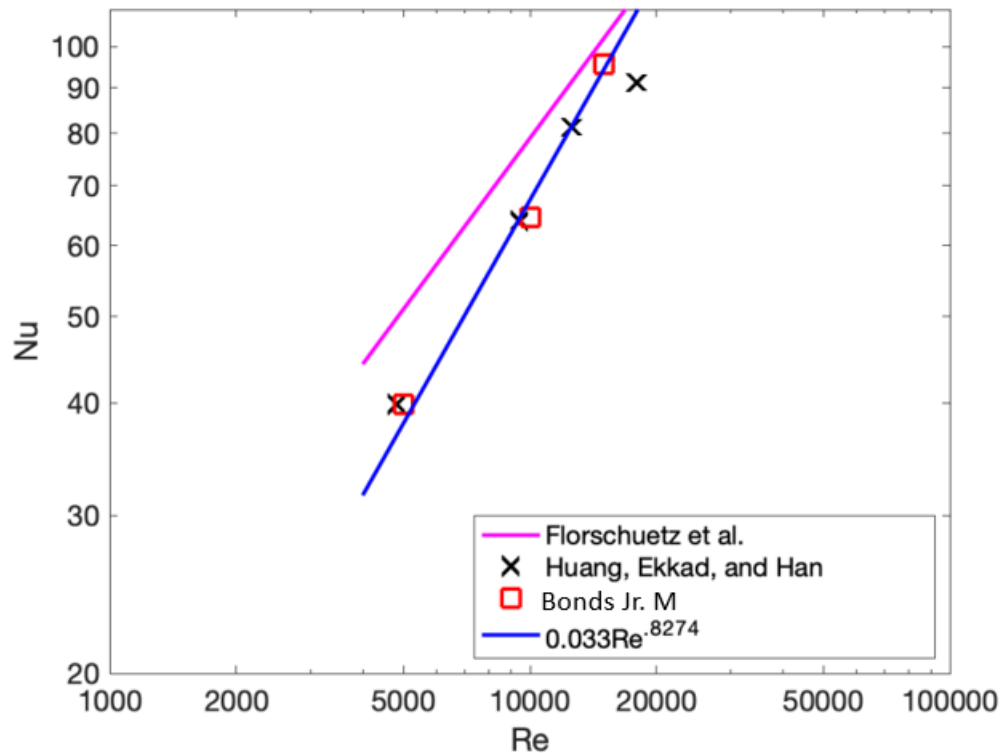


Figure 3.48: Overall Nusselt Number comparison with existing Literature

The average Nusselt number is calculated for the region of interest of the test section where the spanwise Nusselt number is calculated. Comparing the values of overall Nusselt number with literature [14], the values of Nusselt number are within 15 % of the experimental values obtained. The difference might be due to the simulations being done at ideal conditions with uniform flow inlet and adiabatic walls. Due to this, the Nusselt number gets overpredicted for the low mass flow rate cases. The experiment also has a mean uncertainty of 10 % and a local uncertainty of 22.43 %. Further validating the overall Nusselt number values with different studies as shown in the below figure, the overall Nusselt number as shown in the Figures 3.48 for $z/D = 3$ is within 10 %

of the values from literature with the Nusselt number being 45 for Re 5000, 71 for Re 10000 and 92 for Re 15000.

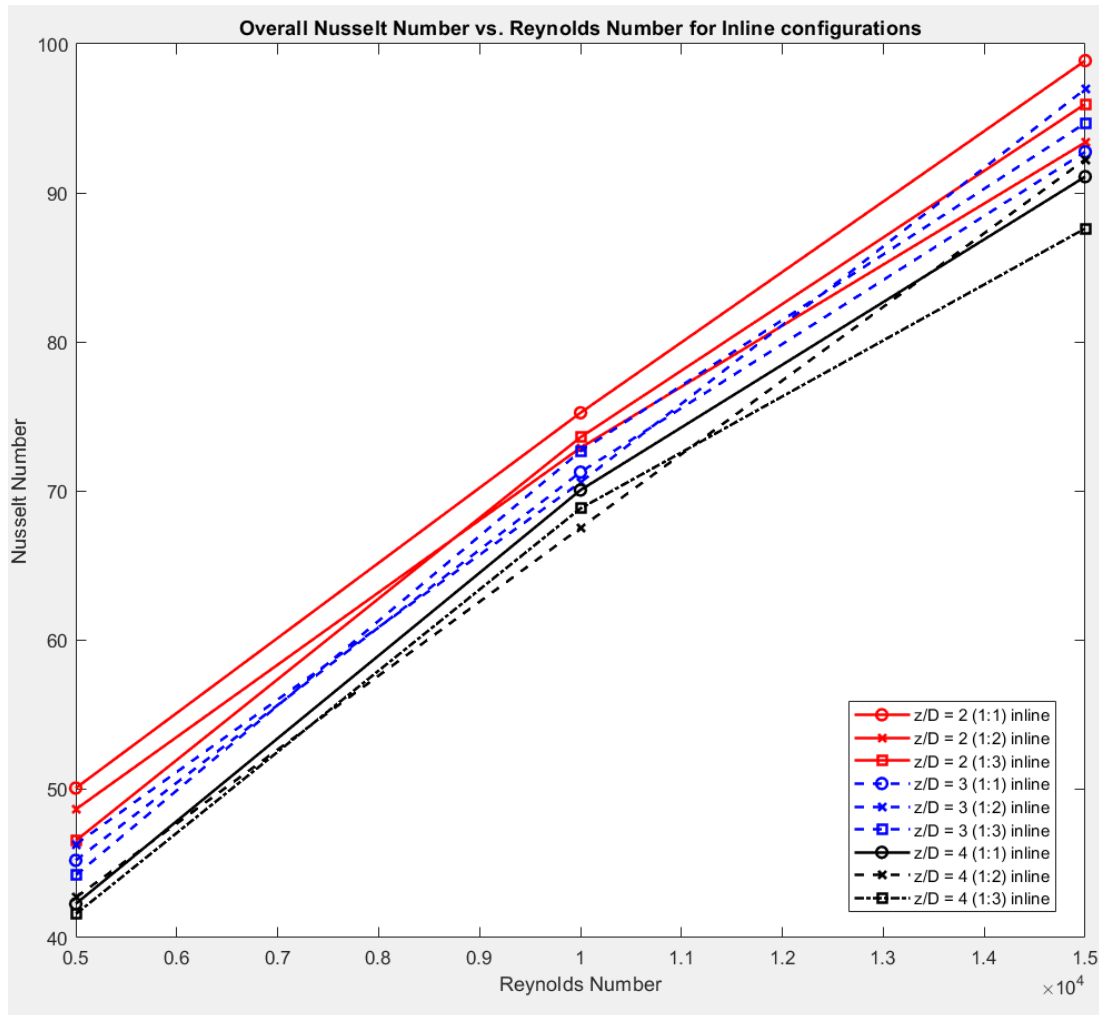


Figure 3.49: Overall Nusselt number vs. Reynolds number for inline configurations

Comparing the overall Nusselt numbers between the inline and staggered configurations, it can be observed that the inline configurations provide a higher overall Nusselt number compared to the staggered configurations. The Nusselt number values are higher as z/D ratio decreases and 1:1 configuration provides a higher heat transfer compared to the 1:2 and 1:3 configurations for almost all mass flow rates. For some cases, 1:2 and 1:1 configurations provide similar overall Nusselt number values.

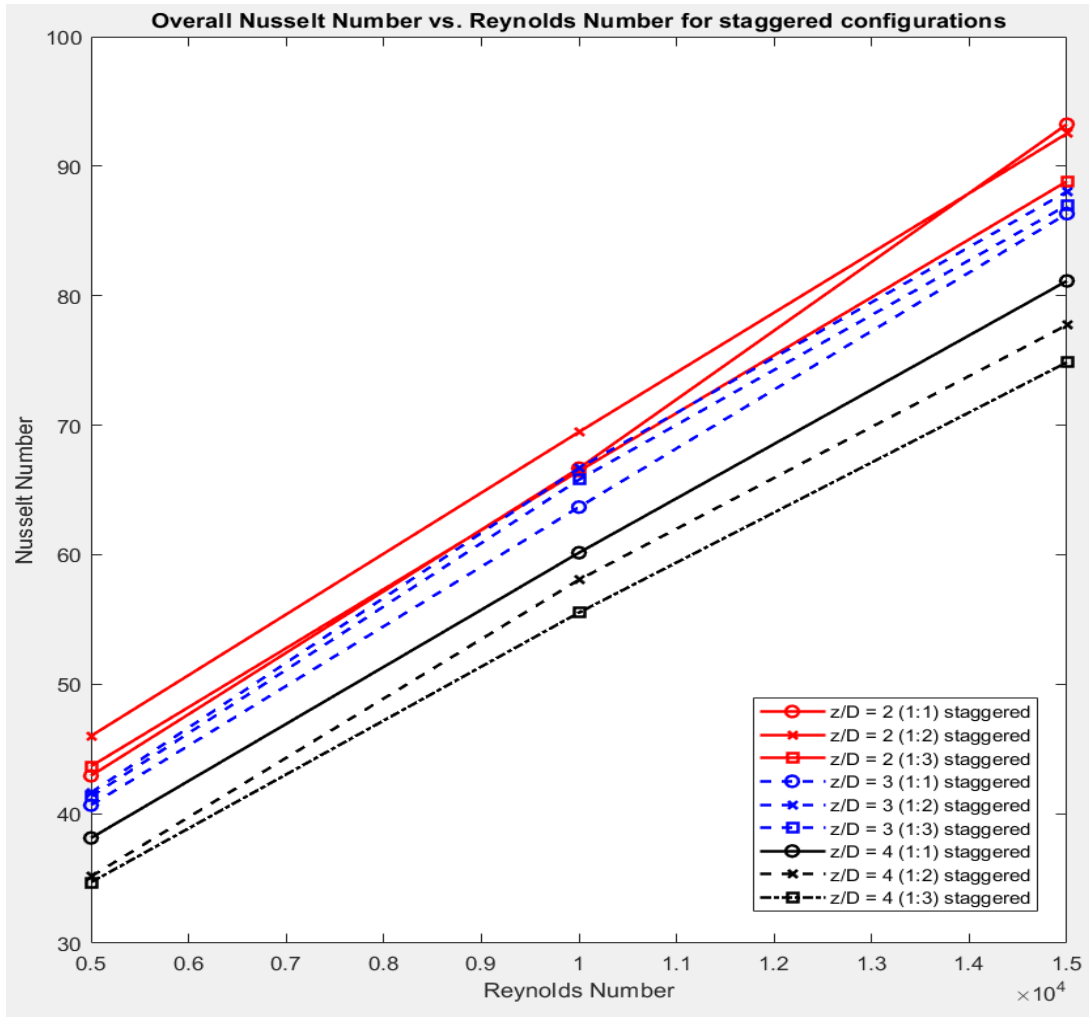


Figure 3.50: Overall Nusselt number vs. Reynolds number for staggered configurations

3.5 Nusselt Number Contours

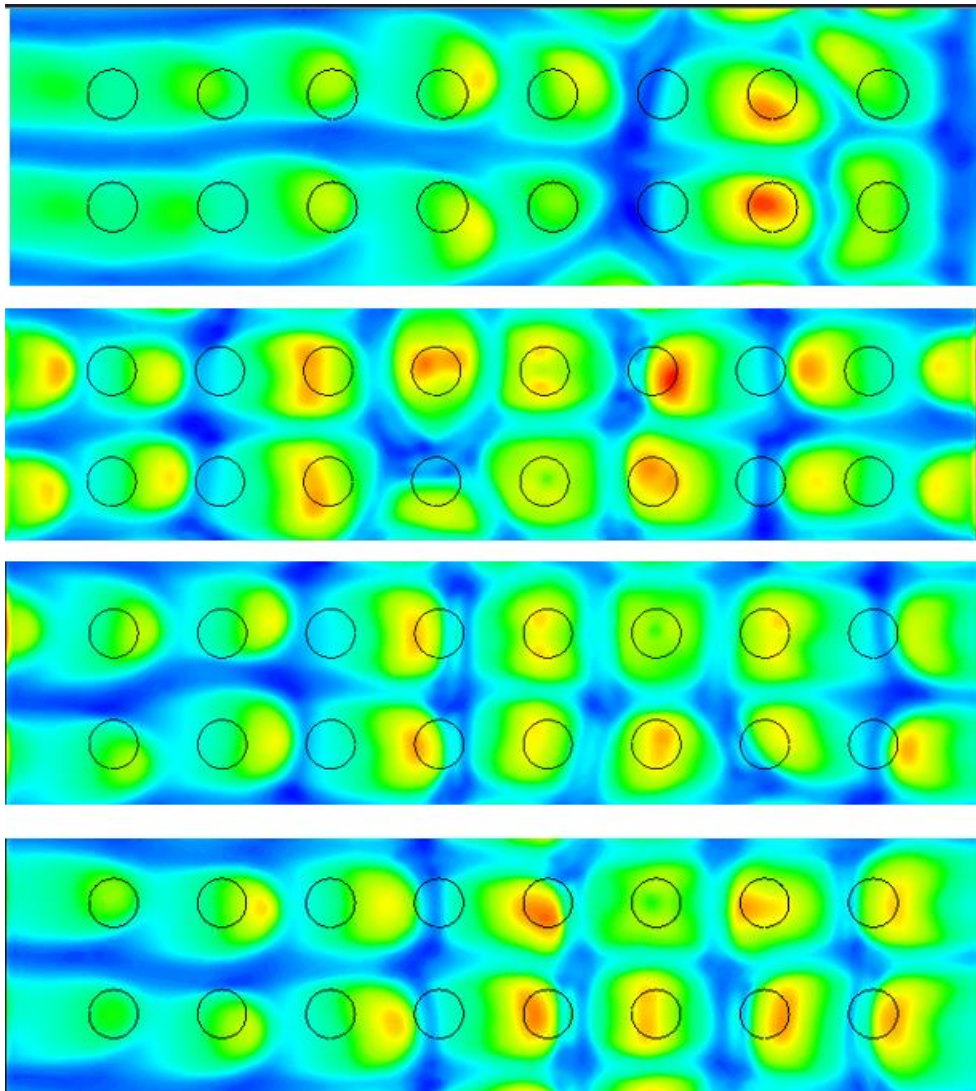


Figure 3.51: Nusselt number contours for inline configuration for $z/D = 4$ with $Re = 10000$ for different mass flow rate exits (higher mass flow exit at the left side), (a) 1:0, (b) 1:1, (c) 1:2, (d)

1:3

The Nusselt number contours provide further insight on how the heat transfer gets distributed when the mass flow is biased through one exit. Figure 3.51 shows 2 rows of jets and how the Nusselt number varies with different mass flow exits.

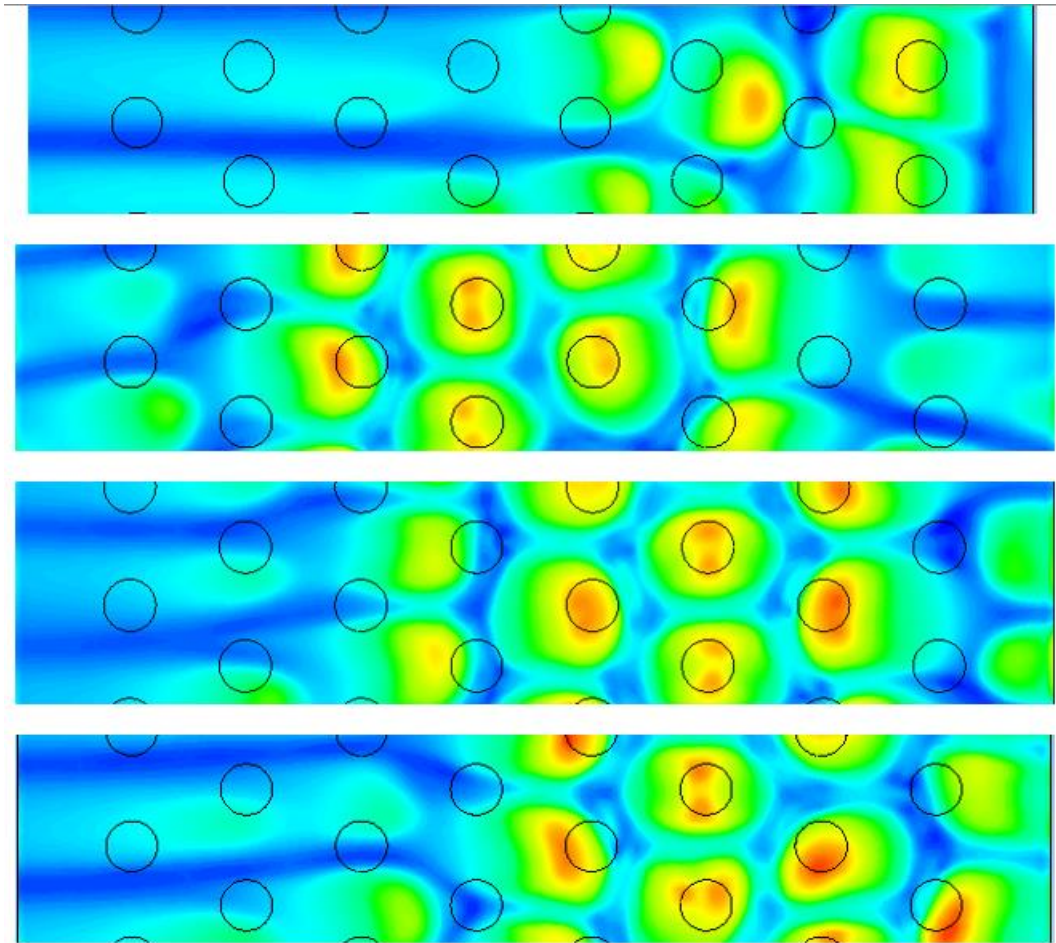


Figure 3.52: Nusselt number contours for staggered configuration for $z/D = 4$ with $Re = 10000$ for different mass flow rate exits (higher mass flow exit at the left side), (a) 1:0, (b) 1:1, (c) 1:2, (d)

1:3

The Nusselt number contours for the staggered grid provide an explanation on why the inline grids have higher heat transfer performance compared to the staggered grid setting based on figure 3.52.

CHAPTER 4

CONCLUSION

The numerical study on the effect of different types of exit schemes with variable mass flow exits has been simulated for a total of 72 different configurations with inline and staggered grids. The z/D ratios used for the simulations are 2,3 and 4 by varying the jet diameters. The different mass flow ratios analyzed are 1:0, 1:1, 1:2, and 1:3 for Reynolds numbers 5000, 10000, and 15000. The simulations have also been validated using experimental results and past studies on array jet impingement. The following inferences can be taken from the study.

1. The bidirectional exit schemes with mass flow ratios 1:1, 1:2, and 1:3 provided better heat performance compared to the single exit schemes.
2. 1:1 mass flow scheme provides uniform heat transfer across the test section and provides the highest overall and local Nusselt numbers compared to the other bidirectional exit schemes and the single exit scheme.
3. The difference in the overall Nusselt number for the same Reynolds number is not very different for the 1:2 and 1:3 schemes compared to the 1:1 scheme. However, local Nusselt numbers are higher towards the lower mass flow exit side compared to the higher mass flow exit. This can be beneficial for cooling specific regions of test sections where the heat generation is high.
4. The area averaged and overall Nusselt number values are higher for lower z/D values independent of the exit scheme being used.
5. The inline grids show higher overall and local Nusselt number values compared to the staggered grids. Therefore, inline grids should be the preferred setting for maximizing heat transfer.

CHAPTER 5

FUTURE WORK

The primary study provided in the current thesis is to quantify and check the behavior of array jet impingement for differing mass flow exits for bidirectional exit configurations. The study explains the thermal performance of the jets based on the z/D ratios and Reynolds number. From the analysis done in the current study, the future work recommendations are mentioned below.

1. The crossflow configuration with different mass flow exit ratios has only been analyzed with respect to the Reynolds number and very low z/D ratios in this study. Higher z/D ratios may provide different results compared to the contours obtained in the current study. Further, changing the hole spacing provides another interesting option to study the thermal performance of the jets.
2. Along with numerical simulations of the above, experimental methods can be set up to analyze the new methods such that transient methods using Liquid Crystal Thermography or Infrared cameras are more accurate. The 1-D lumped capacitance and semi-infinite models provide accurate results. However, methods can be set up such that the heat flux on the inside surface of the plate can be measured directly so that accuracy of the experiments provide a better validation for the numerical analysis.
3. Future work can also include having exits in more directions with different exit mass flow rates to see if the stagnation point can be moved to different locations on the jet such that heat transfer can be concentrated on few hotspots.
4. Another interesting study that could be done is the effect of angled jets on test section. This might yield results which can show more heat transfer if the jets are angled away from the

exit with higher mass flow exit and lower heat transfer when the jets are angled towards the higher mass flow rate exit.

NOMENCLATURE

Re	Reynolds Number
Nu	Nusselt Number
z	Distance from orifice plate to test section
D	Jet/Orifice diameter
x	Spanwise distance across the test section
h	Heat transfer coefficient
L	Characteristic length
k_{air}	Thermal conductivity
T	Temperature at the test section
T_{ref}	Reference Temperature
q''	Heat Flux
ρ	Density
k	Turbulent kinetic energy
ω	Specific rate of dissipation
\widetilde{G}_k	Generation of turbulent kinetic energy due to mean velocity gradients
G_ω	Generation of ω
Y_ω	Dissipation of ω due to turbulence
S_k	User specified source term
D_ω	Cross-diffusion term
S_ω	User specified source term
Y_ω	Dissipation of ω due to turbulence
τ_ω	Effective diffusivity of ω

τ_k Effective diffusivity of k

REFERENCES

- [1] K. Jambunathan, E. Lai, M. A. Moss, and B. L. Button, “A review of heat transfer data for single circular jet impingement,” *Int J Heat Fluid Flow*, vol. 13, no. 2, pp. 106–115, Jun. 1992, doi: 10.1016/0142-727X(92)90017-4.
- [2] P. S. Penumadu and A. G. Rao, “Numerical investigations of heat transfer and pressure drop characteristics in multiple jet impingement system,” *Appl Therm Eng*, vol. 110, pp. 1511–1524, 2017, doi: <https://doi.org/10.1016/j.applthermaleng.2016.09.057>.
- [3] A. Ü. Tepe, “Numerical investigation of a novel jet hole design for staggered array jet impingement cooling on a semicircular concave surface,” *International Journal of Thermal Sciences*, vol. 162, p. 106792, 2021, doi: <https://doi.org/10.1016/j.ijthermalsci.2020.106792>.
- [4] Y. Q. Zu, Y. Y. Yan, and J. D. Maltson, “CFD PREDICTION FOR MULTI-JET IMPINGEMENT HEAT TRANSFER,” in *Proceedings of ASME Turbo Expo 2009: Power for Land, Sea and Air*, 2009. [Online]. Available: http://asmedigitalcollection.asme.org/GT/proceedings-pdf/GT2009/48845/483/2765665/483_1.pdf
- [5] L. W. Florschuetz *et al.*, “NASA Contractor Report 3217 4 NASA CR 3217 Multiple Jet Impingement Characteristic-Experimental Investigation of In-Line and Staggered Arrays With Crossflow.”
- [6] L. Florschuetz, C. R. Truman, and D. E. Metzger, “Streamwise Flow and Heat Transfer Distributions for Jet Array Impingement with Crossflow,” 1981. [Online]. Available: <http://asmedigitalcollection.asme.org/GT/proceedings-pdf/GT1981/79634/V003T09A005/2393497/v003t09a005-81-gt-77.pdf>

- [7] Y. Huang, S. v. Ekkad, and J. C. Han, "Detailed heat transfer distributions under an array of orthogonal impinging jets," *J Thermophys Heat Trans*, vol. 12, no. 1, pp. 73–79, 1998, doi: 10.2514/2.6304.
- [8] A. Terzis, G. Wagner, and P. Ott, "HOLE STAGGERING EFFECT ON THE COOLING PERFORMANCE OF NARROW IMPINGEMENT CHANNELS," 2012. [Online]. Available: http://asmedigitalcollection.asme.org/GT/proceedings-pdf/GT2012/44700/127/4228087/127_1.pdf?casa_token=Kr91IR5p3y4AAAAA:8QTcTXmj1g7Fbp4s-1G6Oql3_wcAvOlxPy8ML17X-XEQYCbko3MrNX0IHai5JId6f4JDT4i
- [9] A. Terzis, J. von Wolfersdorf, B. Weigand, and P. Ott, "DETAILED HEAT TRANSFER DISTRIBUTIONS OF NARROW IMPINGEMENT CHANNELS WITH VARYING JET DIAMETER," 2014. [Online]. Available: http://asmedigitalcollection.asme.org/GT/proceedings-pdf/GT2014/45714/V05AT12A028/4231722/v05at12a028-gt2014-25910.pdf?casa_token=iqzGtW8bojEAAAAA:MaQ21jXjNvEmYtxIlnsYmb598KUOr203DRoHI6P2riOzY8LnoD9WYeTjUA7jigx9sqLnhfrW
- [10] S. Fechter, A. Terzis, P. Ott, B. Weigand, J. von Wolfersdorf, and M. Cochet, "Experimental and numerical investigation of narrow impingement cooling channels," *Int J Heat Mass Transf*, vol. 67, pp. 1208–1219, 2013, doi: 10.1016/j.ijheatmasstransfer.2013.09.003.
- [11] W. Tabakoff, "Heat Transfer by a Spare Array of Round Air Jets Impinging Perpendicular to a Flat Surface Including the Elect of Spent Air," 1970. [Online]. Available: http://asmedigitalcollection.asme.org/gasturbinespower/article-pdf/92/1/73/5885907/73_1.pdf?casa_token=8KXiPHCAIUQAAAAA:gJ9lk-

2R4wDkCr36HtOdOvgP2WAI-uAjQmk6GmvMjz4Q8RMiaLnbopf5Y7OTpY-
GXbuM4tpg

- [12] S. Madhavan, K. R. Ramakrishnan, P. Singh, and S. Ekkad, “Jet Impingement Heat Transfer Enhancement by U-Shaped Crossflow Diverters,” *J Therm Sci Eng Appl*, vol. 12, no. 4, Aug. 2020, doi: 10.1115/1.4045514.
- [13] M. B. Ibrahim, B. J. Kochuparambil, S. v Ekkad, and T. W. Simon, “CFD FOR JET IMPINGEMENT HEAT TRANSFER WITH SINGLE JETS AND ARRAYS,” 2005. [Online]. Available: http://asmedigitalcollection.asme.org/GT/proceedings-pdf/GT2005/47268/359/2638277/359_1.pdf
- [14] M. A. Bonds Jr., “Evaluation of Complex Cooling Geometries with Jet Impingement and Effusion for Gas Turbine Combustor Liners (PhD Thesis),” 2022. Accessed: Nov. 27, 2022. [Online]. Available: <https://repository.lib.ncsu.edu/handle/1840.20/40078>
- [15] “ANSYS, Inc. ANSYS Fluent User’s Guide, Release 12.0.,” 2009.

APPENDICES

Appendix A

Example for the multizone mesh used for 0.25 inch plate ($z/D = 4$).

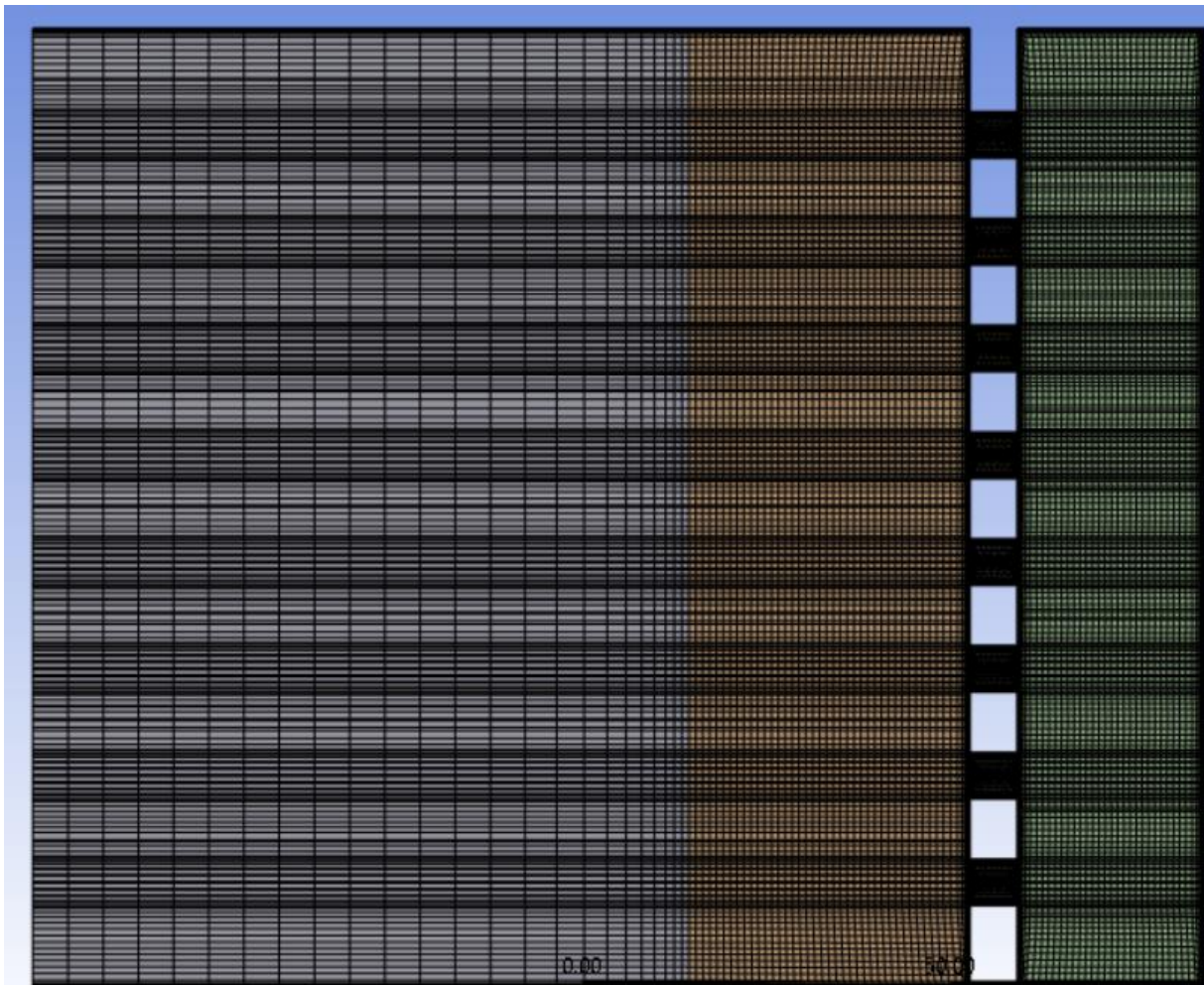


Figure A1: Sectional view of Inlet, holes and impingement region

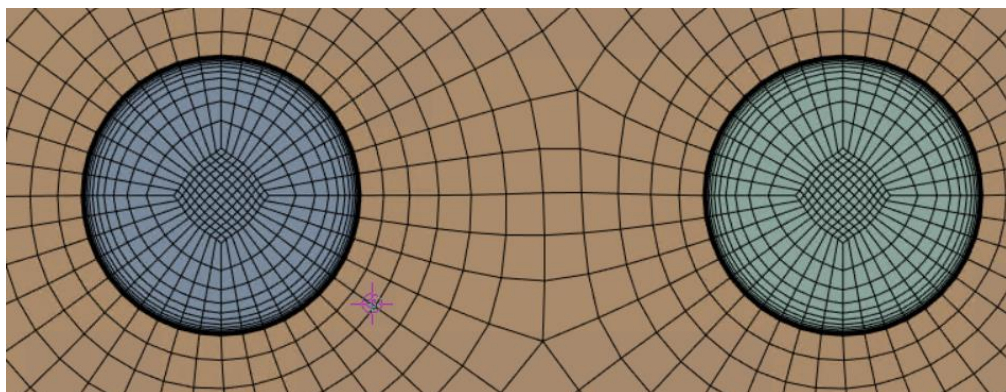


Figure A2: Sectional view of inflation layer for holes.

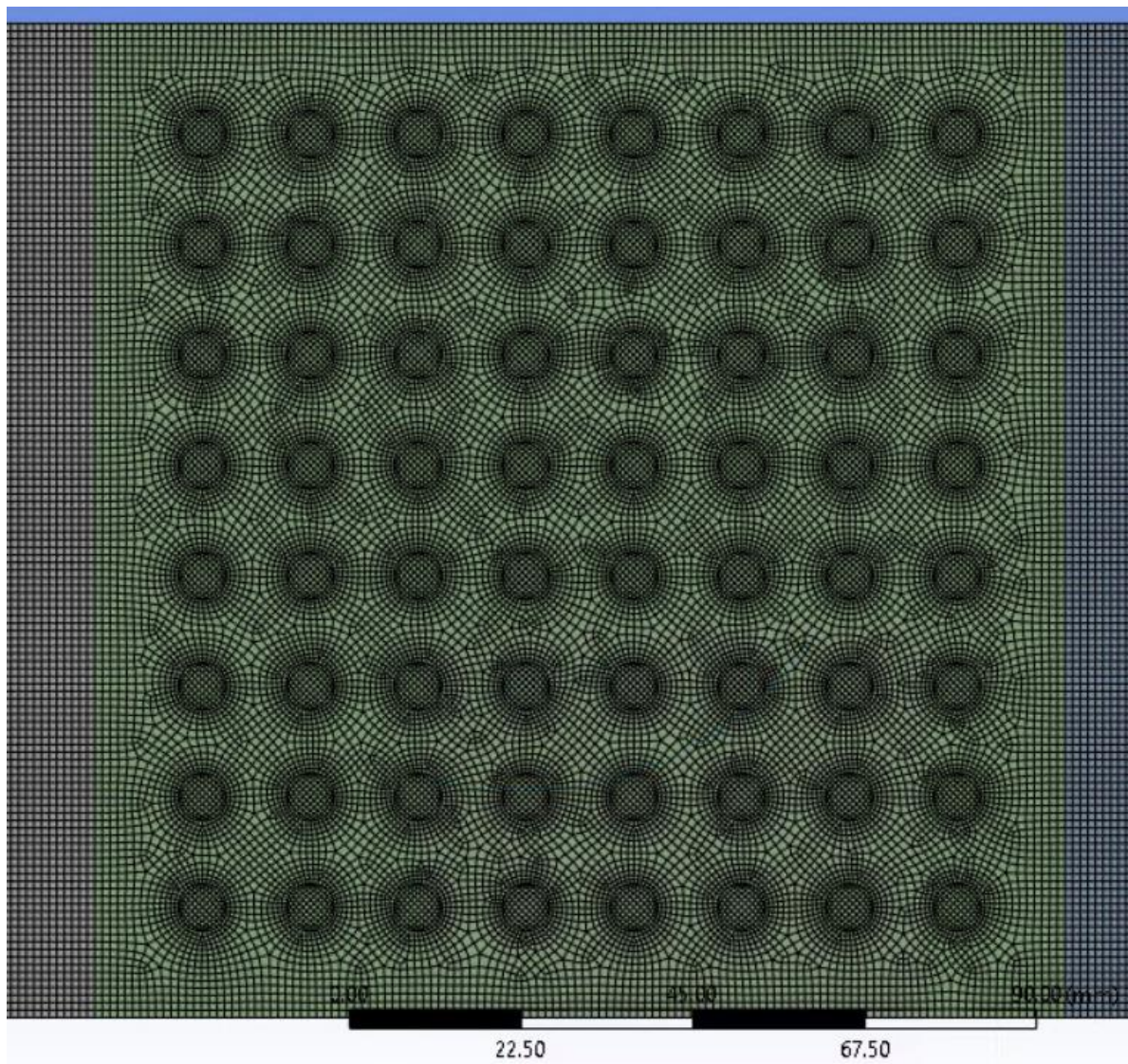


Figure A3: Multizone mesh on test section